Contract No. DTFACT-15-D-00007
Delivery Order 015: Reflective Cracking Support
Deliverable: 4.10.2.2 Reflective Cracking Indoor Phase 6 Material Characterization Report

June 1, 2020

Prepared by **General Dynamics Information Technology**

GENERAL DYNAMICS
Information Technology

TABLE OF CONTENTS

	Page
1. INTRODUCTION	1
2. OBJECTIVES	1
3. LABORATORY TESTING PROGRAM	1
4. HMA MIX DESIGN	2
5. TEST RESULTS AND DATA ANALYSIS	3
5.1 Dynamic Modulus Test	3
5.2 Texas Overlay Test	9
5.3 Customized Overlay Test	11
5.3.1 Cycle to Failure and Crack Resistance Index	13
5.3.2 Strain Analysis	17
5.3.3 Paris Law	20
6. EFFECT OF EXTREME COOLING CYCLE	22
6.1 Effect on Fracture Energy	22
6.2 Effect on Strain Energy	23
7. FULL-SCALE VS CUSTOMIZED OT TESTS	26
8. CONCLUSIONS	30
9. REFERENCES	32
APPENDICES	

LIST OF FIGURES

Figure	Page
1 Dynamic Modulus Master Curves	4
2 Dynamic Modulus Comparison Among Reflective Cracking Indoor Phases	8
3 Area Used for Calculation of Critical Fracture Energy [34]	9
4 Calculation of Crack Resistance Index [34]	10
5 Customized OT Specimen Instrumentation	12
6 Failure Strain	18
7 Failure Cycle	19
8 Failure Strain Comparison	20
9 d*a*/d*N* vs. SIF	22
10 Typical Plot of Fracture Energy vs Cycle Number	23
11 Fracture Energy Increase/Decrease Percentage for Each Extreme Cooling Cycle	23
12 Typical Plot of Strain Energy vs Cycle Number	25
13 Strain Energy Increase/Decrease Percentage for Each Extreme Cooling Cycle	25
14 Failure Strain Comparison between Full-Scale Test and Customized OT	26
15 Failure Cycle Comparison between Full-Scale Test and Customized OT	27
16 Fracture Energy Increase/Decrease After 1st Extreme Cooling Cycle	28
17 Strain Energy Increase/Decrease After 1st Extreme Cooling Cycle	29

LIST OF TABLES

Table Page
1 Laboratory Testing Program 2
2 Aggregate Gradation and Volumetric of Studied HMA Mixture 2
3 Modulus and Phase Angle Values of Dynamic Modulus Test 5
4 HMA Mix Details in Different Reflective Cracking Indoor Phases 7
5 Texas Overlay Test Results Summary 10
6 Statistical Analysis Result for Texas Overlay Test 11
7 Laboratory Test Plan to Study Occurrence of an Extreme Cooling Cycle using the Customized OT 13
8 Summary of Customized OT Test Results 14
9 Outlier Test Result 15
10 Customized OT Test Results Without Outliers 16
11 ANOVA Results 17
12 Combined Dataset 17
13 *SIF* and *da/dn* Values 21
14 Shift Factor Calculation 30

LIST OF ACRONYMS

ANOVA	Analysis of Variance
CRI	Crack Resistance Index
FAA	Federal Aviation Administration
G	Fracture Energy
G_c	Critical Fracture Energy
HMA	Hot Mixed Asphalt
NAPTF	National Airport Pavement Test Facility
OT	Overlay Test
PCC	Portland Cement Concrete
RC	Reflective Cracking

EXECUTIVE SUMMARY

From 2012 through 2019, six indoor full-scale test pavements have been constructed at the Federal Aviation Administration (FAA) National Airport Pavement Test Facility (NAPTF) to study reflective cracking (RC) in airfield pavements. The core objective of the most recent full-scale indoor reflective cracking test (Phase VI) was to evaluate the effect of extreme cooling cycles on the reflection crack initiation and propagation of hot mix asphalt (HMA) overlay. The indoor Phase VI test overlay comprised two 30- by 5-ft strips constructed with the FAA standard P-401 HMA (PG 64-22). Post-construction HMA samples were extracted from the test overlay for advanced laboratory material characterization using Dynamic Modulus, Texas Overlay, and Customized Overlay tests.

HMA viscoelastic properties were obtained using the Dynamic Modulus test. |E*| master curves were obtained at four different temperatures. Because the Phase VI test overlay was constructed in two lifts, compaction effort was examined using the Texas Overlay Test (OT). Test results indicated no significant difference in the performance between the two overlay lifts. The effect of the variable occurrence of an extreme cooling cycle was examined using the Customized Overlay Test. Three sets of samples were tested assuming the extreme cooling cycle occurred at the beginning, middle, and end of every 12 loading cycles. Statistical analysis of the customized OT results suggested no significant difference in the performance among the data sets. The material properties of Paris' Law ($A=0.8197, n=0.2678$) for the RCIP-VI HMA mixture were calculated. Compared to the RCIP-V mixture, a faster crack propagation rate was observed due to extreme cooling cycles. Both fracture energy and strain energy captured the effect of the extreme cooling cycles. However, this effect diminished with each successive extreme cooling cycle. This observation was similar to the RCIP-VI indoor full-scale test. Finally, a set of shift factors was derived for failure strain and cycles to failure using both the Customized OT and full-scale test data.

1. INTRODUCTION

Resurfacing an existing portland cement concrete (PCC) pavement with a relatively thin hot mix asphalt (HMA) overlay is a popular choice of pavement rehabilitation. The primary reason for this choice is its inexpensive nature compared to a total PCC rehabilitation or total reconstruction. However, the newly constructed HMA overlay is often susceptible to cracking due to the movement of the underlying PCC slabs. These movements are the opening and closing of joints between PCC slabs which are induced by the daily variation of temperature and traffic. The bottom-up crack occurring on the HMA overlay layer due to this movement is called Reflective Cracking [1]–[8]. A large daily temperature variation combined with a very low temperature at the end of a cooling cycle presents the most critical condition for the development of reflective cracking. Low temperatures cause the HMA layer to stiffen which makes it less likely to relax under strain and results in the development of reflection cracking [9]–[11].

Reflection cracking poses a major challenge for airfield rehabilitation projects constructed using the asphalt overlay on PCC concrete, often referred to as HMA over PCC, construction method. These cracks are undesirable as water is allowed to penetrate through the cracks to the underlying layers and weaken them, subsequently compromising the integrity, strength, and ride quality of the airfield or pavement [12]. The current Federal Aviation Administration (FAA) Advisory Circular does not address reflection cracking of asphalt overlaid concrete pavements (FAA 2018) [13]. Thus a series of full-scale test pavements have been constructed, instrumented, and tested at the FAA National Airport Pavement Test Facility (NAPTF) [14]–[18] to implement reflection cracking in flexible over rigid design procedure. The most recent completed RC Indoor Phase VI full-scale test was aimed at assessing the effect of extreme cooling cycles on the crack evolution through varied displacement rates. Upon the completion of construction, field cores were extracted from the test overlay. Advanced laboratory characterization tests were then conducted at the FAA NexGen Materials Laboratory. Details of the testing program, test results, and data analysis are presented in this report.

2. OBJECTIVES

This study presents a comprehensive laboratory testing program to study the HMA material characteristics for reflection cracking, specifically:

- Obtain the viscoelastic properties using Dynamic Modulus Test.
- Assess the compaction effort using Texas Overlay Test.
- Evaluate the effect of extreme cooling cycles on the crack initiation and propagation using Customized Overlay Test.
- Establish correlations between the laboratory and full-scale tests.

3. LABORATORY TESTING PROGRAM

Table 1 summarizes the laboratory testing program. All tests were conducted on the HMA cores extracted from the Indoor Phase-VI test overlay. A total of 38 HMA cores (19 from the north side and 19 from the south side) were obtained.

Table 1. Laboratory Testing Program

Test	Standard	Properties / Parameters	Temp (°F)	Replicate	Total Samples
Dynamic Modulus	AASHTO T 342	Dynamic Modulus Master Curves	14, 39, 50, 70, 99	3	3
Texas Overlay	Tex 248-F	Fracture Energy (G_c)	77	3	6
		Fatigue Parameters (*LRR*, *CRI*)			
Customized Overlay	Yin & Mandal (2017)[19]	Fracture Parameters (G_c, *LRR*, *CRI*)	32	4	12
		Fatigue Parameters ($Nf_{(NLC)}$)			
		Strain Parameters (Initial Strain, Failure Strain, Cycles at *IF*, Strain at $Nf_{(NLC)}$)			

Note: *G_c = Critical Fracture Energy; $Nf_{(NLC)}$ = Number of Cycles at Failure Point; $Nf_{(crack)}$ = Number of Cycles representing the macro-crack in the specimen; $Nf_{(czone)}$ = Number of cycles between $Nf_{(NLC)}$; DE_{ini} = Dissipated Energy from the first loading cycle; LRR = Load Reduction Rate (%); CRI = Cracking Resistance Index; $Nf_{(75\%)}$ = Number of Cycles at 75% Load Reduction; and $Nf_{(crack)}$= Number of Cycles representing the macro-crack in the specimen; IF = Inflection Point;*

4. HMA MIX DESIGN

The HMA used in the RC Indoor Phase VI construction was designed as per the FAA standard P-401 (PG 64-22). Details of this HMA mix design are provided in table 2.

Table 2. Aggregate Gradation and Volumetric of Studied HMA Mixture

Sieve Size	Cumulative Percentage Passing	
	Blended Aggregate	P-401 Specification
¾”	100.0%	100.0%
½”	96.0%	79.0% - 99.0%
⅜”	85.0%	68.0% - 88.0%
#4	54.4%	48.0% - 68.0%
#8	38.0%	33.0% - 53.0%
#16	25.2%	20.0% - 40.0%
#30	18.5%	14.0% - 30.0%
#50	11.4%	9.0% - 21.0%
#100	7.1%	6.0% - 16.0%
#200	4.0%	3.0% - 6.0%
Fine Aggregate Angularity	47.9%	≥ 45.0%
Maximum Specific Gravity	2.709	--
Bulk Specific Gravity	2.615	--
Optimum Asphalt Content	5.30%	5.0% - 7.5%

Air Void	3.46%	2.8% - 4.2%
VMA	15.62	≥ 15.0%

5. TEST RESULTS AND DATA ANALYSIS

5.1 DYNAMIC MODULUS TEST

Dynamic modulus testing was conducted to evaluate the viscoelastic properties of the HMA mixture used in the Reflective Cracking Indoor Phase VI experiment. The test was conducted using the Universal Testing Machine (UTM-25) at the FAA NexGen Materials Laboratory as per AASHTO T 342 "Standard Method of Test for Determining Dynamic Modulus of Hot-Mix Asphalt Concrete Mixtures"[20]. The test applied a repeated load at varied frequencies to the asphalt mixture specimen over a relatively short period and measured the specimen's recoverable strain and permanent deformation. Tests were performed at five temperatures: 14, 39, 50, 70, and 99 °F using loading frequencies of 25, 10, 5, 1, 0.5, and 0.1 Hz. Dynamic modulus tests were conducted on three replicate specimens, with a diameter of 4-in. and trimmed to the height of 6-in. Appendix A provides the dimensions and volumetric properties for each of the specimens. For graphical analysis and easy interpretation of test data, $|E^*|$ master curves were generated by shifting data according to the time-temperature superposition principle described in Equation-1 [11], [21].

$$\log|E^*| = \delta + \frac{\alpha}{1 + e^{\beta + \gamma \log \omega_r}} \tag{1}$$

where, $|E^*|$ is dynamic modulus (ksi), ω_r is reduced frequency (Hz), δ is minimum value of modulus (ksi), $\delta+\alpha$ is maximum value of modulus (ksi), and β, γ are fitting parameters describing the shape of the sigmoidal function. The reduced frequency is computed using the Arrhenius function and William-Landel-Ferry equation [22], provided in Equation-2:

$$\log \omega_r = \log \omega + \frac{\Delta E_a}{19.14714}\left(\frac{1}{T} - \frac{1}{T_r}\right) \tag{2}$$

where, ω_r is reduced frequency at the reference temperature (Hz), ω is loading frequency at the test temperature (Hz), T_r is reference temperature (°F). T is test temperature (°F), and ΔE_a is activation energy treated as a fitting parameter.

Dynamic modulus master curves are most commonly developed at 68°F [23], [24]. In this study, three additional master curves were prepared at 14°F, 32°F, and 50°F that correspond to extreme low, low, and medium pavement temperatures in the field. The measured modulus and phase angle at different temperatures and frequencies are presented in table 3. Dynamic modulus master curves for four reference temperatures are presented in figure 1. Under a constant loading frequency, $|E^*|$ decreases as the temperature increases; and under a constant testing temperature, $|E^*|$ increases as the frequency increases. The changes in $|E^*|$ values with changes in temperature and frequency are as expected and so are the $|E^*|$ absolute values as provided in table 3. Phase angle values were also presented in table 3. For each sample, the phase angle value

increased with decreasing loading frequency for all temperatures. Also, the phase angle values for any particular loading frequency followed an increasing trend with the increase of temperature. Both these trends are expected as HMA material tends to become softer due to its viscoelastic nature at a lower frequency and increased temperature. This softness in-turn created more phase difference between the stress and strain.

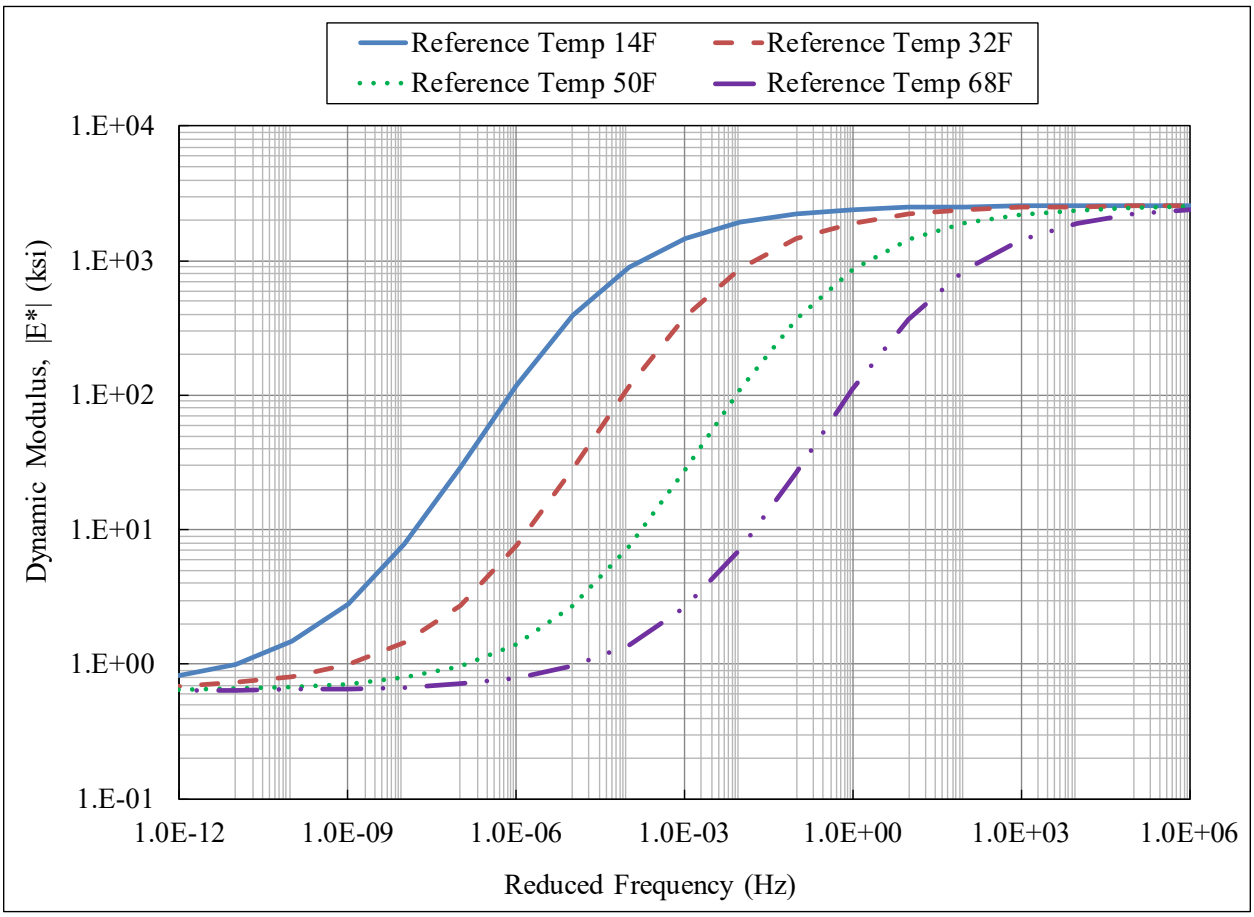

Figure 1. Dynamic Modulus Master Curves

Table 3. Modulus and Phase Angle Values of Dynamic Modulus Test

Conditions		Specimen 1		Specimen 2		Specimen 3		Average	
Test Temp (°F)	Frequency (Hz)	Modulus (ksi)	Phase (Degree)	Modulus (ksi)	Phase (Degree)	Modulus (ksi)	Phase (Degree)	Modulus (ksi)	Phase (Degree)
14	25	3084	4.55	3026	4.64	2800	5.01	2970	4.73
	10	2937	5.43	2870	5.49	2657	5.88	2821	5.60
	5	2817	6.02	2748	6.13	2538	6.59	2701	6.25
	1	2495	7.71	2426	7.92	2239	8.42	2386	8.02
	0.5	2342	8.69	2278	8.81	2098	9.35	2239	8.95
	0.1	1981	10.96	1923	11.23	1765	11.72	1890	11.30
39	25	2282	9.21	2200	9.90	2036	9.53	2173	9.55
	10	2064	10.82	1977	11.52	1834	11.19	1958	11.18
	5	1893	12.11	1804	12.91	1674	12.53	1790	12.52
	1	1492	15.74	1399	16.65	1299	16.39	1397	16.26
	0.5	1318	17.59	1232	18.49	1140	18.48	1230	18.19
	0.1	942	22.68	865	23.67	800	23.78	869	23.38
50	25	1792	12.78	1707	14.02	1625	13.38	1708	13.39
	10	1568	14.99	1471	16.39	1404	15.74	1481	15.71
	5	1394	16.74	1295	18.25	1242	17.59	1310	17.53
	1	1007	21.86	912	23.45	883	22.77	934	22.69
	0.5	857	24.03	765	25.60	746	24.99	789	24.87
	0.1	541	30.03	465	31.27	465	30.86	490	30.72
70	25	1017	22.28	906	23.89	886	23.09	936	23.09
	10	805	25.76	706	27.26	700	26.55	737	26.52
	5	658	28.23	570	29.54	572	29.02	600	28.93
	1	364	34.25	303	35.19	313	34.91	327	34.78
	0.5	270	35.83	223	36.56	231	36.46	241	36.28
	0.1	124	37.73	101	37.22	106	37.70	110	37.55
99	25	392	34.32	415	33.20	332	34.45	380	33.99
	10	261	35.94	284	34.95	220	35.52	255	35.47
	5	179	37.73	200	36.70	149	37.19	176	37.21
	1	63	48.96	76	41.71	53	41.99	64	44.22
	0.5	44	45.96	52	39.89	37	39.65	44	41.83
	0.1	20	38.28	23	33.98	16	33.75	19	35.34

Dynamic modulus tests were also done in the Indoor Phase IV and Phase V[19], [25]. The HMA mix designs for Phase V and Phase VI are the same, whereas it was different for Phase IV (table 4). Figure 2 presents a comparison of dynamic modulus master curves at reference temperatures of 14°F, 32°F, 50°F, and 68°F among the three phases. All the master curves followed the typical S-Shape of a sigmoidal function and the S-Shape part of the master curves shifted towards higher frequency at a similar rate with increasing reference temperature. The master curves for Phase IV were different and had a much narrow width compared to the other two phases. As mentioned before, Phase IV had a different mix design than Phase V and Phase VI which may be the reason for the differences (table 4). Dynamic modulus values of Phase IV were similarly compared to the other two phases at frequencies higher than 0.01Hz but were much higher at frequencies lower than 0.01Hz. The trend was the same at all the reference temperatures. This observation indicates that the Phase IV HMA mixture was much stiffer than the other phases at frequencies lower than 0.01Hz but relatively similar at frequencies higher than 0.01Hz. Lower frequency is an important factor of consideration in analyzing reflection cracking as it develops due to the very slow movement of PCC layer underneath the asphalt layer resulting from environmental temperature variation. Also, asphalt binders tend to become stiff and brittle at low temperatures [26], [27]. An already stiffer binder will increase the brittle characteristics of the asphalt mixture at low temperatures and in-turn can accelerate the development of reflective cracking. The Phase V HMA mixture was slightly updated to remedy this characteristic of the mixture and was followed in Phase VI. Due to having the same HMA mix design, dynamic modulus values for Phase V and VI exhibited slight differences. The construction of Phase-V and Phase-VI was done at different times (2018 vs 2019). Dynamic modulus values of Phase VI were higher than Phase V at a reference temperature of 14°F. The values of Phase VI were similar to Phase V at a reference temperature of 32°F. For both reference temperatures of 50°F and 68°F, Phase VI E* values were slightly lower than Phase V. This observation indicates that the Phase VI HMA mix was stiffer at temperatures below 32°F and softer at temperatures above 32°F, compared to the Phase V HMA mix. Although both Phase V and Phase VI had the same HMA mix design, the variability due to constructing at two different times (Phase V in 2018 & Phase VI in 2019) may be the reason behind the small differences in E* values.

Table 4. HMA Mix Details in Different Reflective Cracking Indoor Phases

Sieve Size	Cumulative Percentage Passing			
	RCIP-IV	RCIP-V	RCIP-VI	P-401 Specification
¾”	100.0%	100.0%	100.0%	100.0%
½”	95.4%	96.0%	96.0%	79.0% - 99.0%
⅜”	87.5%	85.0%	85.0%	68.0% - 88.0%
#4	62.9%	54.4%	54.4%	48.0% - 68.0%
#8	36.9%	38.0%	38.0%	33.0% - 53.0%
#16	22.3%	25.2%	25.2%	20.0% - 40.0%
#30	15.1%	18.5%	18.5%	14.0% - 30.0%
#50	11.5%	11.4%	11.4%	9.0% - 21.0%
#100	8.9%	7.1%	7.1%	6.0% - 16.0%
#200	5.9%	4.0%	4.0%	3.0% - 6.0%
Maximum Specific Gravity	2.628	2.709	2.709	--
Bulk Specific Gravity	2.535	2.615	2.615	--
Optimum Asphalt Content	5.00%	5.30%	5.30%	5.0% - 7.5%
Air Void	3.4%	3.5%	3.5%	2.8% - 4.2%
VMA	15.4	15.6	15.6	≥ 15.0%

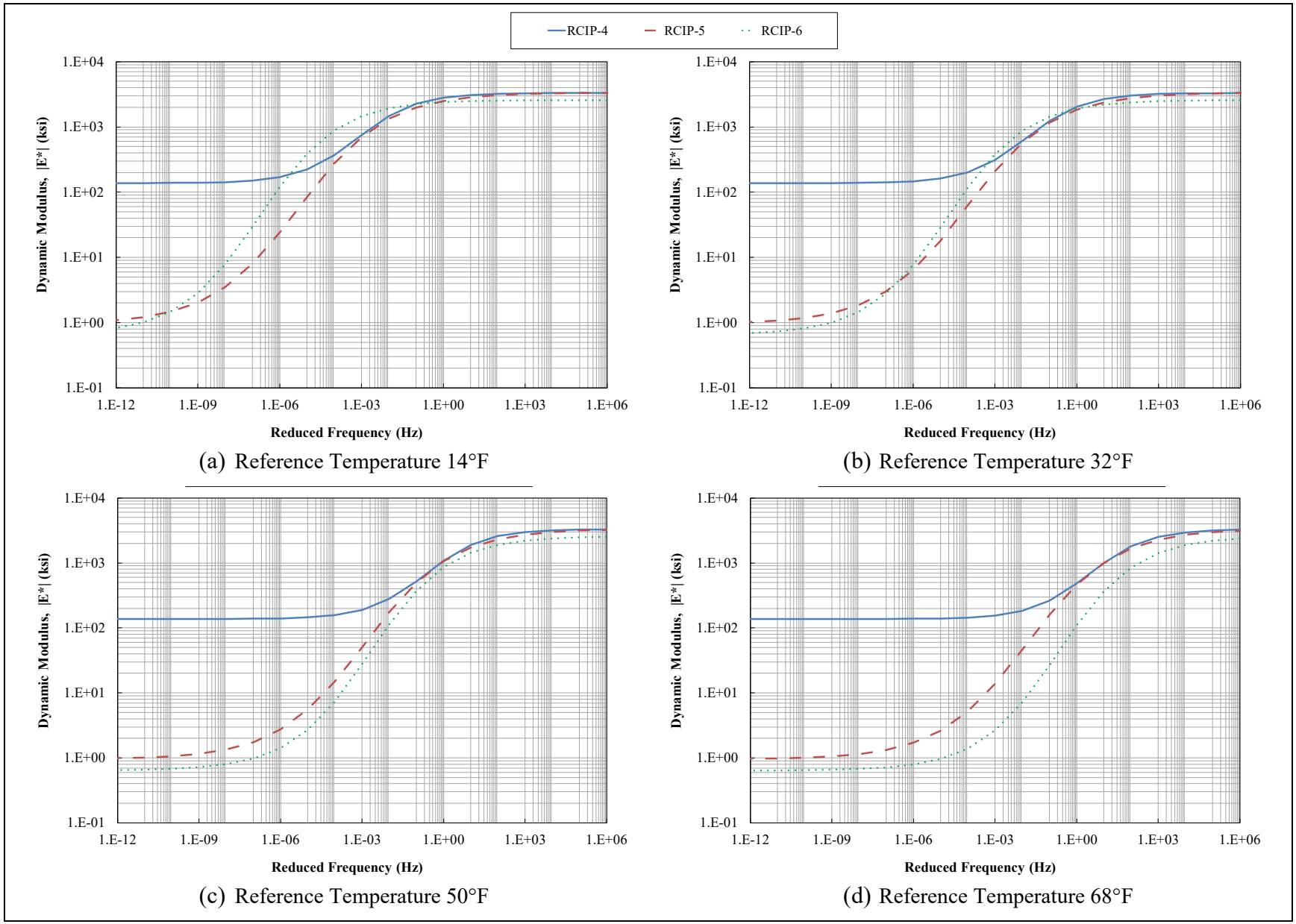

Figure 2. Dynamic Modulus Comparison Among Reflective Cracking Indoor Phases

5.2 TEXAS OVERLAY TEST

The Phase VI test overlay included two 5-in. thick HMA strips that were placed in two 2.5" lifts. The Texas Overlay Test (OT) was used to assess the compaction effort. The Texas OT is a fatigue type test and currently represents the best laboratory method to truly simulate horizontal joint movements in the joint/crack vicinity of PCC pavements [28]–[33]. The test was performed as per Tex 248-F "Test procedure for overlay test" [34]. The test is conducted in a controlled displacement mode at a repeated loading rate of one cycle per 20 seconds. (10 seconds of loading and 10 seconds of unloading) with a maximum horizontal displacement of 0.025" (0.635 mm) at the testing temperature of 77°F (25°C). The repeated loading cycles are applied until failure was achieved, which is defined by a 93 percent reduction in the maximum peak load from the first cycle or a preset value of 1000 cycles, whichever occurs first. The two most important parameters calculated from Texas OT results are the Critical Fracture Energy and Crack Resistance Index. Critical fracture energy (G_c) is defined as the energy required to initiate a crack on the bottom of the specimen at the first loading cycle during the overlay test. G_c is calculated by measuring the area under the load-displacement curve, until peak load, during the first loading cycle in the overlay test. In figure 3, the shaded area in a typical load-displacement curve during the first loading cycle (provided for demonstration purpose only) represents the G_c. This parameter characterizes the fracture properties of the specimen during the crack initiation phase. Crack resistance index (CRI) is defined as the reduction in load required to propagate cracking under the cyclic loading conditions of the overlay test. It is calculated using the β parameter from a fitted power equation representing the load reduction curve in an overlay test. An example of a fitted power equation in a typical load reduction curve is presented in figure 4. With each successive cycle in an overlay test, the peak load in the cycles gets reduced due to fatigue. This reduction in strength helps any cracks to propagate more easily through the asphalt sample. As CRI represents the reduction in load during the cyclic loading, it can be used to characterize the flexibility and fatigue properties of the specimens.

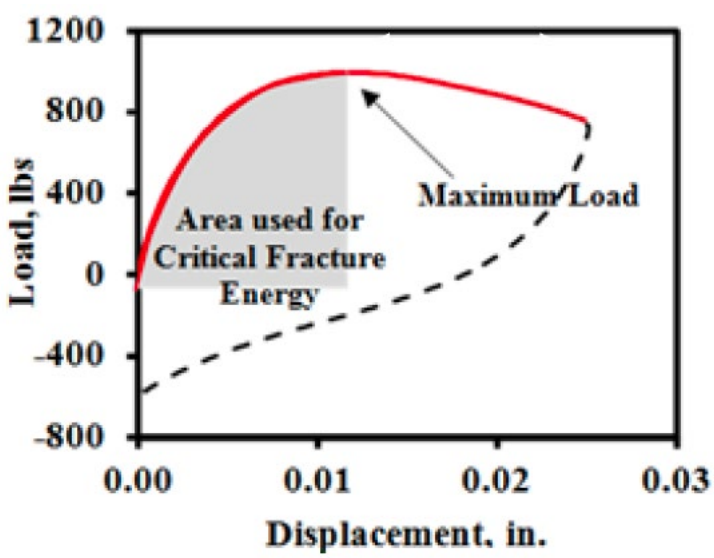

Figure 3. Area Used for Calculation of Critical Fracture Energy [34]

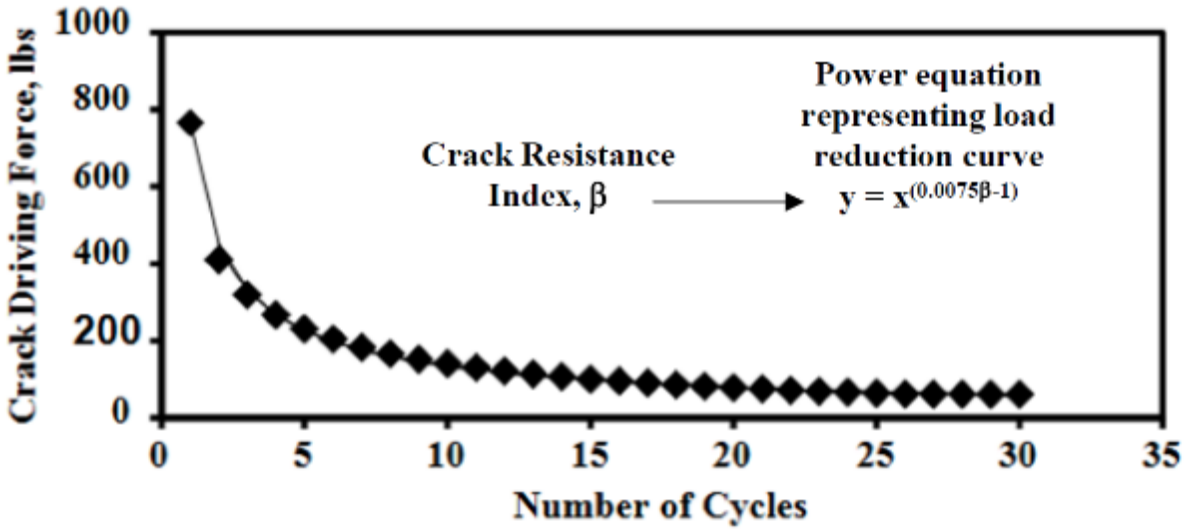

Figure 4. Calculation of Crack Resistance Index [34]

Three replicate samples from each overlay lift were tested using the Texas OT. A summary of test results is provided in table 5. Appendix B provides the dimensions and volumetric properties of the test specimens. Appendix C provides all the load vs cycle plots. Appendix D contains the pictures of all specimens.

Table 5. Texas Overlay Test Results Summary

Set	Specimen ID	Air Void (%)	Load Reduction (%)	LRR	CRI	P_{max} (kN)	N_f (Final)	G_c (J/m^2)
Bottom Lift	N3B	7.9	80	0.211	105	1.464	1000	196.9
	N4B	6.8	82	0.229	103	1.440	1000	222.3
	N16B	6.9	81	0.208	106	1.574	1000	162.6
Top Lift	N3T	7.1	79	0.206	106	1.214	1000	169.2
	N7T	7.1	81	0.215	105	1.411	1000	182.3
	N16T	5.5	76	0.175	110	1.116	1000	156.9

Note: *LRR = Load Reduction Rate; CRI = Cracking Resistance Index; P_{max} = Maximum Load at Cycle-1; N_f = Number of Cycles at Failure Point; G_c = Critical Fracture Energy;*

Two tail t-Test assuming unequal variances was performed to investigate the consistency of compaction effort. The parameters considered were the air void content, maximum load at cycle-1, load reduction percentage, load reduction rate, critical fracture energy and crack resistance index. The null hypothesis for each parameter assumed that the difference between the true mean values of the two datasets (lift) was equal to zero. Results of the statistical analysis at a 95% confidence level are presented in table 6. P-values for all the investigated parameters were found to be higher than 0.05 which represents that strong evidence is absent to reject the null hypothesis. Therefore, the compaction effort seemed consistent for both overlay lifts.

Table 6. Statistical Analysis Result for Texas Overlay Test

	Mean Values			T Value	P Value	P > 0.05 (Accept Null Hypothesis)
	Bottom Lift	Top Lift				
Air Void (%)	7.20	6.57		0.992	0.394	YES
P_{max} (kN)	1.49	1.25		2.558	0.083	YES
Load Reduction (%)	81	79		1.492	0.232	YES
LRR	0.216	0.199		1.258	0.297	YES
G_c (J/m^2)	194	169		1.302	0.284	YES
CRI	105	107		-1.258	0.297	YES

5.3 CUSTOMIZED OVERLAY TEST

The Texas OT has been successfully customized to mimic the full-scale tests at the NAPTF [19]. A test temperature of 32°F was used instead of 77°F and the maximum horizontal displacement was set at 12 mils to replicate the full-scale testing conditions. Six strain gages (three on the front and three on the back) were attached to each sample. The strain gages recorded the strains during loading at the bottom, middle, and top portion of the sample on each side. The strain gage attachment schematic and sample pictures are provided in figure 5.

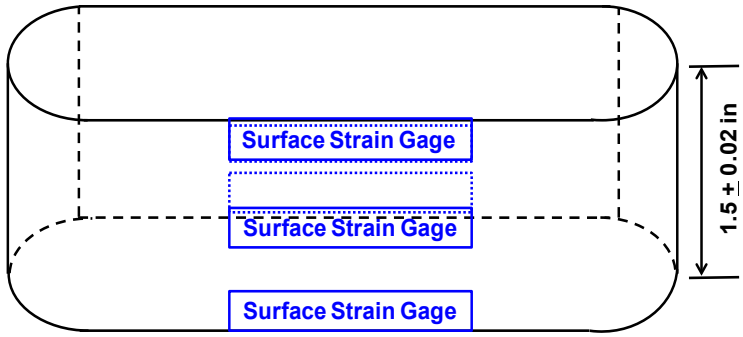

(a) Strain Gage Schematic

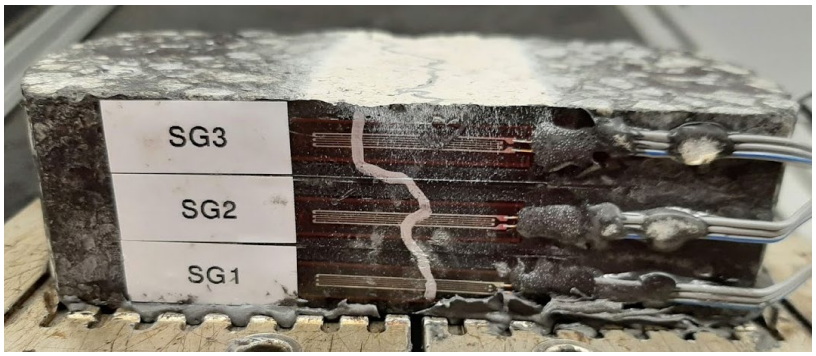

(b) Front Side

(c) Back Side

Figure 5. Customized OT Specimen Instrumentation

A haversine waveform with a rest period was applied, mimicking full-scale testing conditions. During each loading cycle, load, displacement, and strain gage responses were collected at 1 Hz using a Laboratory Virtual Instrument Engineering Workbench (LabVIEW) program. The equation describing the relationship between the joint opening and cycle time is provided in Equation 3.

$$d(t) = D sin^2\left(\frac{\pi}{2} + \frac{\pi t}{T}\right) + R \tag{3}$$

where t is the time of interest, D is the amplitude of joint opening, T is the cycle time, and R is rest period, which was included at the end of each loading cycle to allow the HMA materials to relax.

For Reflective Cracking Indoor Phase VI, the customized OT tests were conducted using a mixed displacement rate of 0.16 mil/sec and 0.32mil/sec [19]. Three separate sets of samples were tested, as shown in table 7. Set 1 included the extreme cooling at the end every 12 loading cycles, whereas, Set 2 implemented the extreme cooling in the first loading cycle. In Set 3, the extreme cooling was sandwiched in the middle. Appendix E provides the dimensions and volumetrics parameters for all customized OT specimens. Results analysis, discussion, and observation are provided in the following subsections.

Table 7. Laboratory Test Plan to Study Occurrence of an Extreme Cooling Cycle using the Customized OT

Testing Suite	Standard	Cycles	Cycle Time (Sec)	Rest Period (Sec)	Displacement Rate (mills/Sec)	Replicates
Extreme Set - 1		1st – 11th	150	150	0.16	4
		12th	75	150	0.32	
Extreme Set - 2		1st	75	150	0.32	4
		2nd - 12th	150	150	0.16	
Extreme Set - 3		1st – 6th	150	150	0.16	4
		7th	75	150	0.32	
		8th - 12th	150	150	0.16	

5.3.1 Cycle to Failure and Crack Resistance Index

Cycle to failure ($N_{f(Final)}$) is an indicator to understand crack propagation within any HMA mix. Similar to Reflective Cracking Indoor Phase IV and V, cycles to failure of the customized OT samples were determined using the "Normalized Load x Cycle" or NLC method [19], [25], [33]. In this method, the failure point can be defined as the transition from micro-crack to macro-crack propagation. In the first step, NLC for every cycle is calculated (Equation 4). Then it is plotted against the number of cycles. Finally, the failure point can be selected as the peak point on the plot.

$$NLC = \frac{P_i \times N_i}{P_1 \times N_1} \tag{4}$$

Where, NLC = Normalized Load x Cycle, P_i = Peak load at cycle number i (lb), P_1 = Peak load at cycle number 1 (lb), N_i = Cycle number i, and N_1 = Cycle number at which P_1 is estimated. A detailed discussion on the aforementioned process can be found elsewhere [19].

Crack Resistance Index (*CRI*) is another good measure to evaluate crack propagation in the OT test. Table 8 presents a summary of customized OT test results for all data sets. Appendix F provides all the NLC plots, and Appendix G provides all the peak load vs cycle plots. The coefficient of variation (COV) of the "Cycle to Failure" values are very high: 70.0%, 139.2%, and

97.9% for extreme set 1, 2, and 3, respectively. To remedy any possible bias, an outlier test was performed as per ASTM E 178[35]. The test was performed at a 99% confidence level to find outliers on both the high and low sides of the values. Any test observation will be considered an outlier if its test criterion (T_n) value becomes higher than the critical T value on either the high or low side. Table 9 provides the results of the outlier analysis. Samples S2, N10, and N12 had their test criterion value (T_n) higher than the critical T value at a 99% confidence level and hence were considered outliers. Results from these three samples were discarded from any further analysis. Table 10 presents the summary of customized OT results showing much-improved COV values.

Table 8. Summary of Customized OT Test Results

Extreme Set - 1						
Sample ID	S2	S3	S7	N8	Average	COV (%)
$N_{f(Final)}$	1475	500	770	260	751	70.0
Load Reduction @ $N_{f(Final)}$ (%)	83	80	71	59	73	14.7
Load Reduction Rate	0.376	0.413	0.323	0.584	0.424	26.6
Crack Resistance Index	83	78	90	55	77	19.8
Extreme Set - 2						
Sample ID	S10	S11	N9	N10	Average	COV (%)
$N_{f(Final)}$	200	160	160	1760	570	139.2
Load Reduction @ $N_{f(Final)}$ (%)	75	66	68	85	74	11.7
Load Reduction Rate	0.353	0.719	0.622	0.365	0.515	35.8
Crack Resistance Index	86	37	50	85	65	38.5
Extreme Set - 3						
Sample ID	S14	N12	N17	N18	Average	COV (%)
$N_{f(Final)}$	280	2084	270	850	871	97.9
Load Reduction @ $N_{f(Final)}$ (%)	69	93	88	94	86	13.5
Load Reduction Rate	0.628	0.298	0.430	0.352	0.427	33.9
Crack Resistance Index	50	94	76	86	77	25.0

Table 9. Outlier Test Result

Set	Sample ID	$N_{f(Final)}$	Average	Standard Deviation	Test Criterion (T_n)		Critical T	Outlier?
					High Side	Low Side		
Extreme Set 1	N8	260	751.3	455.1	-1.0793	1.0793	1.4925	NO
	S3	500			-0.5520	0.5520		NO
	S7	770			0.0412	-0.0412		NO
	S2	**1475**			**1.5902**	-1.5902		**YES**
Extreme Set 2	N9	160	570.0	687.2	-0.5966	0.5966		NO
	S11	160			-0.5966	0.5966		NO
	S10	200			-0.5384	0.5384		NO
	N10	**1760**			**1.7316**	-1.7316		**YES**
Extreme Set 3	N17	270	871	738.6	-0.8137	0.8137		NO
	S14	280			-0.8001	0.8001		NO
	N18	850			-0.0284	0.0284		NO
	N12	**2084**			**1.6422**	-1.6422		**YES**

Table 10. Customized OT Test Results Without Outliers

Extreme Set - 1						
Sample ID	--	S3	S7	N8	Average	COV (%)
$N_{f(Final)}$	--	500	770	260	510	50.0
Load Reduction @ $N_{f(Final)}$ (%)	--	80	71	59	70	15.1
Load Reduction Rate	--	0.413	0.323	0.584	0.440	30.1
Crack Resistance Index	--	78	90	55	74	23.9
Extreme Set - 2						
Sample ID	S10	S11	N9	--	Average	COV (%)
$N_{f(Final)}$	200	160	160	--	173	13.3
Load Reduction @ $N_{f(Final)}$ (%)	75	66	68	--	70	6.8
Load Reduction Rate	0.353	0.719	0.622	--	0.565	33.6
Crack Resistance Index	86	37	50	--	58	44.0
Extreme Set - 3						
Sample ID	S14	--	N17	N18	Average	COV (%)
$N_{f(Final)}$	280	--	270	850	467	71.1
Load Reduction @ $N_{f(Final)}$ (%)	69	--	88	94	84	15.6
Load Reduction Rate	0.628	--	0.430	0.352	0.470	30.3
Crack Resistance Index	50	--	76	86	71	26.3

The main objective of the Customized OT test was to evaluate the effect of different occurrences of extreme cooling on the crack initiation and propagation. An Analysis of Variance (ANOVA) test was performed to test the validity of such an assumption. “Cycle to Failure” and “Crack Resistance Index” from table 10 were used in the analysis. For each of these two parameters, the confidence interval was set at 95% assuming equal variances. The null hypothesis assumed that all means were equal. ANOVA results are presented in table 11. The *p*-Value for both parameters were above 0.05, which indicates that there was not enough evidence present to reject the null hypothesis. Therefore, the effect of the different occurrences of the extreme cooling cycle on crack initiation and propagation was not statistically significant. All the proceeding analysis are then performed considering all data points from 3 extreme sets, as shown in table 12.

Table 11. ANOVA Results

Parameter	Factor	Mean	F-Value	p-Value	Accept Null Hypothesis (P > 0.05?)
Cycles to Failure	Extreme Set-1	510	1.72	0.257	YES
	Extreme Set-2	173			
	Extreme Set-3	467			
Crack Resistance Index	Extreme Set-1	223	0.53	0.614	YES
	Extreme Set-2	173			
	Extreme Set-3	212			

Table 12. Combined Dataset

Sample ID	Cycle to Failure	Crack Resistance Index	Load Reduction Rate
S3	500	78	0.413
S7	770	90	0.323
N8	260	55	0.584
S10	200	86	0.353
S11	160	37	0.719
N9	160	50	0.622
S14	280	50	0.628
N17	270	76	0.43
N18	850	86	0.352
Average	383	68	0.49
COV (%)	68.6	29.0	29.9

5.3.2 Strain Analysis

As demonstrated in figure 5, each customized OT sample had six strain gages (three on each side) to monitor and capture crack initiation and propagation. Readings from the bottom-most strain gages provided information on the bottom-up crack initiation whereas the upper four strain gages provided information on the crack propagation. A similar process to Reflective Cracking Phase IV and Phase V data analysis was used in Phase VI to identify strain gage failure. The determination of failure strain and failure cycle depended on the crack location with respect to the strain gage. There are three possible scenarios:

1. If the gage is on the crack path, a continuous rise in tension will be recorded as the gage

bridges the crack and eventually goes out of range.

2. If the gage is off but close to the crack path (within 0.5”), a significant drop in tension will be recorded as the strain energy is released by the crack formation.
3. If the gage is far away from the crack path (more than 0.5”), a constant low magnitude tensile strain will be recorded.

Only the first two scenarios were considered in the strain analysis. Finally, the failure point was determined by the inflection point from the strain vs cycle plot or by the cycle number. A more detailed discussion on this process is available in the Reflective Cracking Phase IV Material Characterization Report [19]. Appendix H provides the strain gage data of all customized OT samples, and Appendix I shows pictures of all test samples. Failure strain data of all test samples can be found in Appendix J. The average failure strain and failure cycle are presented in figure 6 and figure 7, respectively. The bottom strain gage had the highest failure strain and lowest failure cycle value, indicating the greatest potential of reflection cracks. Interestingly, the error bars in both plots revealed an increase in the variation of both the failure strain and failure cycle as the crack progressed to the top. The standard deviation values for both failure strain and failure cycle were lowest for the bottom strain gage and progressively increased for the middle and top strain gages. This variation was caused by the directions of crack propagation. Bottom-up cracks usually started from the center of the sample where the displacement-controlled loading was applied. Afterward, the cracks did not always follow an upright angle towards the sample surface.

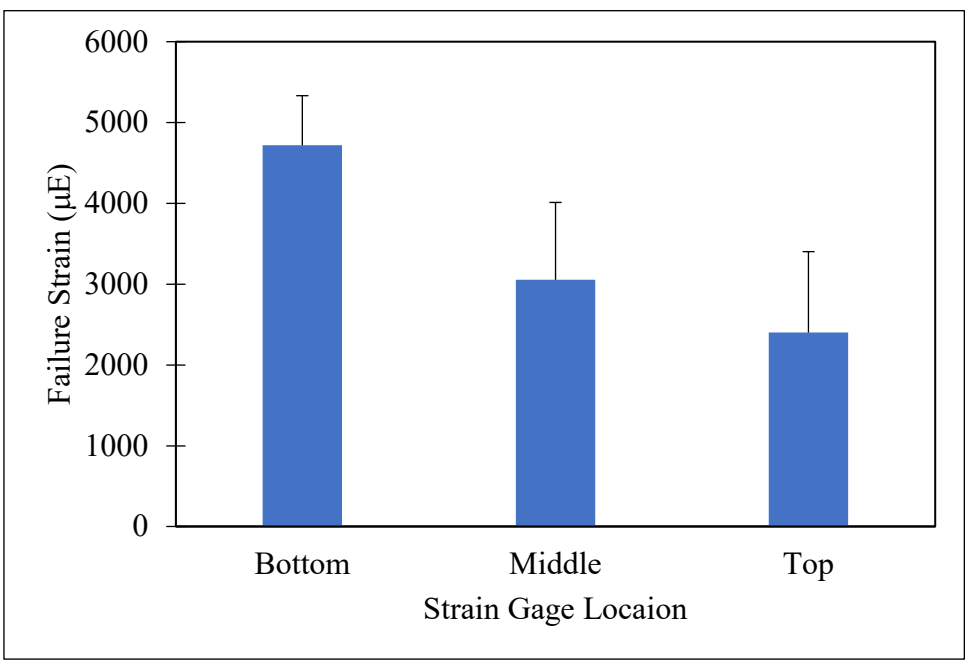

Figure 6. Failure Strain

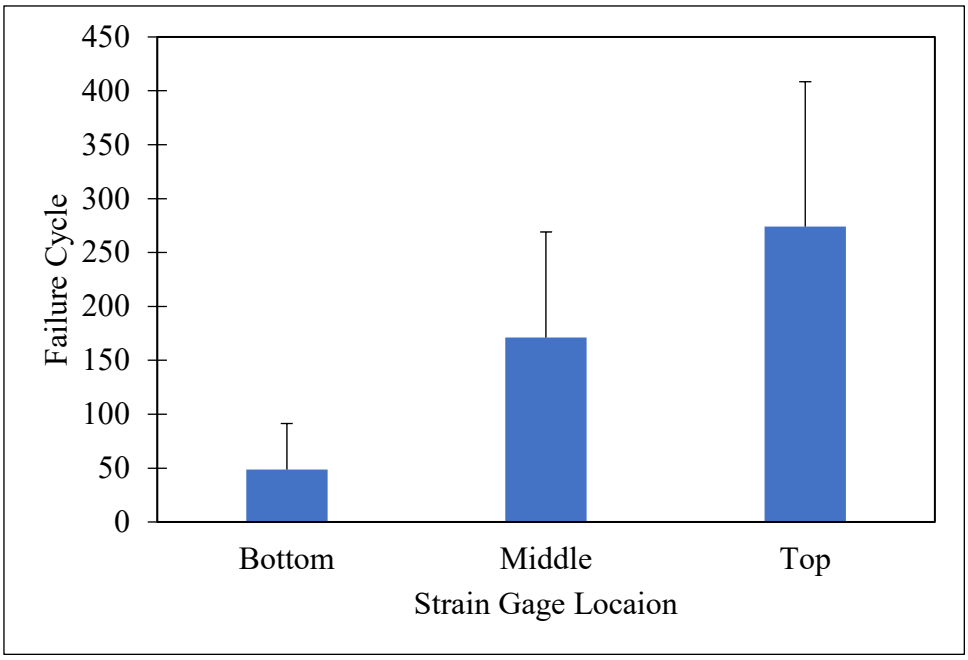

Figure 7. Failure Cycle

An effort was made to compare the failure strain of Phase VI test samples with Phase IV and V studies (figure 8). Although Phase IV used the same testing parameters as the Extreme Set 1 of Phase VI, the HMA mix design was different. Phase V and VI shared the same HMA mix design but different testing parameters. Therefore, the control set (150s loading cycle and 150s rest period) from Phase V was selected for comparison purposes. For all cases, the bottom strain gage had the highest failure strains whereas the top strain gage had the lowest failure strains. Because Phase VI had extreme cooling cycles, the failure strain at all locations was highest among the three phases.

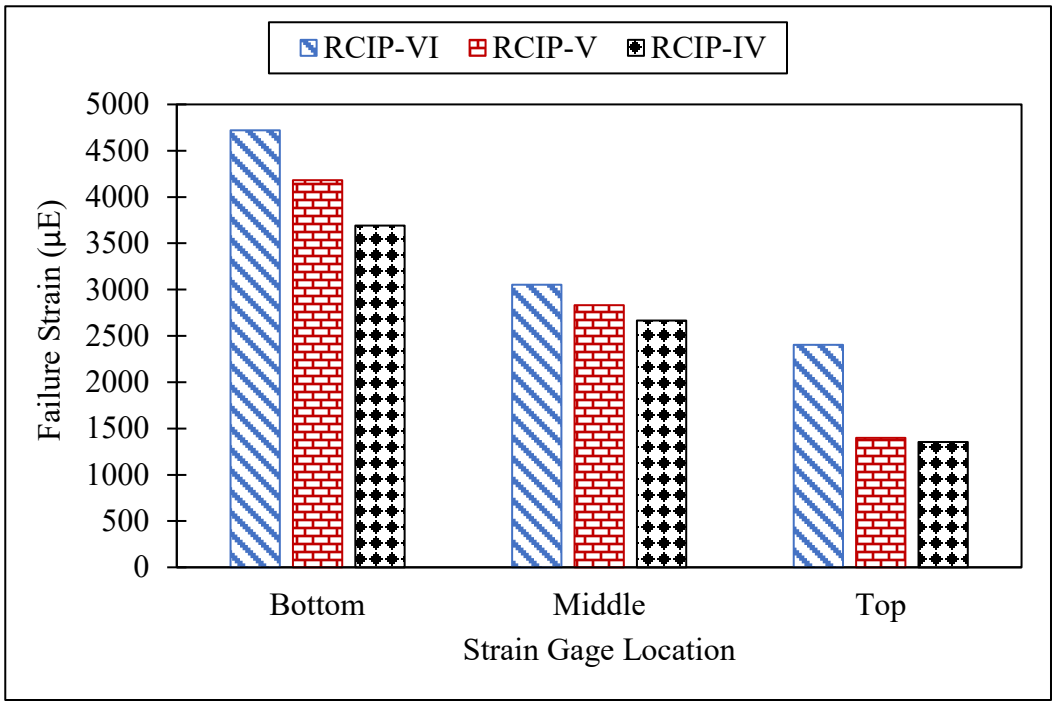

Figure 8. Failure Strain Comparison

5.3.3 Paris Law

Paris and Erdogan Law [36] is a crack growth equation that provides the rate of growth of a fatigue crack by relating it to the stress intensity factor (SIF). The crack growth and SIF equations are given by,

$$\left(\frac{da}{dN}\right) = A(\Delta K)^n \tag{9}$$

$$SIF = 0.2911 \times E \times MOD \times c^{-0.459} \tag{10}$$

where, a is the crack length, N is the number of loading cycles, da/dN is the fatigue growth rate, ΔK is the change in SIF, A & n are material properties which are obtained experimentally, SIF is stress intensity factor in $ksi \times mills^{0.5}$, E is HMA modulus in ksi, MOD is maximum opening displacement in $mills$, c is crack length in $mills$. This cracking model has been successfully implemented by various pavement researches to investigate the reflective crack growth of HMA overlays [37]–[44]. Zhou et al (2009) [42] proposed an empirical equation to calculate SIF (equation-10) for any modulus (E) and maximum crack opening (MOD) which was derived using a 2D finite element program named "2D-CrackPro". This method was previously used in the RCIP-V material characterization study to calculate the material properties A and n [25]. An effort was made in this study to calculate the same material properties of the RCIP-VI HMA mixture.

To calculate *SIF*, it is important to know the modulus value (*E*). Similar to RCIP-V [25], the value of *E* was calculated (=2298 ksi) from the master curve (figure 1) at 32ºF and 25Hz. The value of *MOD* was 0.3048mm (12 mills). Strain gage reading and location were used to calculate the number of cycles (*N*) and crack length (*c*), respectively. The *N* corresponded to the cycle number at which the respective strain gage failed, whereas, the crack length was taken as the distance of gage of interest from the bottom of the specimen. Then *da/dN* (which is the slope of crack length and number of cycles) was calculated. Because only two *da/dN* points can be estimated from three gage locations, for the third point, the 1st loading cycle was assumed to introduce a crack length of 0.01 mills. Table 13 presents the average *SIF* and corresponding *da/dN* values for the Customized OT samples. The material properties *A* and *n* were calculated 0.8197 and 0.2678 respectively.

Figure 9 presents the material properties and crack propagation comparison between Phase-V and Phase-VI. Both phases had the same HMA mixture, but the testing parameters were different. Figure 9 clearly shows the effect extreme cooling cycles had on the crack propagation. For a constant SIF, the crack propagation rate in phase-VI was much faster than Phase-V.

Table 13. *SIF* and *da/dn* Values

Crack Length	Crack Length	SIF	Failure Cycle	d*a*/d*N*	Material Properties
(inch)	(mills)	(ksi×mills$^{0.5}$)		(mills/cycle)	*A, n*
0.00001	0.01	66457.33	1	--	0.8197, 0.2678
0.22	220	675.10	49	4.58	
0.75	750	384.49	172	4.31	
1.5	1500	279.72	383	3.55	

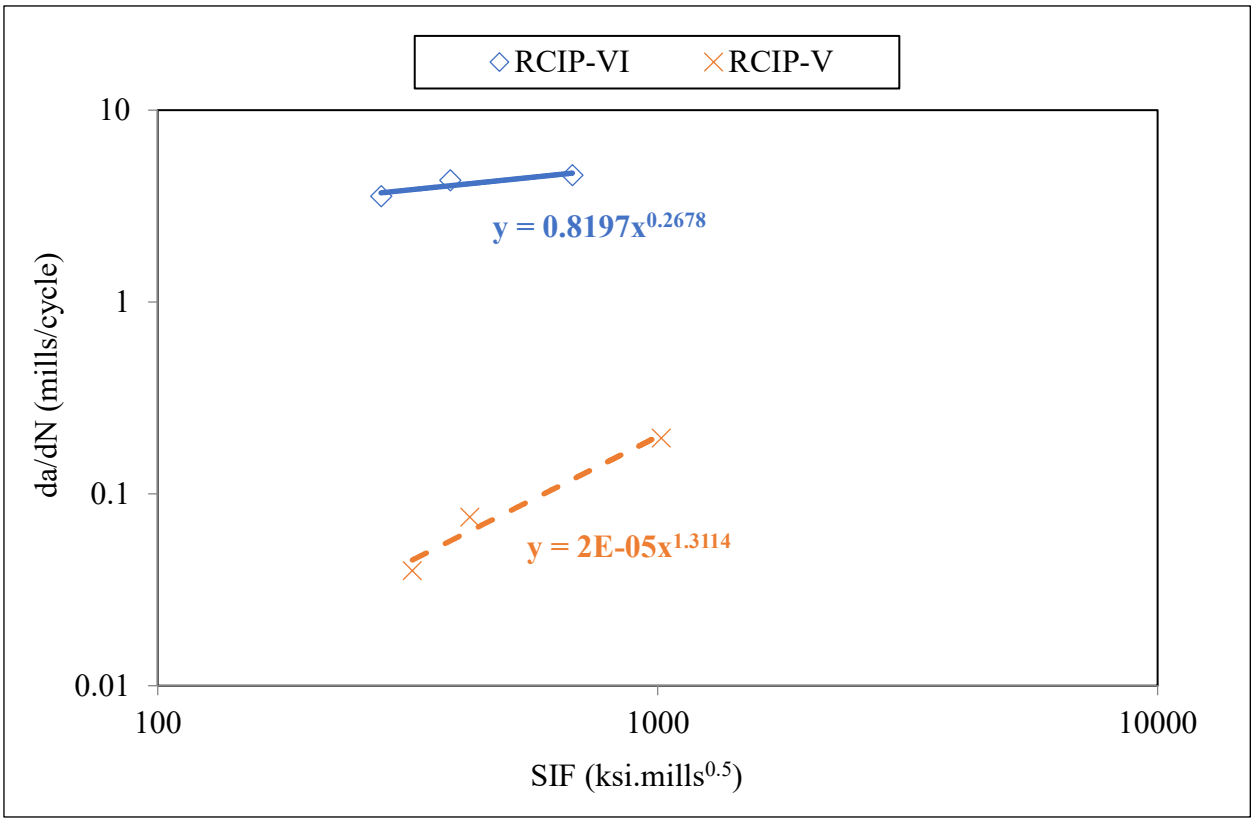

Figure 9. d*a*/d*N* vs. SIF

6. EFFECT OF EXTREME COOLING CYCLE

6.1 EFFECT ON FRACTURE ENERGY

Fracture energy is a measure of load with respect to displacement. A typical plot of fracture energy vs cycle number from RCIP-VI Customized OT test is provided in figure 10 for demonstration purposes. During each extreme loading cycle, a sudden increase in load resulted in increased fracture energy, as shown in the zoomed-in section of figure 10. Figure 11 presents the fracture energy increase and decrease percentage for each extreme cooling cycle. These rates were calculated using Equation-11 and Equation-12, respectively.

$$(\%)\ Increase\ in\ G = \frac{G_{extreme} - G_{preceeding}}{G_{preceeding}} \times 100 \qquad (11)$$

$$(\%)\ Decrease\ in\ G = \frac{G_{extreme} - G_{succeeding}}{G_{preceeding}} \times 100 \qquad (12)$$

where $G_{extreme}$ is the fracture energy during the extreme cooling cycle, $G_{preceeding}$ is the fracture energy preceding the extreme cooling cycle and $G_{succeeding}$ is the fracture energy succeeding the extreme cooling cycle. As seen from figure 11, both increase and decrease rates had a slow decay with each successive extreme cooling cycle.

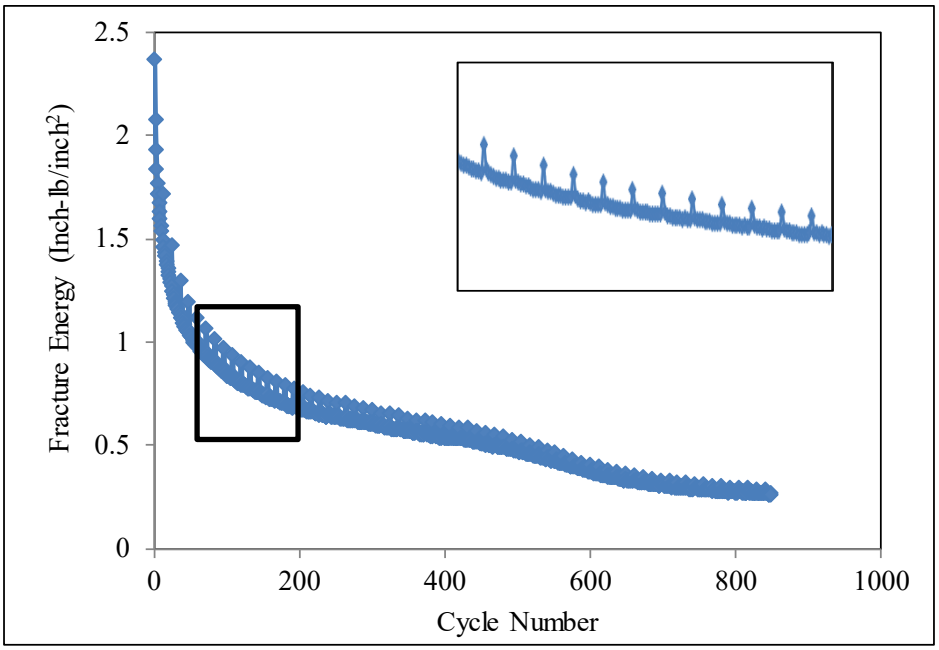

Figure 10. Typical Plot of Fracture Energy vs Cycle Number

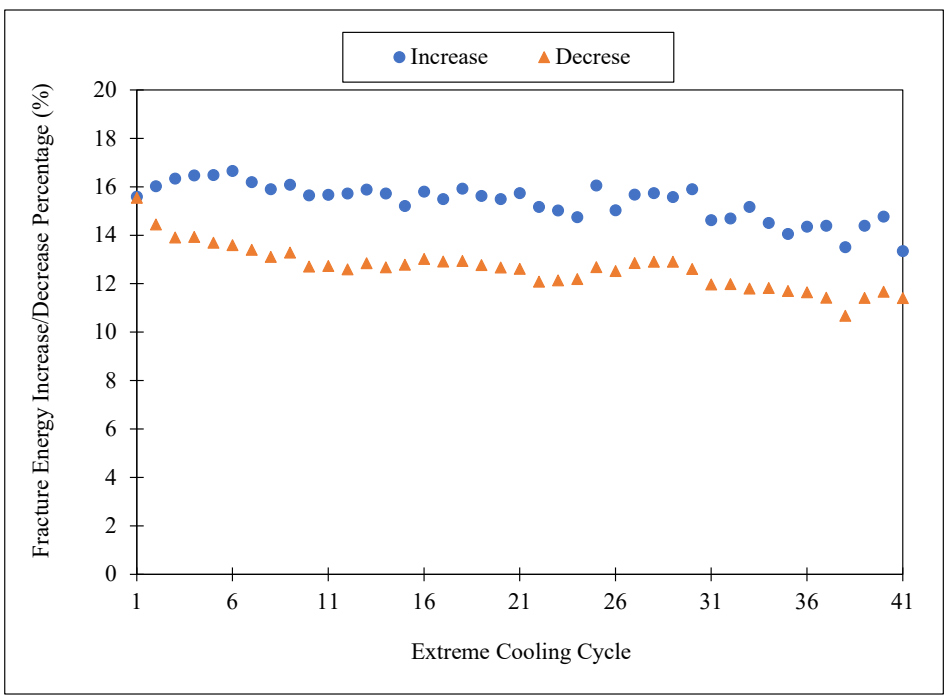

Figure 11. Fracture Energy Increase/Decrease Percentage for Each Extreme Cooling Cycle

6.2 EFFECT ON STRAIN ENERGY

Strain energy is a combined measure of both load and strain response with respect to displacement. Strain Energy is defined as elastic energy stored in the body under loading [45], [46]. From the basic principles of work and energy, strain energy density (U') is defined as:

$$U' = \frac{1}{2}\sigma\varepsilon \tag{13}$$

where, σ is the stress and ε is the strain. Internal Strain Energy per unit area in the undamaged system ($U_{Undamaged}$) can be defined as:

$$U_{Undamaged} = \frac{1}{2}\sigma\varepsilon d \tag{14}$$

where, d is the depth of an undamaged overlay system with zero crack length. Considering unit area, internal Strain Energy associated with a damaged system is given by Equation 15.

$$U_{Damaged} = \frac{1}{2}\sigma\varepsilon(d') \tag{15}$$

where, d' is the effective depth. Internal Strain Energy is reduced as a result of crack propagation. The complete steps to determine the $U_{Undamaged}$ and $U_{Damaged}$ are thoroughly described in RCIP-VI Comprehensive Test Report [47]. Similar to the fracture energy analysis, strain energy showed a sharp jump during each extreme cooling cycle (figure 12). The increase and decrease percentage in strain energy during each extreme cooling cycle were calculated using Equation-16 and Equation-17, respectively.

$$(\%)\ Increase\ in\ U = \frac{U_{extreme} - U_{preceeding}}{U_{preceeding}} \times 100 \tag{16}$$

$$(\%)\ Decrease\ in\ U = \frac{U_{extreme} - U_{succeeding}}{U_{preceeding}} \times 100 \tag{17}$$

Where, $U_{extreme}$ is the strain energy during the extreme cooling cycle, $U_{preceeding}$ is the strain energy preceding the extreme cooling cycle and $U_{succeeding}$ is the strain energy succeeding the extreme cooling cycle. Figure 13 presents the strain energy increase and decrease percentage for each extreme cooling cycle. Although the strain percentages had more fluctuation than fracture percentages, they followed a decreasing trend with the progression of extreme cooling cycles.

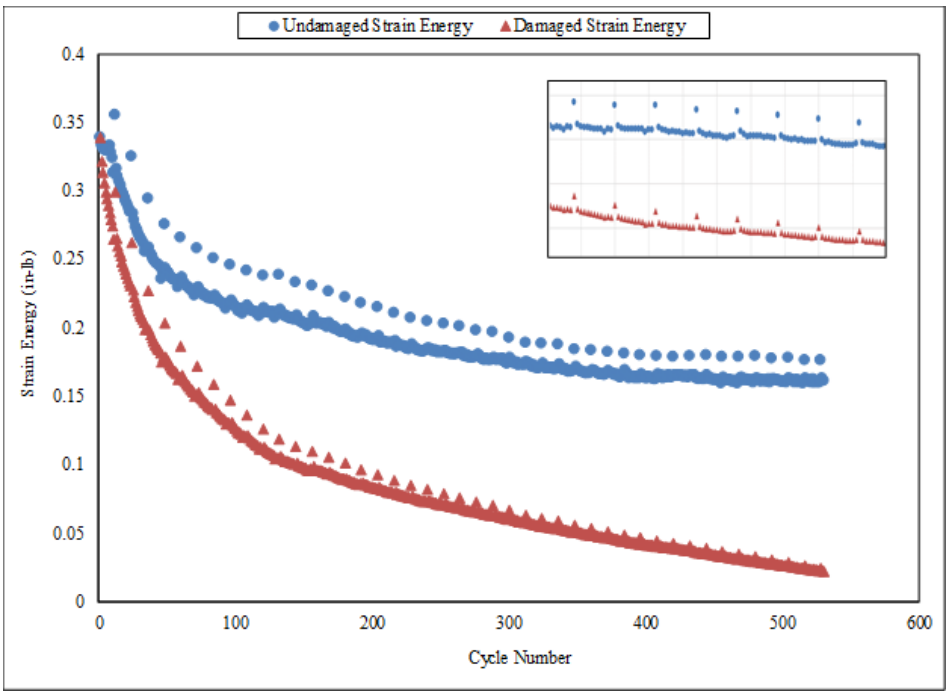

Figure 12. Typical Plot of Strain Energy vs Cycle Number

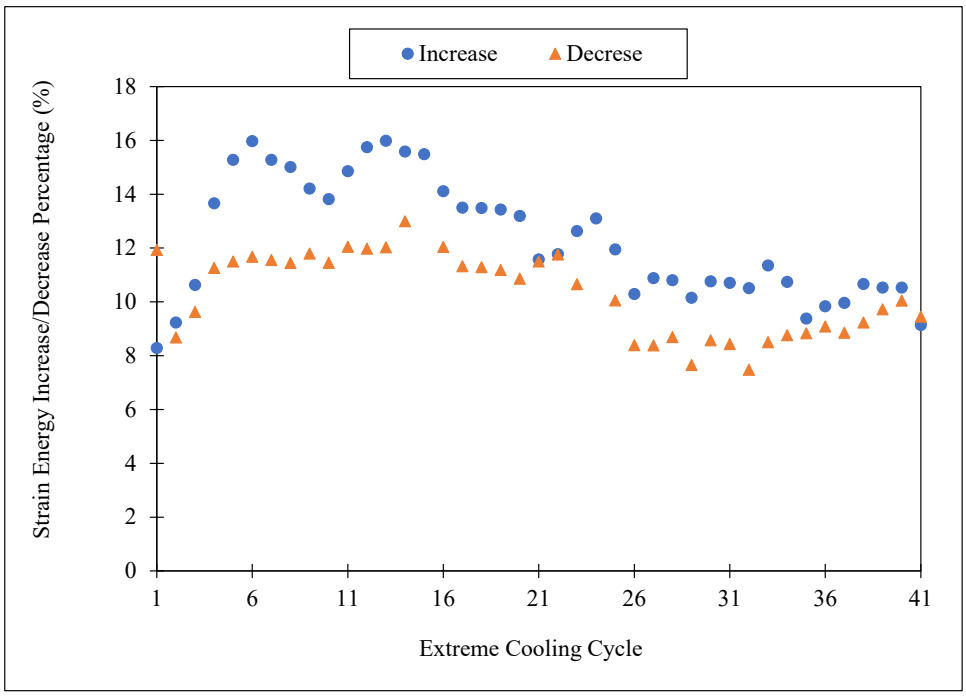

Figure 13. Strain Energy Increase/Decrease Percentage for Each Extreme Cooling Cycle

7. FULL-SCALE VS. CUSTOMIZED OT TESTS

Comparisons between the full-scale tests and laboratory tests were made on the failure strain (figure 14), and strain gage failure cycle (figure 15). Good correlations were observed in all comparisons providing R^2 values of 0.929 and 0.985 respectively.

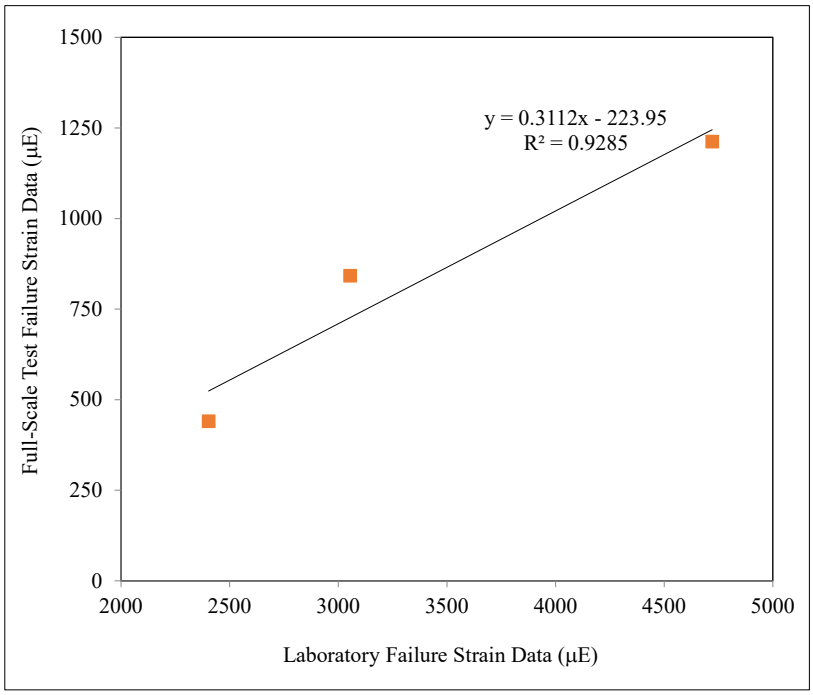

Figure 14. Failure Strain Comparison between Full-Scale Test and Customized OT

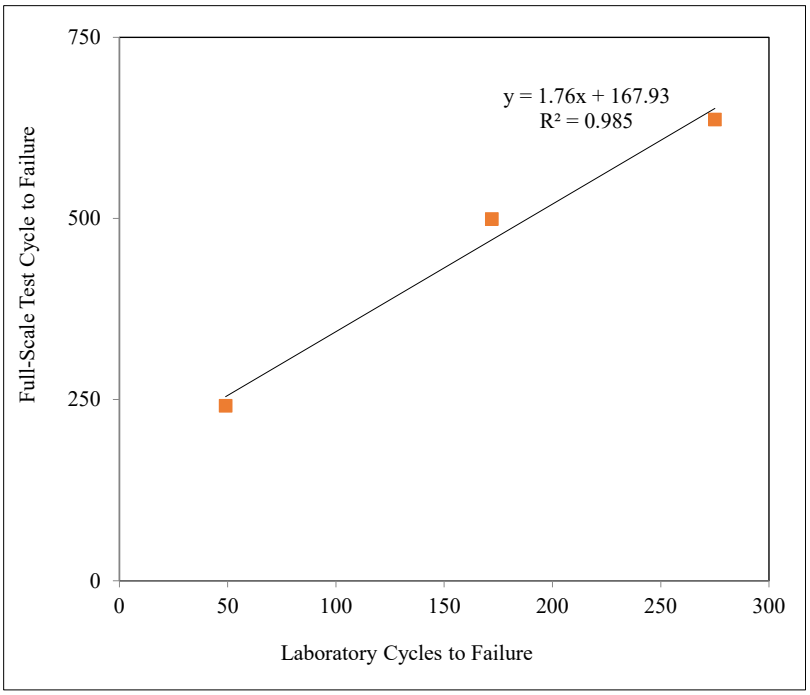

Figure 15. Failure Cycle Comparison between Full-Scale Test and Customized OT

The rate of increase and decrease in the fracture energy were compared between RCIP-VI indoor full-scale test and RCIP-VI Customized OT. Due to the difference in the implementation of extreme cooling cycles (30 of 360 cycles vs. 1 of 12 cycles), only the fracture energy increase and decrease percentage after the 1st extreme cooling cycle was calculated and presented in figure 16. Full-scale test and Customized OT results had a comparable increase and decrease rates.

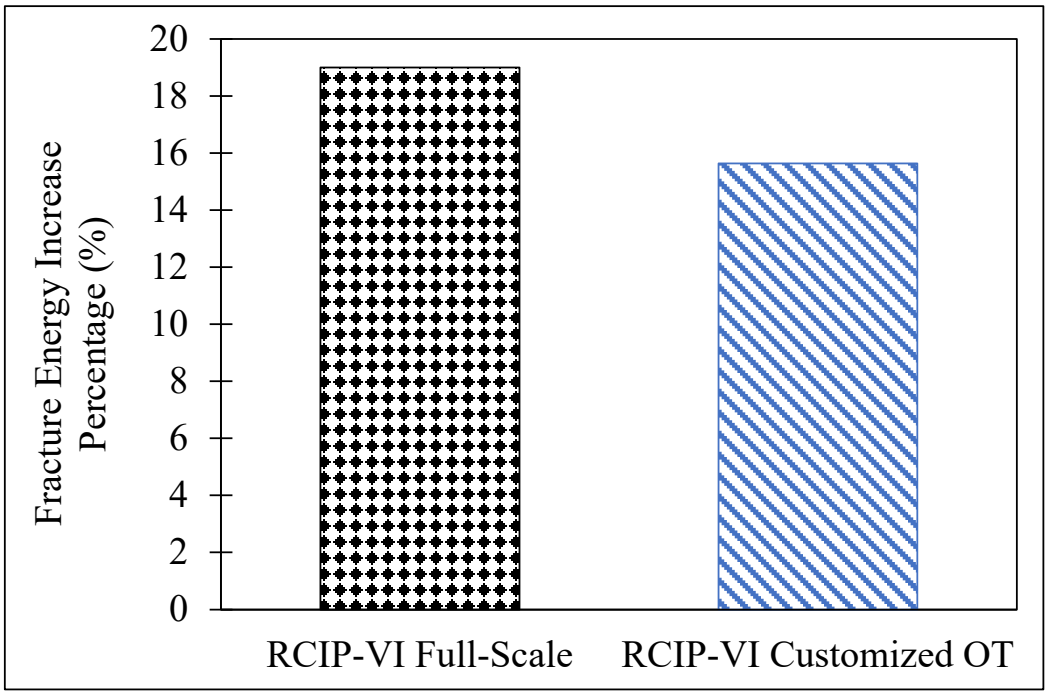

(a) Fracture Energy Increase

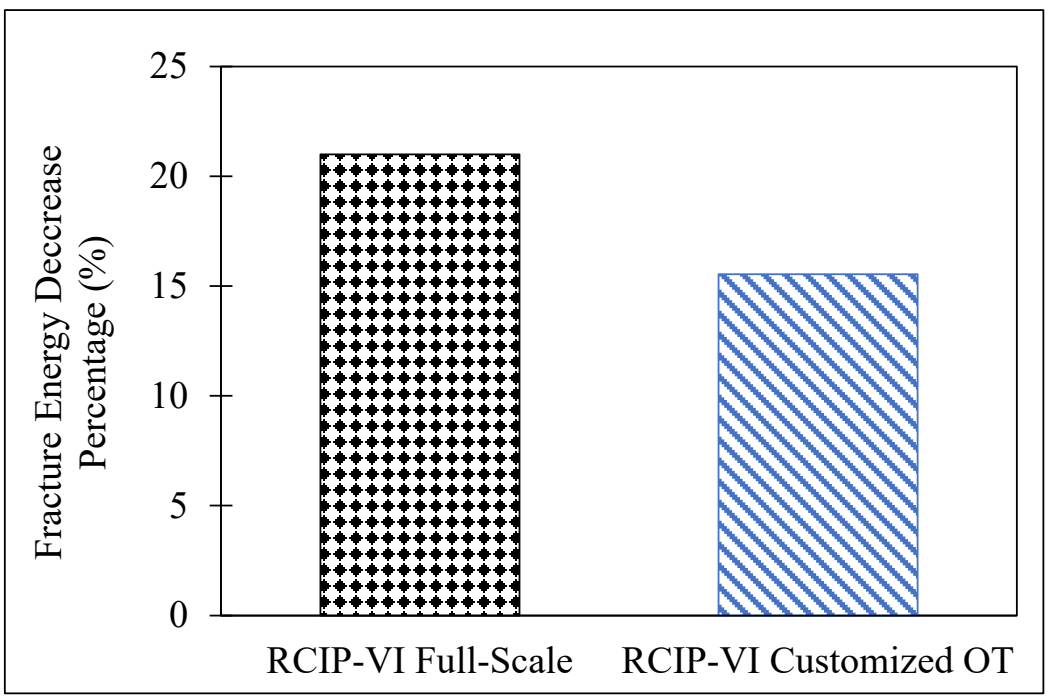

(b) Fracture Energy Decrease

Figure 16. Fracture Energy Increase/Decrease After 1st Extreme Cooling Cycle

Comparison of strain energy increase and decrease percentage after the 1st extreme cooling cycle between RCIP-VI Full-Scale test and RCIP-VI Customized OT are presented in figure 17. While the increase rates were close, the full-scale test concluded a high energy release and therefore

higher strain energy decrease rate than the Customized OT results.

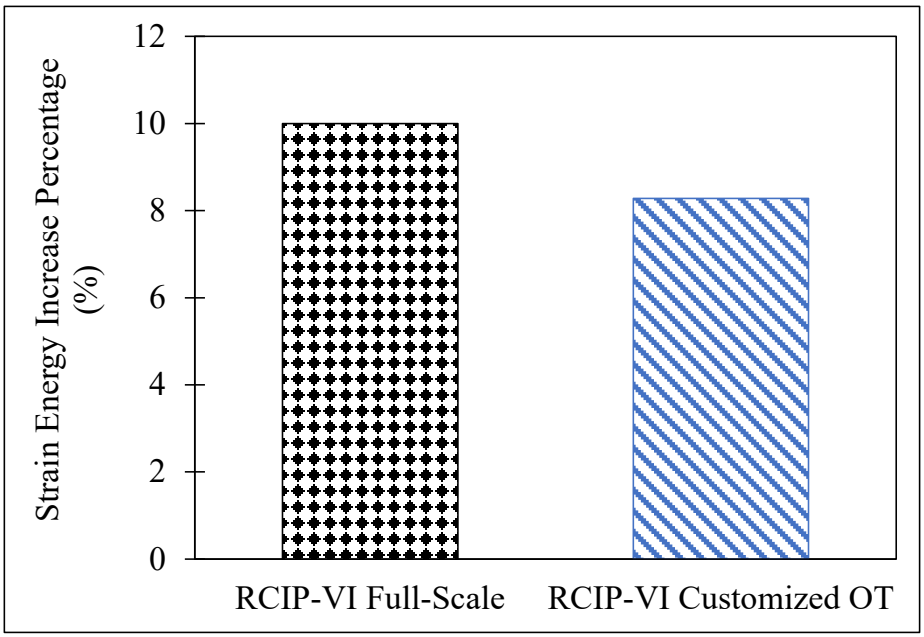

(a) Strain Energy Increase

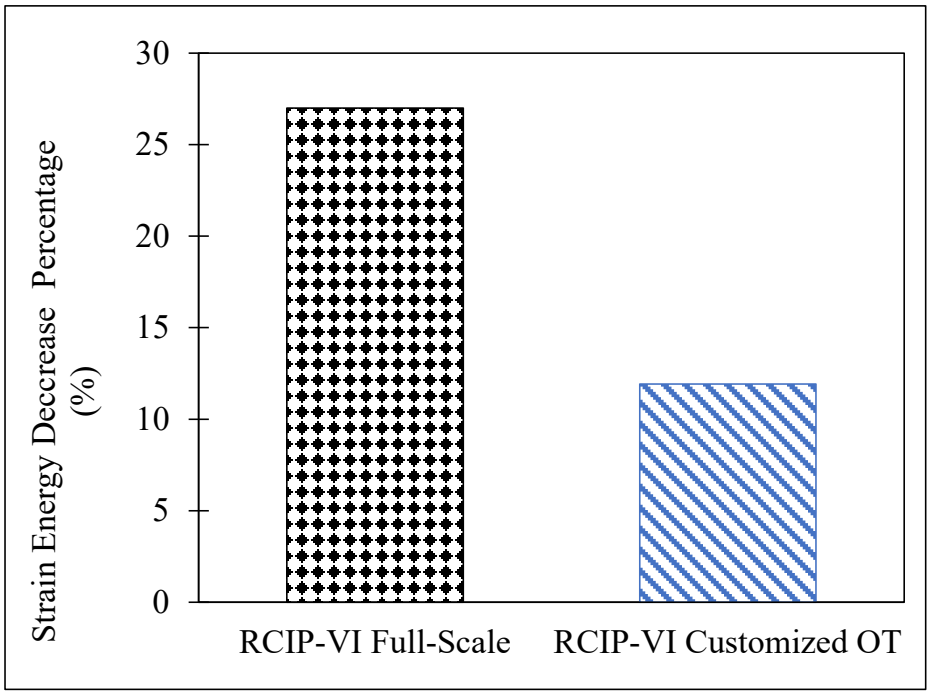

(b) Strain Energy Decrease

Figure 17. Strain Energy Increase/Decrease After 1st Extreme Cooling Cycle

A set of shift factors, which are the ratio of laboratory testing value to full-scale testing value, were developed to correlate full-scale and laboratory test results for both RCIP-V and RCIP-VI.

Although both these phases had the same HMA mixtures, the overlay thickness and testing recipe were different. For comparison purposes, results from the south overlay strip of RCIP-V which was 6-inch in thickness was used to compare the shift factors between the two phases. The shift factors are presented in table 14. Irrespective of overlay thickness and testing recipe differences, the shift factors were found to be quite close.

Table 14. Shift Factor Calculation

Phase	Test	Failure Strain			Strain Gage Failure Cycle		
		Bottom Gage	Middle Gage	Top Gage	Bottom Gage	Middle Gage	Top Gage
RCIP-VI	Full-Scale Test (5" HMA Overlay)	1213	842	441	241	499	637
	Customized OT (1.5" HMA)	4721	3054	2403	49	172	275
	Shift Factor	3.89	3.63	5.45	0.20	0.34	0.43
RCIP-V	Full-Scale Test (6" HMA Overlay)	1391	804.5	722.5	551	477.5	609
	Customized OT (1.5" HMA)	4183	2831	1400	84	172	207
	Shift Factor	3.01	3.52	1.94	0.15	0.36	0.34

8. CONCLUSIONS

Findings from RC Phase VI material characterization study are summarized below:

- Dynamic modulus (*E**) master curves were prepared for the RCIP-VI HMA materials at four different temperatures (14, 32, 50, 68°F). All the E* master curves followed the sigmoidal S-Shape and followed an expected trend of increasing E* values with the decrease of temperature for the same frequency. Comparison of E* values of RCIP-VI with RCIP-IV showed a significant difference in E* values at lower frequencies due to having different HMA mix design. RCIP-VI with RCIP-V had the same HMA mix design and a comparison of E* values between the two phases showed a small difference. The probable cause of the difference in value is construction variability.
- Compaction effort for the two 2.5" overlay lifts was evaluated using Texas Overlay Test. Statistical analysis based on several parameters (air void, peak load, load reduction rate, critical fracture energy, and crack resistance index) showed no significant difference in performance between samples collected from the two lifts. This finding suggests that the compaction effort for both lifts were similar.
- Three Customized OT sample combinations were tested assuming the occurrence of extreme cooling cycles at the beginning, middle, and end of every 12 loading cycles, respectively. Statistical analysis results indicated no significant difference in the

performance of HMA mixture due to different occurrences of extreme cooling cycles.

- Material properties *A* and *n* were found to be 0.8197 and 0.2678 respectively. A comparison with the RCIP-V study revealed a faster crack propagation rate of the RCIP-VI HMA mixture due to extreme cooling cycles.
- Both fracture energy and strain energy captured the extreme cooling effect and this effect decayed with each successive extreme cooling cycle.
- Between RCIP-VI full-scale and laboratory tests, both fracture energy and strain energy increase and decrease percentage were comparable.
- Shift factors were calculated for failure strain and failure cycle by comparing Customized OT and full-scale test results. The values of these shift factors were close to the ones derived from RCIP-V material characterization.

9. REFERENCES

[1] H. Yin and D. Barbagallo, "Development of Full-Scale Reflective Cracking Test at the FAA National Airport Pavement Test Facility," *Transportation Research Record*, vol. 2368, no. 1, pp. 81–91, Jan. 2013, doi: 10.3141/2368-08.

[2] T. Bennert and A. Maher, "Field and Laboratory Evaluation of a Reflective Crack Interlayer in New Jersey," *Transportation Research Record*, vol. 2084, no. 1, pp. 114–123, Jan. 2008, doi: 10.3141/2084-13.

[3] H. Yin, "Full-Scale Test of Thermally Induced Reflective Cracking In Airport Pavements," *Road Materials and Pavement Design*, vol. 16, no. 1, pp. 119–132, Jan. 2015, doi: 10.1080/14680629.2014.982691.

[4] E. V. Dave and W. G. Buttlar, "Thermal Reflective Cracking of Asphalt Concrete Overlays," *International Journal of Pavement Engineering*, vol. 11, no. 6, pp. 477–488, Dec. 2010, doi: 10.1080/10298430903578911.

[5] J. Pais, "The Reflective Cracking in Flexible Pavements," *Romanian Journal of Transport Infrastructure*, vol. 2, no. 1, pp. 63–87, Jul. 2013, doi: 10.1515/rjti-2015-0012.

[6] F. M. Bayomy, F. A. Al-Kandari, and R. M. Smith, "Mechanistically Based Flexible Overlay Design System for Idaho," *Transportation Research Record*, vol. 1543, no. 1, pp. 10–19, Jan. 1996, doi: 10.1177/0361198196154300102.

[7] M. Oshone, E. V. Dave, and J. E. Sias, "Asphalt Mix Fracture Energy Based Reflective Cracking Performance Criteria For Overlay Mix Selection And Design For Pavements In Cold Climates," *Construction and Building Materials*, vol. 211, pp. 1025–1033, Jun. 2019, doi: 10.1016/j.conbuildmat.2019.03.278.

[8] L. M. Pierce, N. C. Jackson, and J. P. Mahoney, "Development and Implementation of A Mechanistic, Empirically Based Overlay Design Procedure For Flexible Pavements," *Transportation Research Record*, no. 1388, 1993, Accessed: Oct. 14, 2019. [Online]. Available: https://trid.trb.org/view/382541.

[9] T. Bennert, "A Rational Approach to The Prediction of Reflective Cracking In Bituminous Overlays For Concrete Pavements," Rutgers University, New Jersey, USA, 2009.

[10] D. Bozkurt and W. G. Buttler, "Three-Dimensional Finite Element Modeling to Evaluate Benefits of Interlayer Stress Absorbing Composite For Reflective Crack Mitigation," in *Proceedings, Federal Aviation Administration Airport Technology Transfer Conference.*, May 2002.

[11] R. Bonaquist, "Refining the Simple Performance Tester for Use in Routine Practice," National Cooperative Highway Research Program Transportation Research Board of The National Academies, Washington D.C., USA, NCHRP Report 614, 2008. doi: 10.17226/14410.

[12] M. Elseifi and R. Bandaru, "Cost Effective Prevention of Reflective Cracking of Composite Pavement," Louisiana Department of Transportation and Development, Louisiana, USA, FHWA/LA.11?478, Sep. 2011. [Online]. Available: https://rosap.ntl.bts.gov/view/dot/23332.

[13] Federal Aviation Administration, "Advisory Circular - Standard Specifications for Construction of Airports," U.S. Department of Transportation, Washington D.C., USA, 150/5370–10H, Dec. 2018.

[14] H. Yin, R. Aponte, R. Rutter, and R. Ji, "Reflective Cracking Indoor Phase-I Comprehensive Report," U.S. Department of Transportation, Washington D.C., USA, FHWA-JPO-XXXX, Dec. 2016.

[15] H. Yin, R. Aponte, R. Rutter, and R. Ji, "Reflective Cracking Indoor Phase-II Comprehensive Report," U.S. Department of Transportation, Washington D.C., USA, FHWA-JPO-XXXX, Apr. 2017.
[16] H. Yin, R. Aponte, R. Rutter, and R. Ji, "Reflective Cracking Indoor Phase-III Comprehensive Report," U.S. Department of Transportation, Washington D.C., USA, FHWA-JPO-XXXX, Feb. 2017.
[17] H. Yin, R. Aponte, R. Rutter, and R. Ji, "Reflective Cracking Indoor Phase-IV Comprehensive Report," U.S. Department of Transportation, Washington D.C., USA, FHWA-JPO-XXXX, Jun. 2017.
[18] H. Yin, R. Aponte, R. Rutter, and R. Ji, "Reflective Cracking Indoor Phase-V Comprehensive Report," U.S. Department of Transportation, Washington D.C., USA, FHWA-JPO-XXXX, Aug. 2017.
[19] H. Yin and T. Mandal, "Reflective Cracking Indoor Phase-IV Comprehensive Report b - Material Characterization," U.S. Department of Transportation, Washington D.C., USA, FHWA-JPO-XXXX, Oct. 2017.
[20] AASHTO T 342-11, "Standard Method of Test for Determining Dynamic Modulus of Hot-Mix Asphalt Concrete Mixtures." American Association of State and Highway Transportation Officials, 2011, Accessed: Feb. 04, 2016. [Online]. Available: http://www.techstreet.com/products/1817547.
[21] G. Garcia and M. Thompson, "HMA Dynamic Modulus Predictive Models– A Review," Illinois Department of Transportation, Illinois, USA, FHWA-ICT-07-005, Jan. 2007. [Online]. Available: https://www.ideals.illinois.edu/bitstream/handle/2142/46009/FHWA-ICT-07-005.pdf?sequence=2&isAllowed=y.
[22] D. W. Christensen and D. A. Anderson, "Interpretation of Dynamic Mechanical Test Data For Paving Grade Asphalt Cements (With Discussion)," in *Journal of the Association of Asphalt Paving Technologists*, 1992, vol. 61, Accessed: Oct. 17, 2019. [Online]. Available: https://trid.trb.org/view/486935.
[23] M. S. Sakhaeifar, Y. Richard Kim, and P. Kabir, "New Predictive Models For The Dynamic Modulus of Hot Mix Asphalt," *Construction and Building Materials*, vol. 76, pp. 221–231, Feb. 2015, doi: 10.1016/j.conbuildmat.2014.11.011.
[24] J. Zhang, A. E. Alvarez, S. I. Lee, A. Torres, and L. F. Walubita, "Comparison of Flow Number, Dynamic Modulus, and Repeated Load Tests For Evaluation of HMA Permanent Deformation," *Construction and Building Materials*, vol. 44, pp. 391–398, Jul. 2013, doi: 10.1016/j.conbuildmat.2013.03.013.
[25] H. Yin and T. Mandal, "Reflective Cracking Indoor Phase-V Comprehensive Report b - Material Characterization," U.S. Department of Transportation, Washington D.C., USA, FHWA-JPO-XXXX, May 2018.
[26] J. G. Speight, "Asphalt Materials Science and Technology," in *Asphalt Materials Science and Technology*, Boston: Butterworth-Heinemann, 2016, pp. 409–435.
[27] M. Pszczola, M. Jaczewski, D. Rys, P. Jaskula, and C. Szydlowski, "Evaluation of Asphalt Mixture Low-Temperature Performance in Bending Beam Creep Test," *Materials (Basel)*, vol. 11, no. 1, Jan. 2018, doi: 10.3390/ma11010100.
[28] F. Zhou and T. Scullion, "Upgraded Overlay Tester and Its Application To Characterize Reflection Cracking Resistance of Asphalt Mixtures," Texas Department of Transportation, Texas, USA, FHWA/TX-04/0-4467-1, Dec. 2003. [Online]. Available: https://static.tti.tamu.edu/tti.tamu.edu/documents/0-4467-1.pdf.

[29] F. Zhou and T. Scullion, "Overlay Tester: A Rapid Performance Related Crack Resistance Test," Texas Department of Transportation, Texas, USA, FHWA/TX-05/0-4467-2, Mar. 2005. [Online]. Available: https://static.tti.tamu.edu/tti.tamu.edu/documents/0-4467-2.pdf.

[30] F. Zhou and T. Scullion, "Overlay Tester: A Simple Performance Test for Thermal Reflective Cracking (With Discussion and Closure)," in *Journal of the Association of Asphalt Paving Technologists*, 2005, vol. 74, Accessed: Oct. 18, 2019. [Online]. Available: https://trid.trb.org/view/776090.

[31] L. F. Walubita, A. N. Faruk, G. Das, H. A. Tanvir, J. Zhang, and T. Scullion, "The Overlay Tester: A Sensitivity Study To Improve Repeatability and Minimize Variability In The Test Results," Texas Department of Transportation, Texas, USA, FHWA/TX-12/0-6607-1, Feb. 2012. [Online]. Available: https://d2dtl5nnlpfr0r.cloudfront.net/tti.tamu.edu/documents/0-6607-1.pdf.

[32] L. F. Walubita, A. N. Faruk, Y. Koohi, R. Luo, T. Scullion, and R. L. Lytton, "The Overlay Tester (OT): Comparison With Other Crack Test Methods And Recommendations For Surrogate Crack Tests," Texas Department of Transportation, Texas, USA, FHWA/TX-13/0-6607-2, Aug. 2013. [Online]. Available: https://static.tti.tamu.edu/tti.tamu.edu/documents/0-6607-2.pdf.

[33] W. Ma, "Proposed Improvements to Overlay Test for Determining Cracking Resistance of Asphalt Mixtures," Thesis, Auburn University, Alabama, USA, 2014.

[34] Tex-248-F, "Test Procedure for OVERLAY TEST." Materials and Tests Division, Texas Department of Transportation, Jul. 2019, [Online]. Available: ftp://ftp.dot.state.tx.us/pub/txdot-info/cst/TMS/200-F_series/pdfs/bit248.pdf.

[35] ASTM D 4867, "Standard Test Method for Effect of Moisture on Asphalt Concrete Paving Mixtures." American Society for Testing and Materials, Nov. 2014.

[36] P. Paris and F. Erdogan, "A Critical Analysis of Crack Propagation Laws," *Journal of Basic Engineering*, vol. 85, no. 4, pp. 528–533, Dec. 1963, doi: 10.1115/1.3656900.

[37] R. A. Schapery, "A Theory of Crack Initiation And Growth In Viscoelastic Media," *International Journal of Fracture*, vol. 11, no. 1, pp. 141–159, Feb. 1975, doi: 10.1007/BF00034721.

[38] R. A. Schapery, "A Method For Predicting Crack Growth In Nonhomogeneous Viscoelastic Media," *International Journal of Fracture*, vol. 14, no. 3, pp. 293–309, Jun. 1978, doi: 10.1007/BF00034690.

[39] R. A. Schapery, "Correspondence Principles And A Generalized J Integral For Large Deformation And Fracture Analysis Of Viscoelastic Media," *International Journal of Fracture*, vol. 25, no. 3, pp. 195–223, Jul. 1984, doi: 10.1007/BF01140837.

[40] E. B. Owusu-Antwi, L. Khazanovich, and L. Titus-Glover, "Mechanistic-Based Model for Predicting Reflective Cracking in Asphalt Concrete–Overlaid Pavements," *Transportation Research Record*, vol. 1629, no. 1, pp. 234–241, Jan. 1998, doi: 10.3141/1629-26.

[41] A.-Q. E. Leonard, "Development of an Overlay Design Model for Reflective Cracking with and without Steel Reinforcing Nettings," *Asphalt Paving Technology*, vol. 72, p. 41, 2003.

[42] F. Zhou, S. Hu, X. Hu, and T. Scullion, "Mechanistic-Empirical Asphalt Overlay Thickness Design and Analysis System.," Texas Transportation Institute, 2009.

[43] Ceylan Halil, Gopalakrishnan Kasthurirangan, and Lytton Robert L., "Neural Networks Modeling of Stress Growth in Asphalt Overlays due to Load and Thermal Effects during Reflection Cracking," *Journal of Materials in Civil Engineering*, vol. 23, no. 3, pp. 221–229, Mar. 2011, doi: 10.1061/(ASCE)MT.1943-5533.0000153.

[44] B. Sheng and W.-C. V. Ping, “Evaluation Of Florida Asphalt Mixes For Crack Resistance Properties Using The Laboratory Overlay Test Procedure,” Florida Department of Transportation, Florida, FDOT BDV30 TWO 977-06, 2016.
[45] B. Birgisson, J. Wang, R. Roque, and B. Sangpetngam, “Numerical Implementation of a Strain Energy-based Fracture Model for HMA Materials,” *Road Materials and Pavement Design*, vol. 8, no. 1, pp. 7–45, Jan. 2007, doi: 10.1080/14680629.2007.9690065.
[46] S. Tang, “Evaluate The Fracture And Fatigue Resistances of Hot Mix Asphalt Containing High Percentage Reclaimed Asphalt Pavement (RAP) Materials At Low And Intermediate Temperatures,” Iowa State University, Iowa, 2014.
[47] H. Yin, R. Kola, R. Aponte, R. Rutter, and R. Ji, “Reflective Cracking Indoor Phase-VI Comprehensive Report,” U.S. Department of Transportation, Washington D.C., USA, FHWA-JPO-XXXX, Sep. 2019.

APPENDIX – A: DYNAMIC MODULUS SPECIMEN VOLUMETRICS AND GEOMETRY

Table A.1: RCIP-VI Dynamic Modulus Test Specimen Volumetrics

Sample ID.	GMM	Dry Mass in Air (grams) [A]	Mass in SSD Condition (grams) [B]	Mass Submerged in Water (grams) [C]	Bulk Specific Gravity	Percent Water Absorbed (%)	Air Voids
Inside 1	2.663	2951.3	2954.1	1767.3	2.487	0.24	6.6
Inside 2	2.663	2985.3	2987.9	1784.9	2.482	0.22	6.8
Inside 3	2.663	2948.4	2952.8	1762.5	2.477	0.37	7.0

Table A.2: RCIP-VI Dynamic Modulus Test Specimen Measurements

Dimension	Sample ID.		
	Inside 1	**Inside 2**	**Inside 3**
Diameter 01 (mm)	100.6	100.6	100.6
Diameter 02 (mm)	100.6	100.6	100.6
Height 01 (mm)	150.3	150.5	150.4
Height 02 (mm)	150.4	150.4	150.5
Height 03 (mm)	150.2	150.6	150.7

APPENDIX – B: TEXAS OVERLAY SPECIMEN VOLUMETRICS AND GEOMETRY

Table B.1: RCIP-VI Texas Overlay Test Specimen Volumetrics

Core No.	Lift	GMM	Dry Mass in Air (grams) [A]	Mass in SSD Condition (grams) [B]	Mass Submerged in Water (grams) [C]	Bulk Specific Gravity	Percent Water Absorbed (%)	Air Voids (%)
N3	Top	2.675	1007.8	1011.0	605.5	2.485	0.79	7.1
	Bottom	2.675	1017.5	1020.9	608.0	2.464	0.82	7.9
N7	Top	2.675	1015.8	1018.1	609.2	2.484	0.56	7.1
N16	Top	2.675	1043.7	1044.5	631.8	2.529	0.19	5.5
	Bottom	2.675	1017.8	1021.1	612.3	2.490	0.81	6.9
N4	Bottom	2.675	1006.5	1008.0	604.1	2.492	0.37	6.8

Table B.2: RCIP-VI Texas Overlay Test Specimen Measurements

SAMPLE	LIFT	THICKNESS (mm)	WIDTH (mm)
N3	Top	38.24	75.68
	Bottom	37.32	76.05
N7	Top	38.32	75.73
N16	Top	38.55	75.65
	Bottom	38.19	76.11
N4	Bottom	37.98	75.67

APPENDIX – C: TEXAS OVERLAY TEST – LOAD VS CYCLE PLOTS

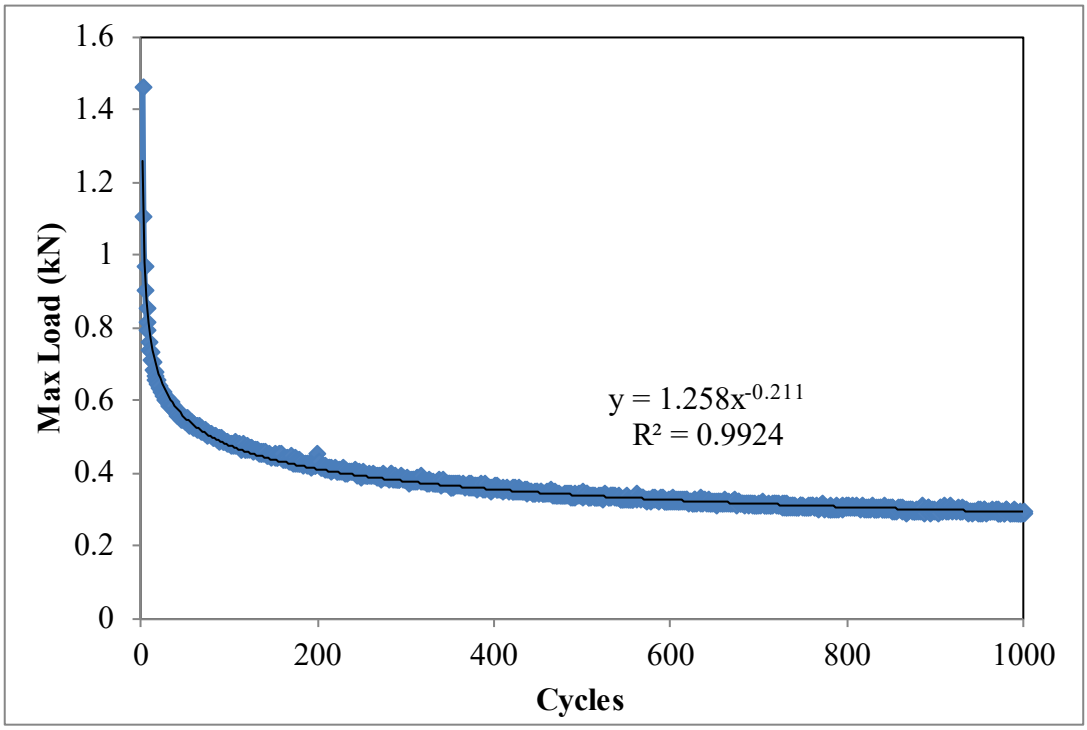

Figure C.1: Load vs Cycle Plot (Sample N3B)

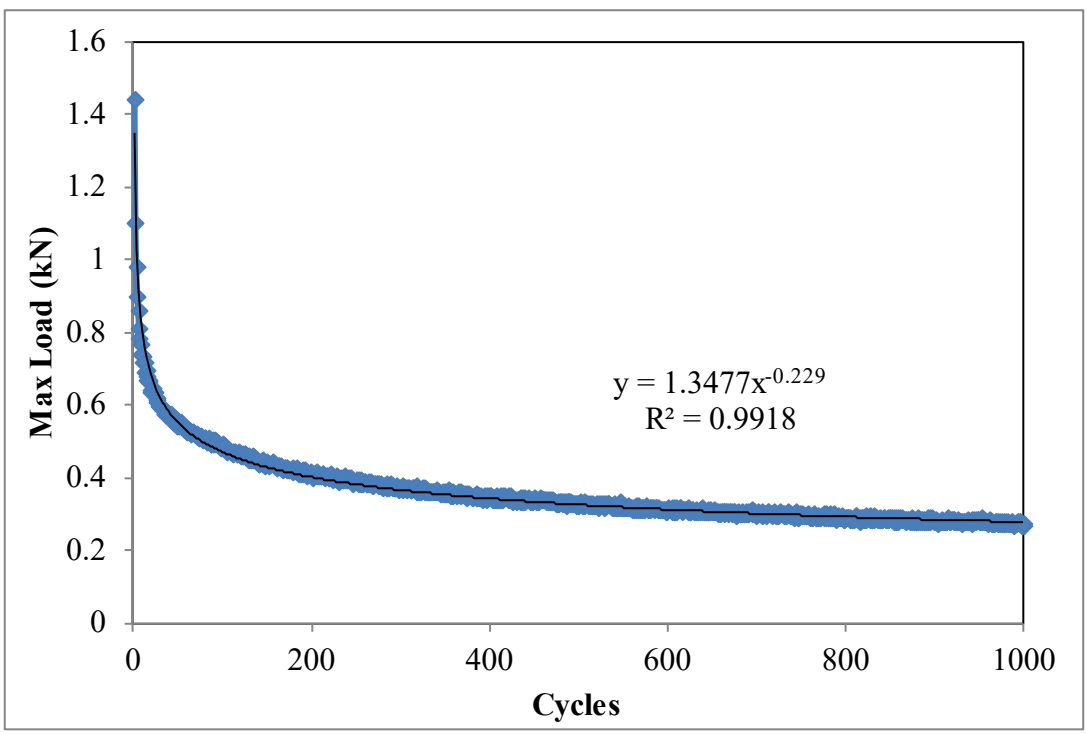

Figure C.2: Load vs Cycle Plot (Sample N4B)

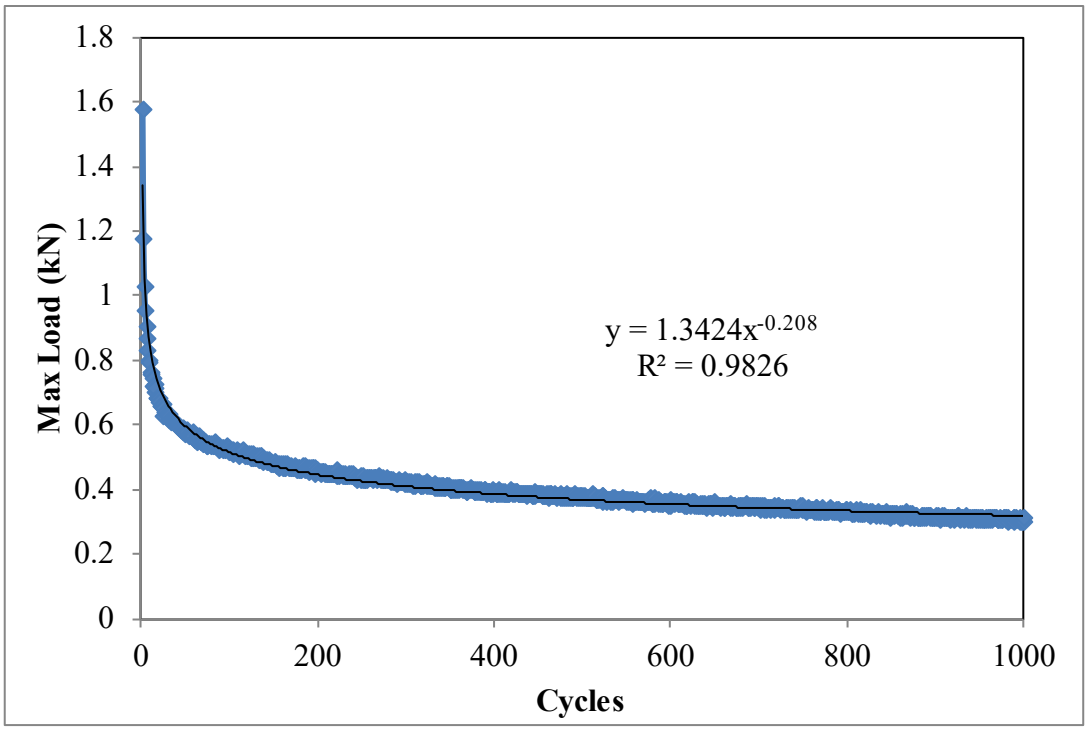

Figure C.3: Load vs Cycle Plot (Sample N16B)

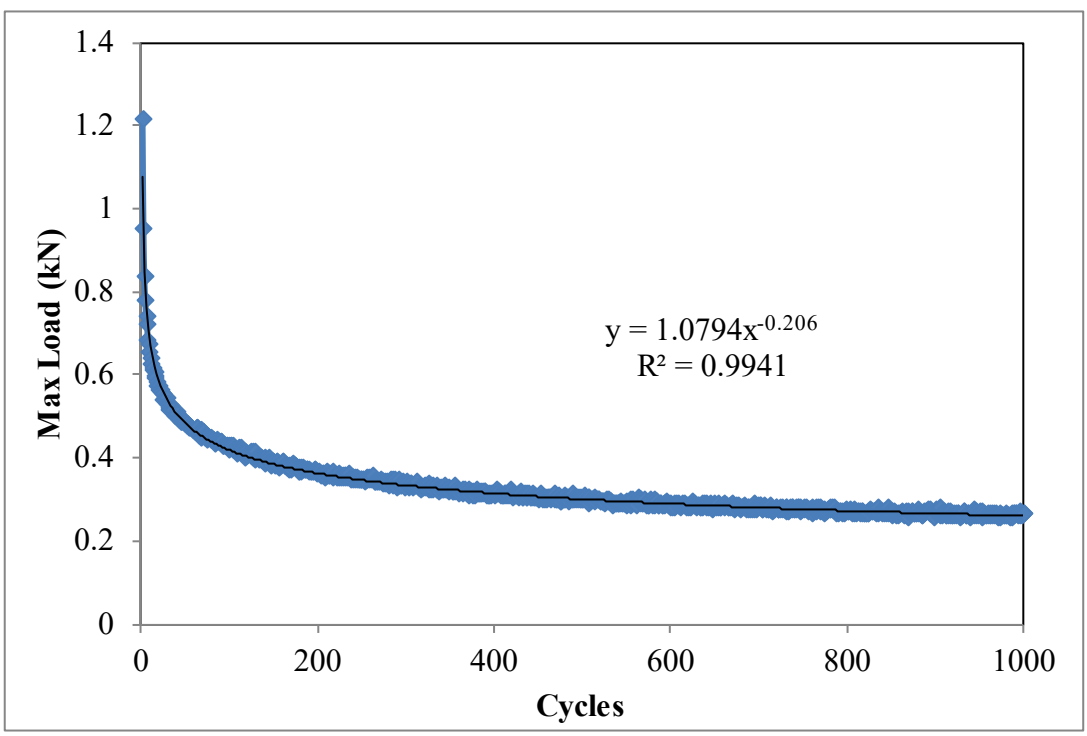

Figure C.4: Load vs Cycle Plot (Sample N3T)

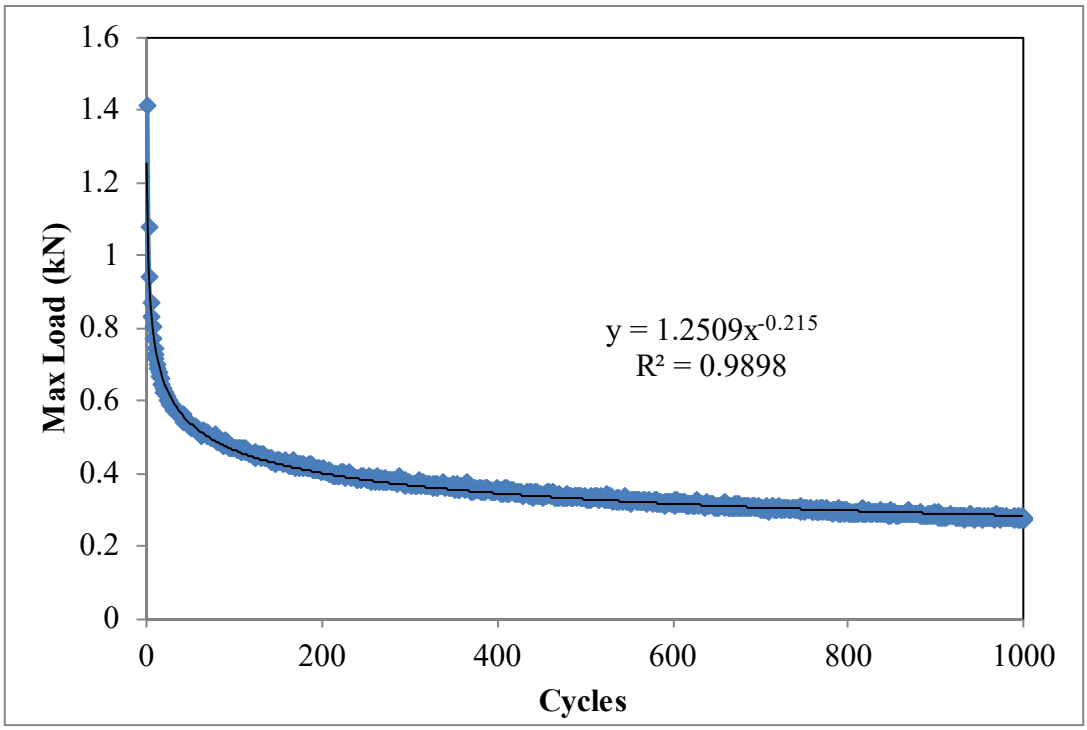

Figure C.5: Load vs Cycle Plot (Sample N7T)

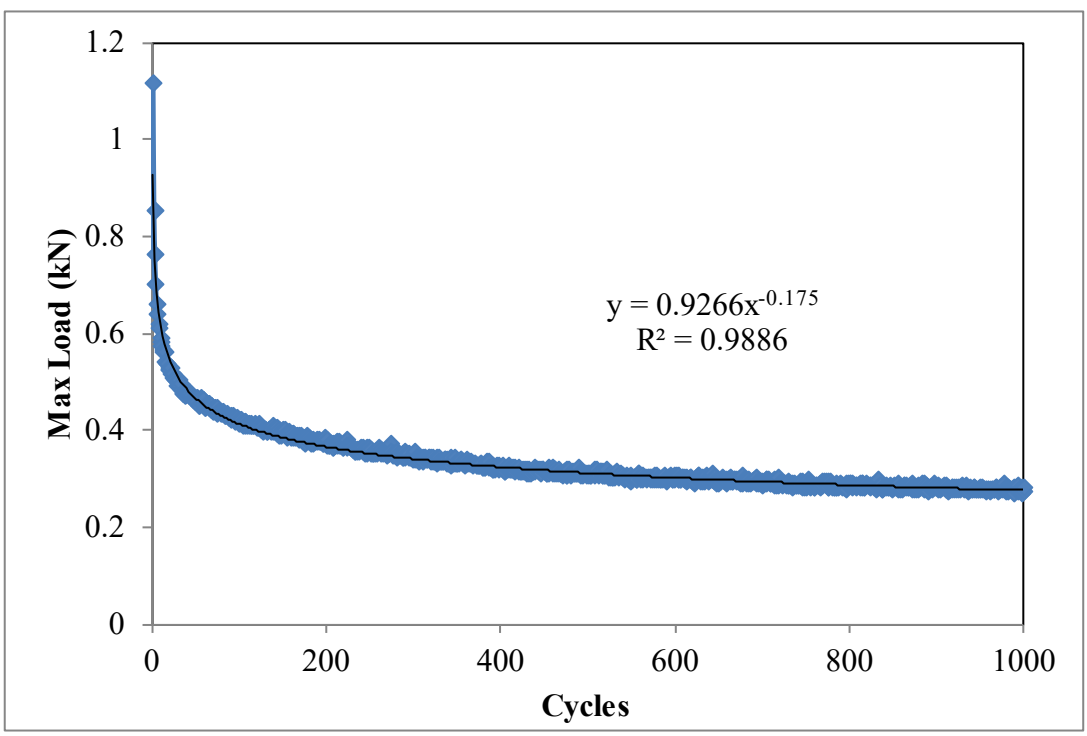

Figure C.6: Load vs Cycle Plot (Sample N16T)

APPENDIX – D: TEXAS OVERLAY TEST – SAMPLE PICTURES

(a) Front Side

(b) Back Side

(c) Top View

Figure D.1: Picture of Sample N3B

(a) Front Side

(b) Back Side

(c) Top View

Figure D.2: Picture of Sample N4B

(a) Front Side

(b) Back Side

(c) Top View

Figure D.3: Picture of Sample N16B

(a) Front Side

(b) Back Side

(c) Top View

Figure D.4: Picture of Sample N3T

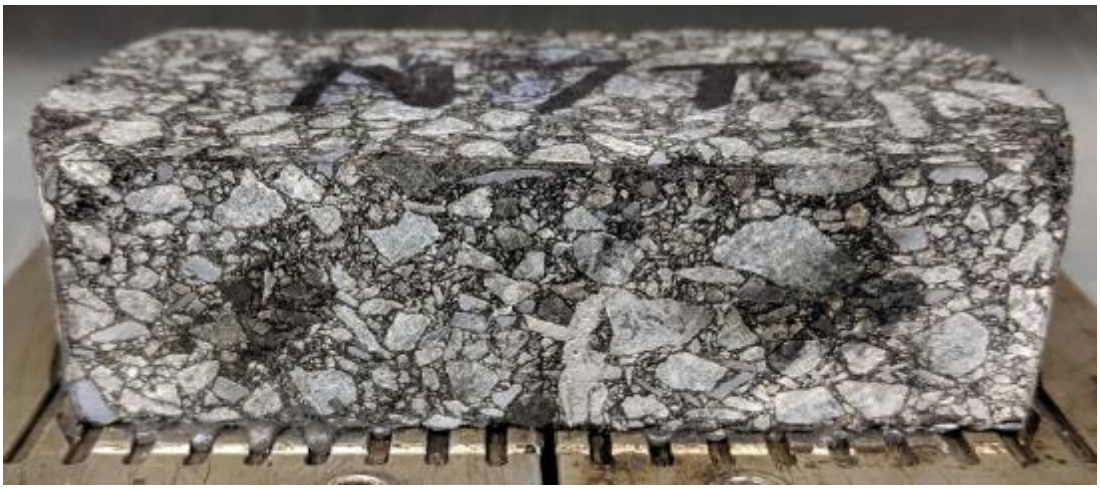

(a) Front Side

(b) Back Side

(c) Top View

Figure D.5: Picture of Sample N7T

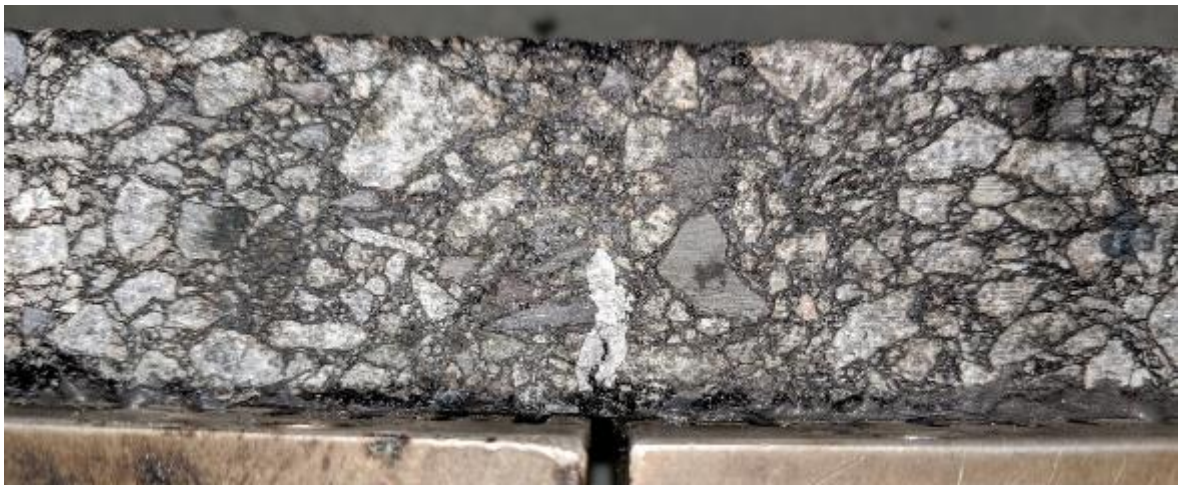

(a) Front Side

(b) Back Side

(c) Top View

Figure D.6: Picture of Sample N16T

APPENDIX – E: CUSTOMIZED OT SPECIMEN VOLUMETRICS AND GEOMETRY

Table E.1: RCIP-VI Customized Overlay Test Specimen Volumetrics

Core No.	GMM	Dry Mass in Air (grams) [A]	Mass in SSD Condition (grams) [B]	Mass Submerged in Water (grams) [C]	Bulk Specific Gravity	Percent Water Absorbed (%)	Air Voids (%)
S1	2.675	998.4	1006.8	601.4	2.463	2.07	7.9
S2	2.675	1039.4	1041.0	627.6	2.514	0.39	6.0
S3	2.675	1018.3	1022.4	614.6	2.497	1.01	6.7
S7	2.675	1007.8	1012.4	607.7	2.490	1.14	6.9
S9	2.675	1001.8	1004.7	599.8	2.474	0.72	7.5
S10	2.675	1017.0	1020.3	606.4	2.457	0.80	8.1
S11	2.675	1024.6	1028.0	618.6	2.503	0.83	6.4
S14	2.675	1038.8	1041.3	627.2	2.509	0.60	6.2
N8	2.675	1016.5	1021.6	612.9	2.487	1.25	7.0
N9	2.675	1014.1	1017.2	610.6	2.494	0.76	6.8
N10	2.675	1039.8	1042.8	630.2	2.520	0.73	5.8
N12	2.675	1019.0	1023.6	611.9	2.475	1.12	7.5
N14	2.675	1041.4	1043.8	628.6	2.508	0.58	6.2
N17	2.675	1007.5	1013.8	604.4	2.461	1.54	8.0
N18	2.675	1041.5	1044.3	631.3	2.522	0.68	5.7

Table E.2: RCIP-VI Customized Overlay Test Specimen Thickness

Sample	Thickness-1 (mm)	Thickness-2 (mm)	Thickness-3 (mm)	Thickness-4 (mm)	Average Thickness
S1	38.15	38.35	37.79	38.30	38.15
S2	38.68	38.74	38.31	38.63	38.59
S3	38.67	38.22	38.33	37.77	38.25
S7	37.83	38.24	38.30	37.34	37.93
S9	37.73	37.66	38.34	38.34	37.97
S10	39.49	38.78	37.65	37.65	38.49
S11	38.01	38.42	38.05	38.55	38.26

S14	37.87	39.16	38.24	38.24	38.51
N8	38.20	38.26	38.31	38.17	38.24
N9	38.26	37.65	38.39	38.22	38.13
N10	38.66	38.62	38.12	38.19	38.40
N12	38.00	38.81	38.15	38.15	38.46
N14	39.31	38.41	38.54	38.54	38.53
N17	38.81	38.31	38.22	38.22	38.40
N18	38.23	38.85	38.09	38.09	38.53

Table E.3: RCIP-VI Customized Overlay Test Specimen Width

Sample	**Width-1 (mm)**	**Width-2 (mm)**	**Average Width**
S1	75.59	75.87	75.73
S2	76.55	76.34	76.45
S3	76.46	76.17	76.32
S7	76.15	76.77	76.46
S9	75.94	76.30	76.30
S10	76.33	75.77	75.77
S11	75.51	75.98	75.75
S14	76.30	76.49	76.49
N8	75.84	76.29	76.07
N9	75.80	76.06	75.93
N10	76.01	76.15	76.08
N12	75.90	75.90	75.90
N14	76.03	75.90	75.90
N17	75.68	75.88	75.88
N18	76.19	76.13	76.13

APPENDIX – F: CUSTOMIZED OT SPECIMEN NORMALIZED LOAD AND NLC PLOTS

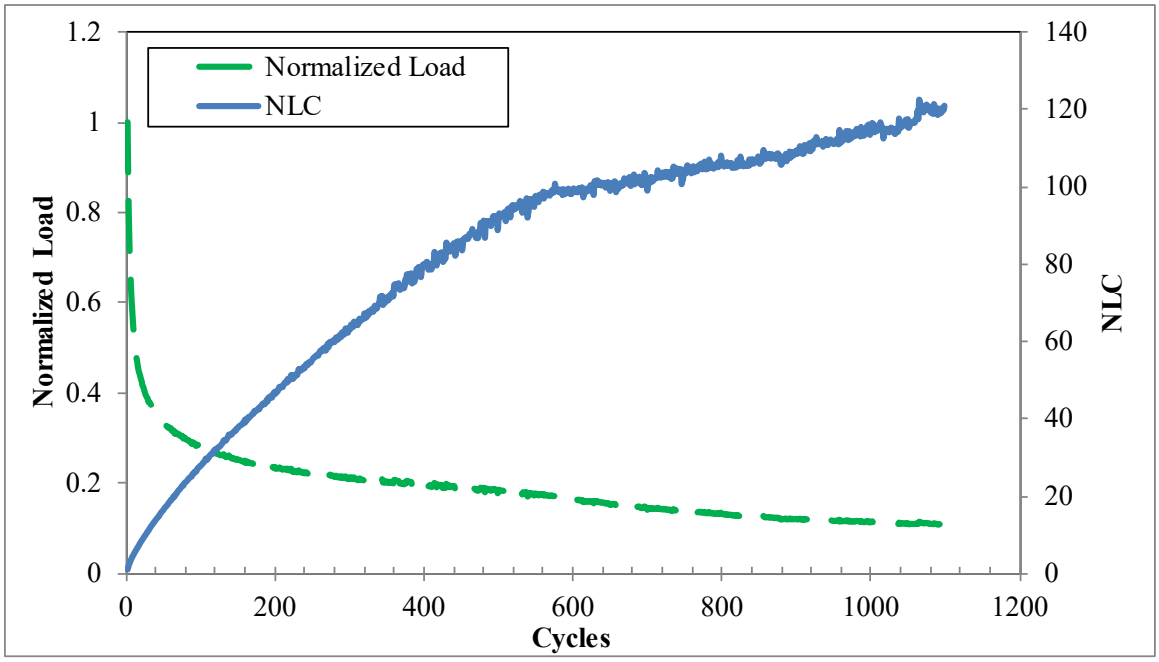

Figure F.1: Sample S1 Normalized Load and NLC Plot

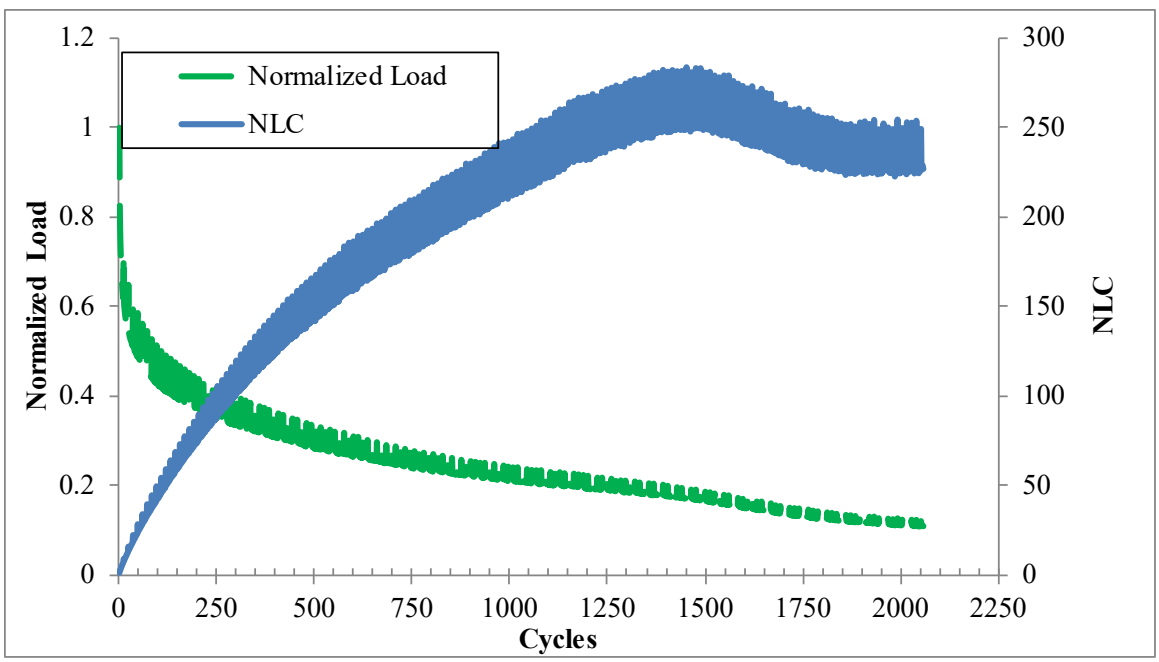

Figure F.2: Sample S2 Normalized Load and NLC Plot

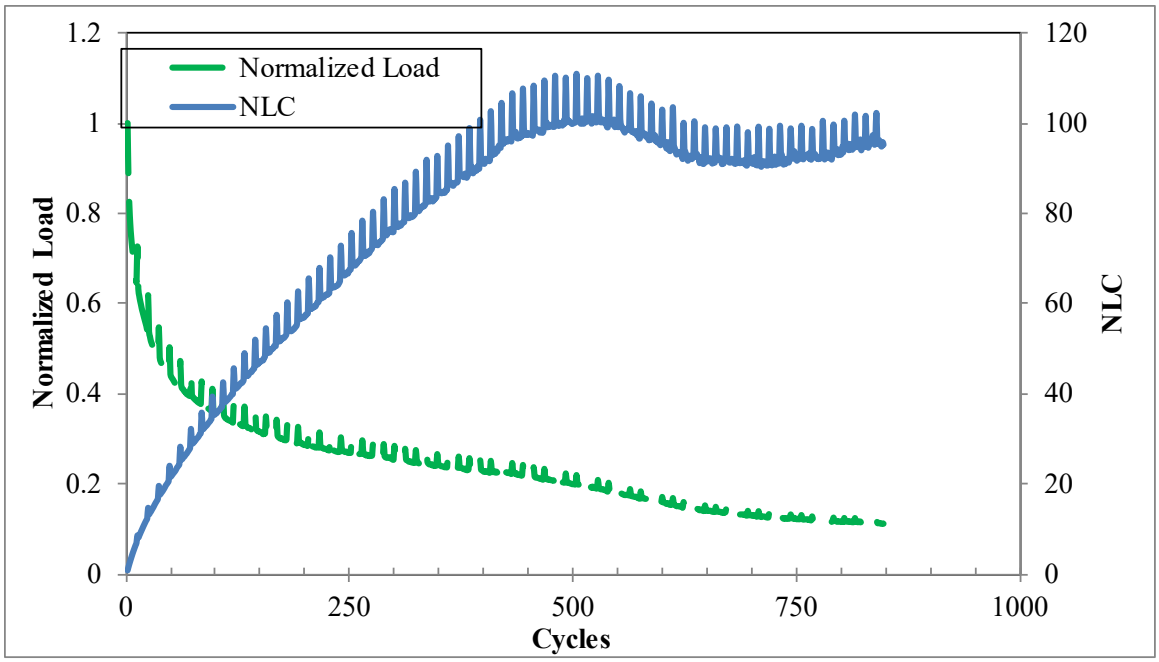

Figure F.3: Sample S3 Normalized Load and NLC Plot

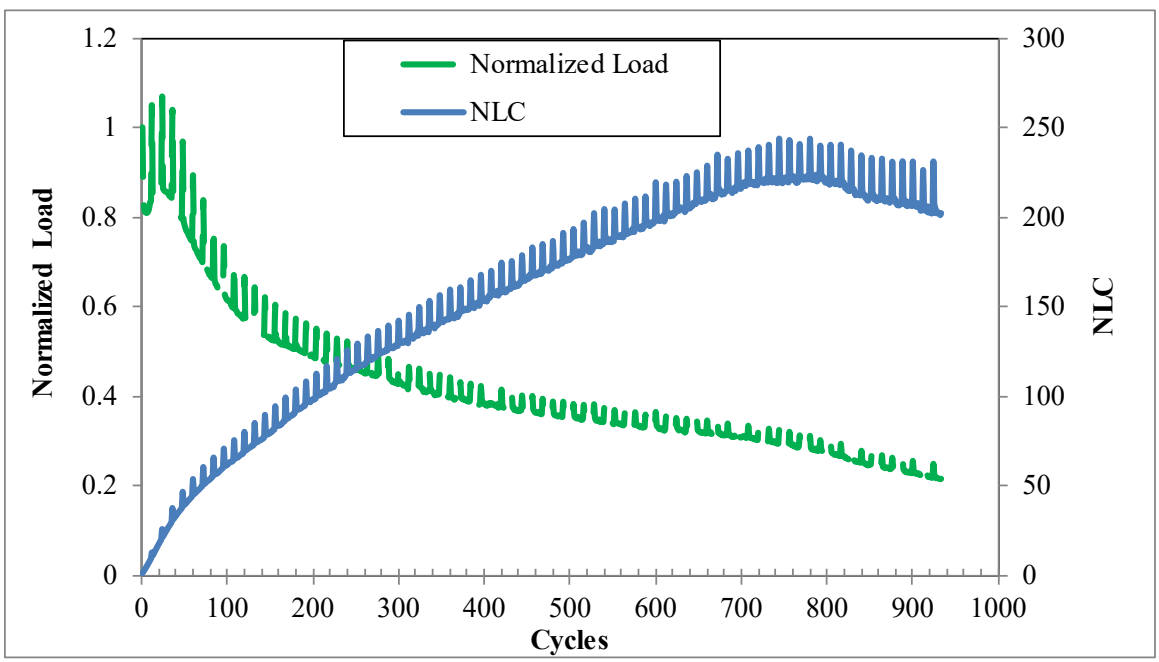

Figure F.4: Sample S7 Normalized Load and NLC Plot

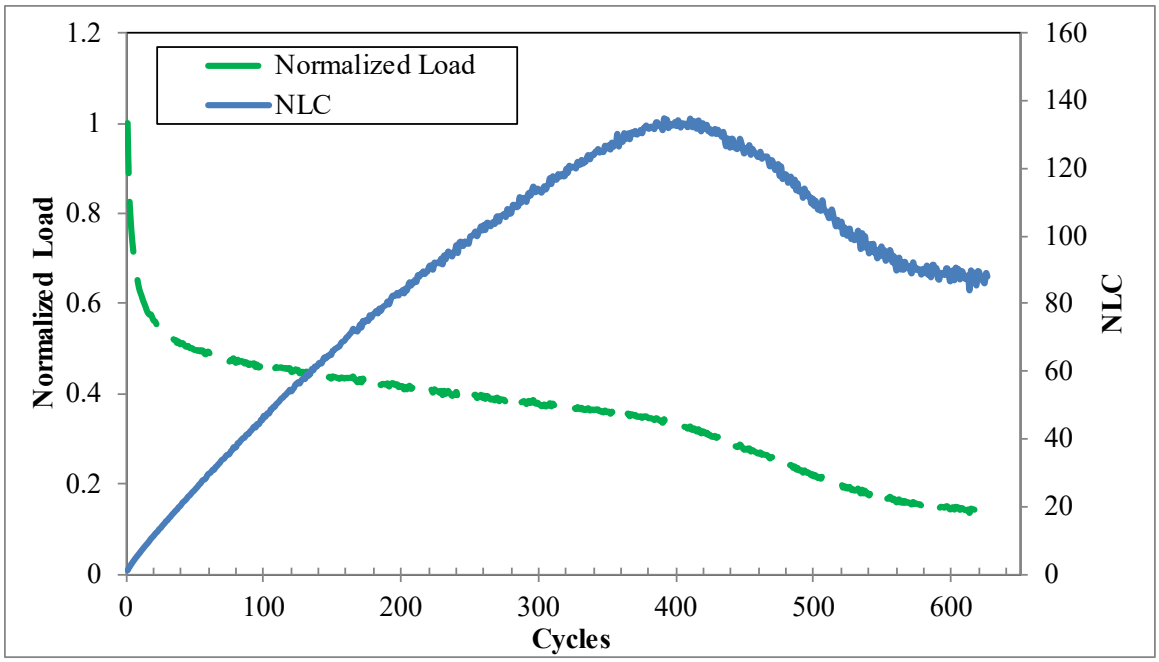

Figure F.5: Sample S9 Normalized Load and NLC Plot

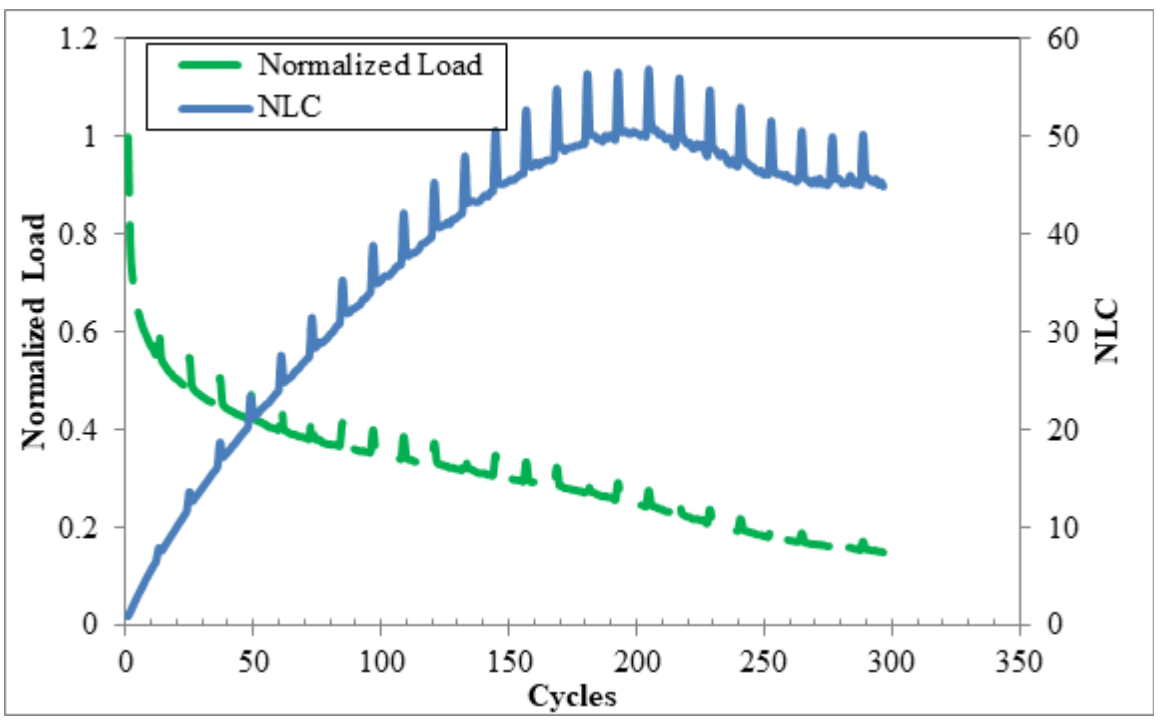

Figure F.6: Sample S10 Normalized Load and NLC Plot

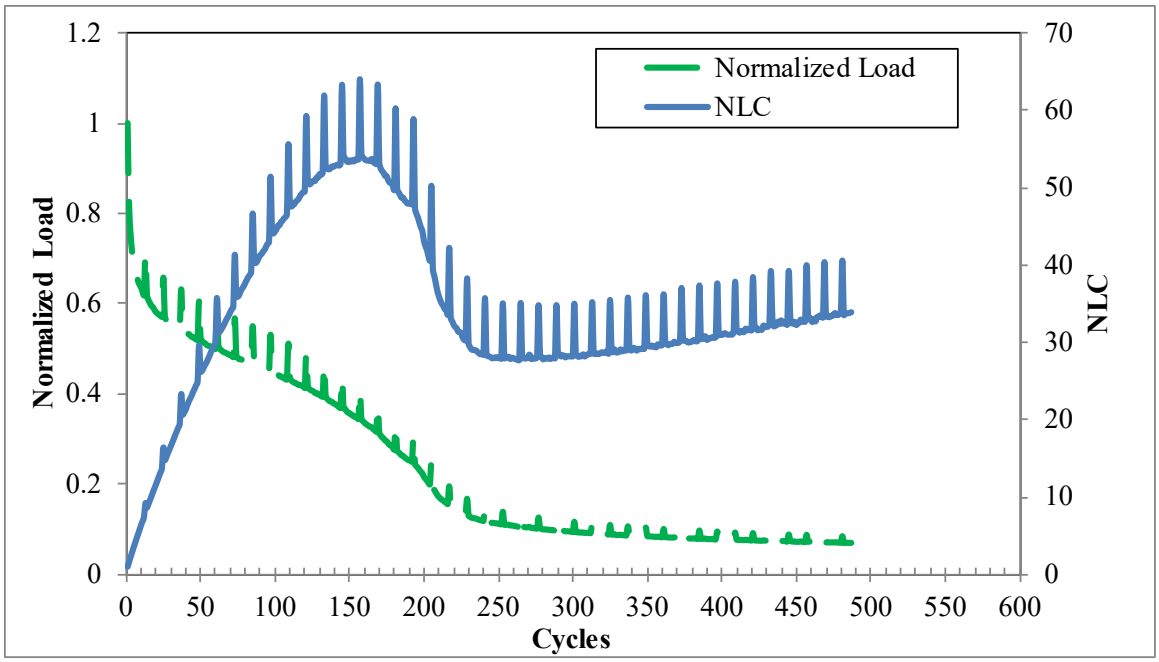

Figure F.7: Sample S11 Normalized Load and NLC Plot

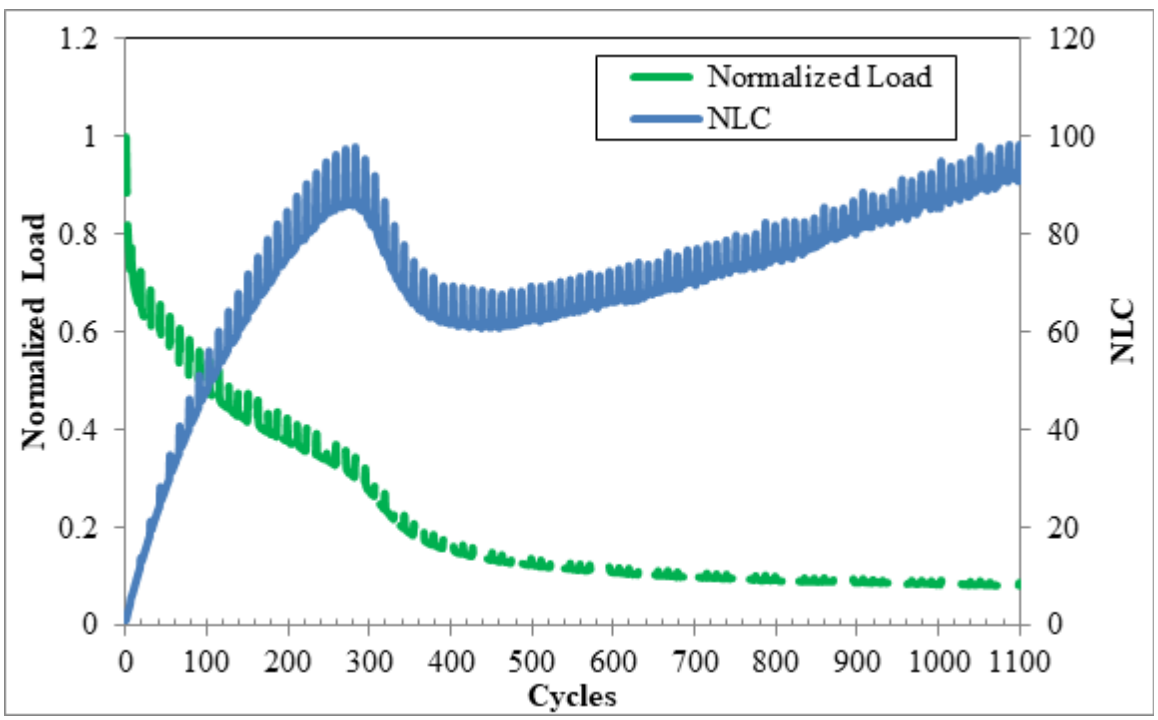

Figure F.8: Sample S14 Normalized Load and NLC Plot

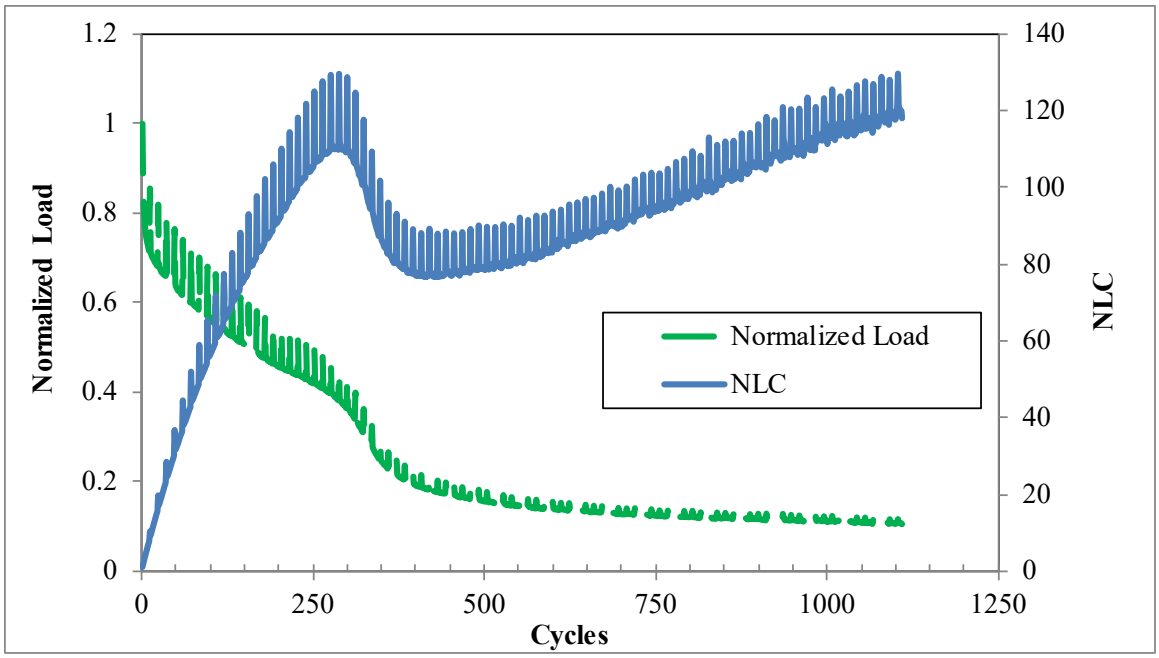

Figure F.9: Sample N8 Normalized Load and NLC Plot

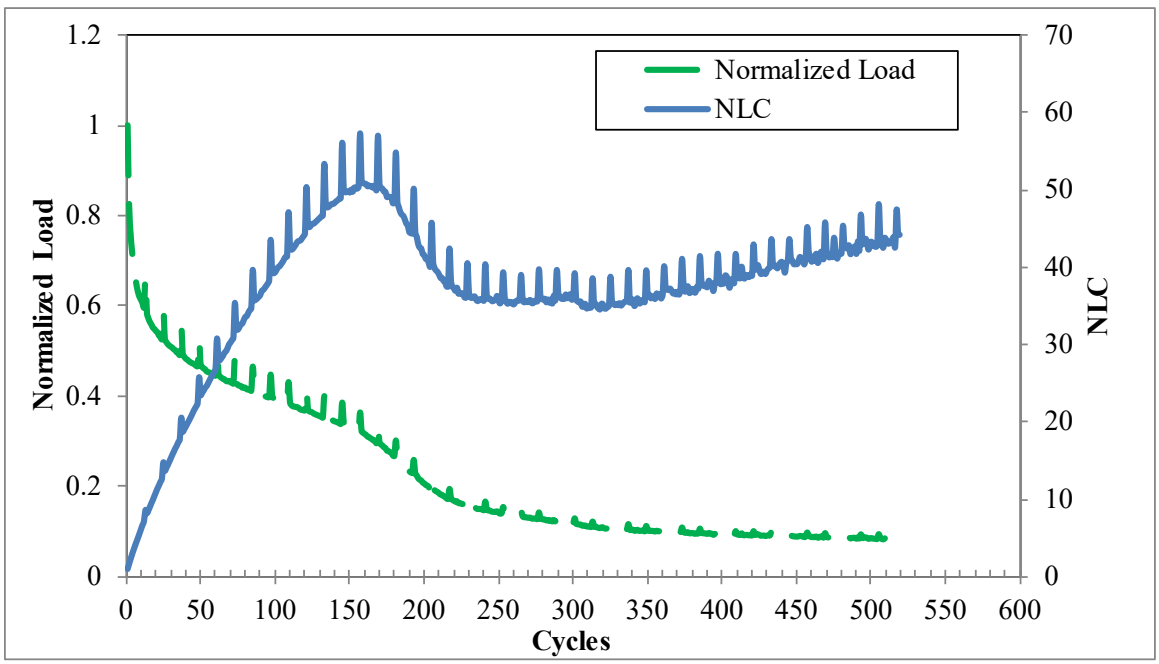

Figure F.10: Sample N9 Normalized Load and NLC Plot

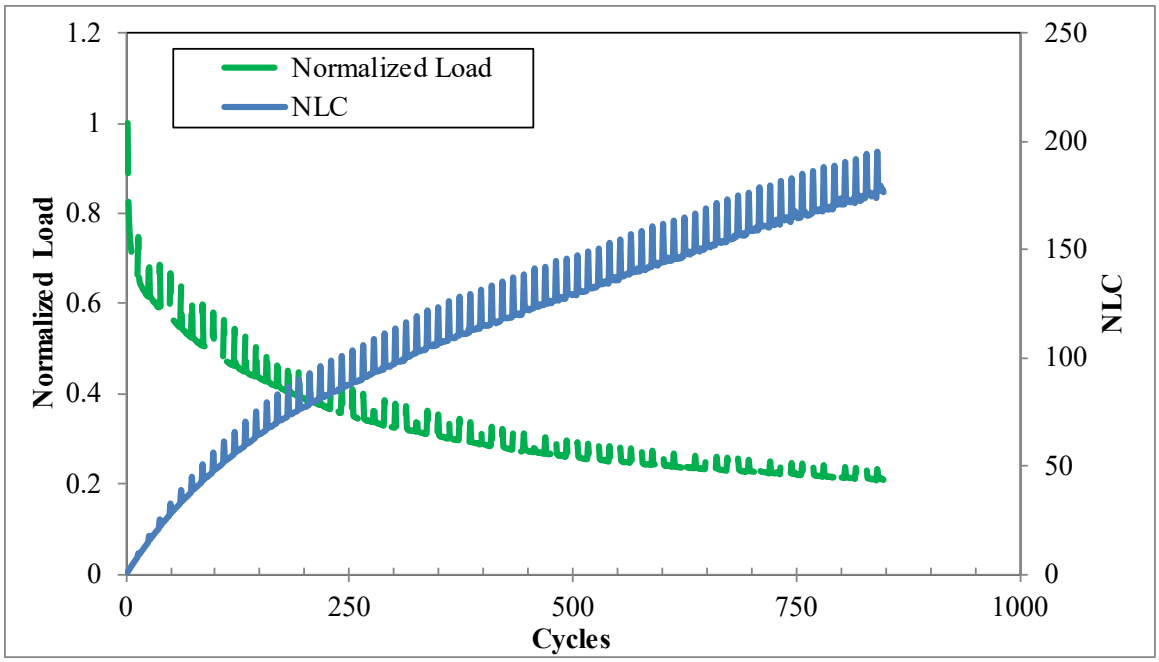

Figure F.11: Sample N10 Normalized Load and NLC Plot

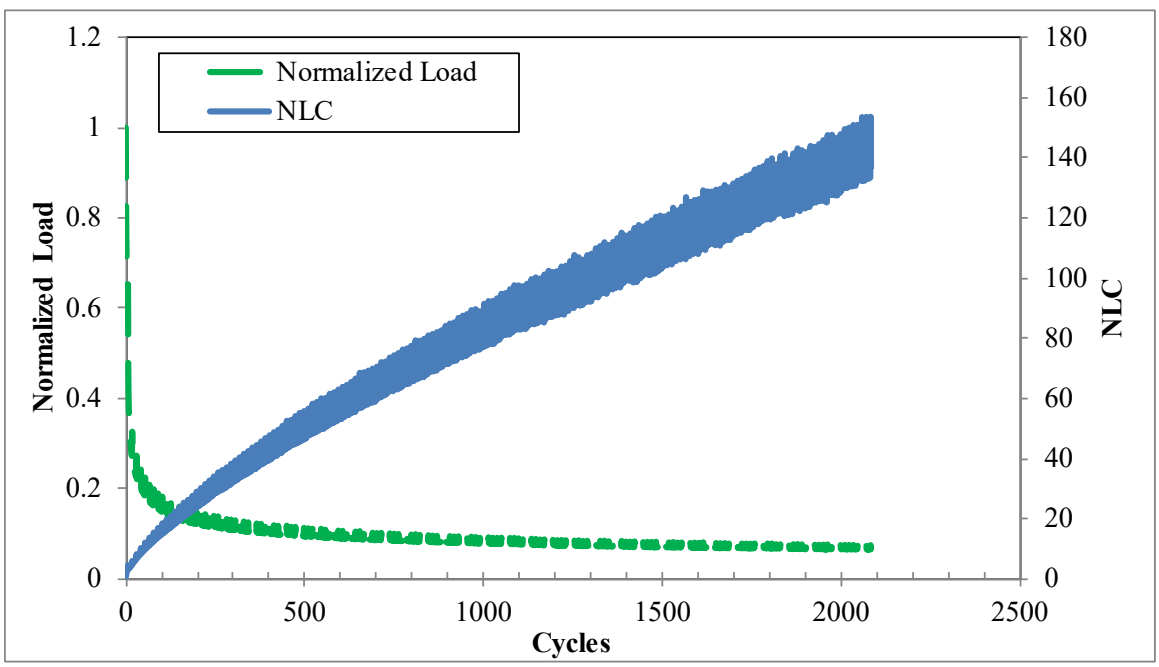

Figure F.12: Sample N12 Normalized Load and NLC Plot

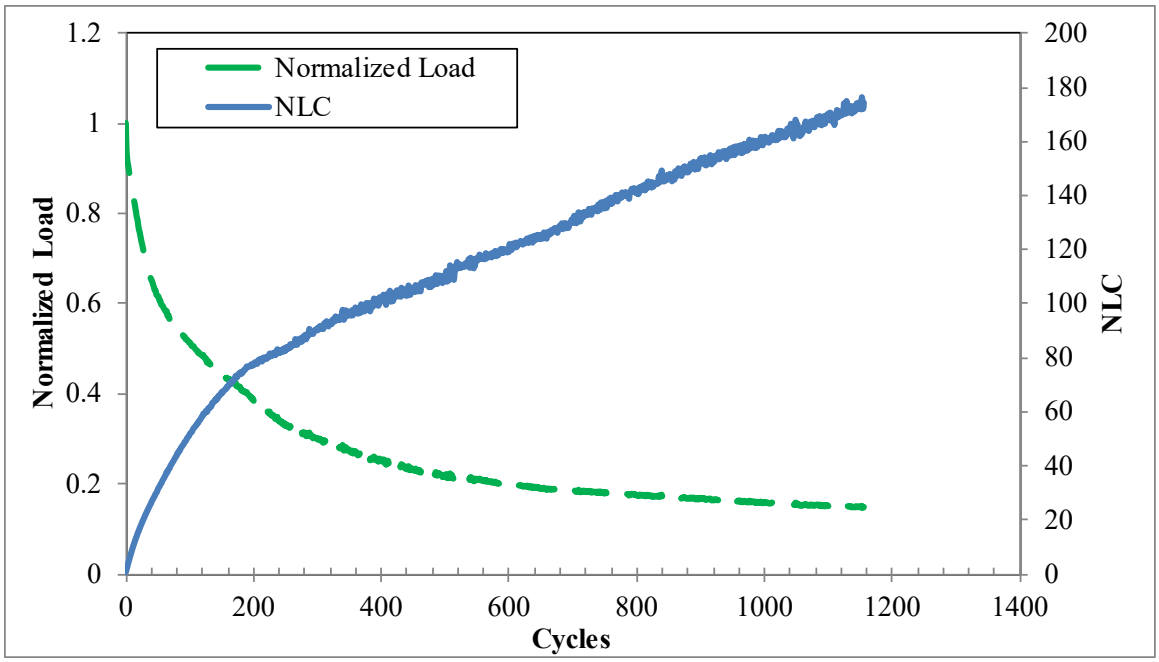

Figure F.13: Sample N14 Normalized Load and NLC Plot

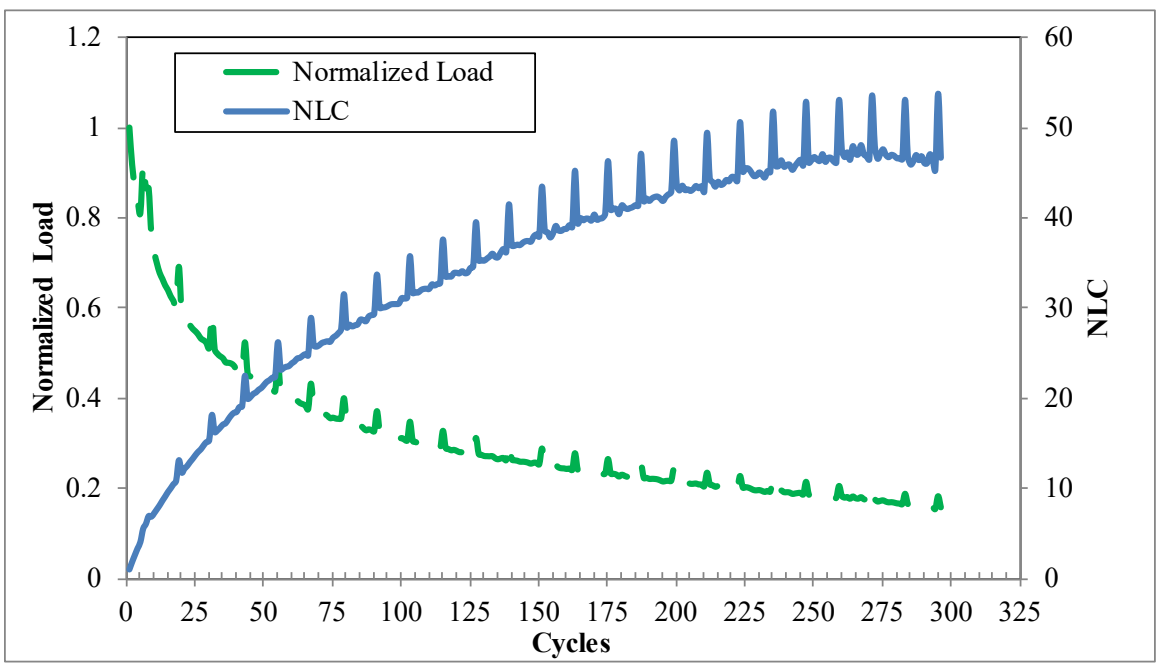

Figure F.14: Sample N17 Normalized Load and NLC Plot

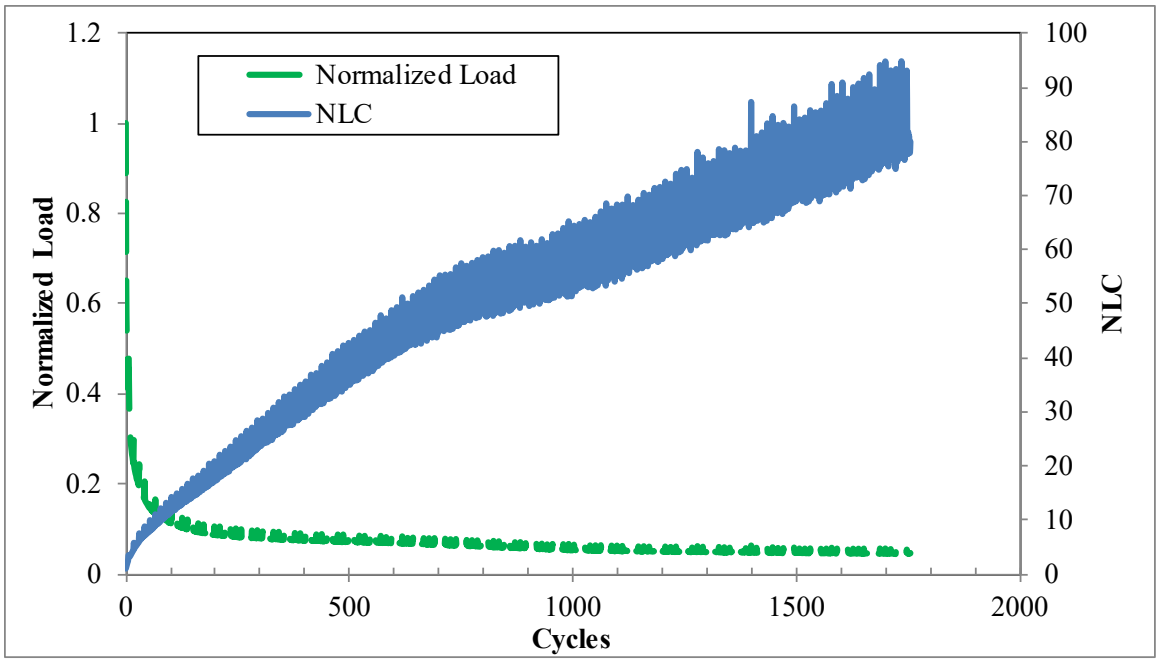

Figure F.15: Sample N18 Normalized Load and NLC Plot

APPENDIX – G: CUSTOMIZED OT SPECIMEN "LOAD VS CYCLE PLOTS"

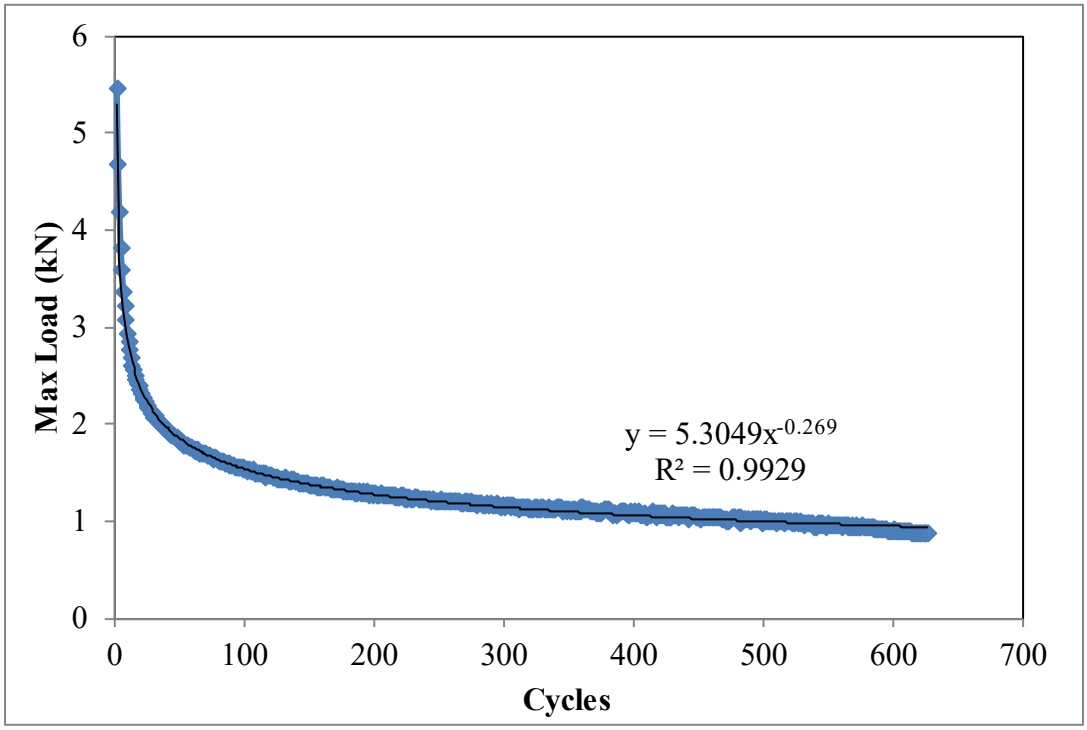

Figure G.1: Sample S1 Load vs Cycle Plot

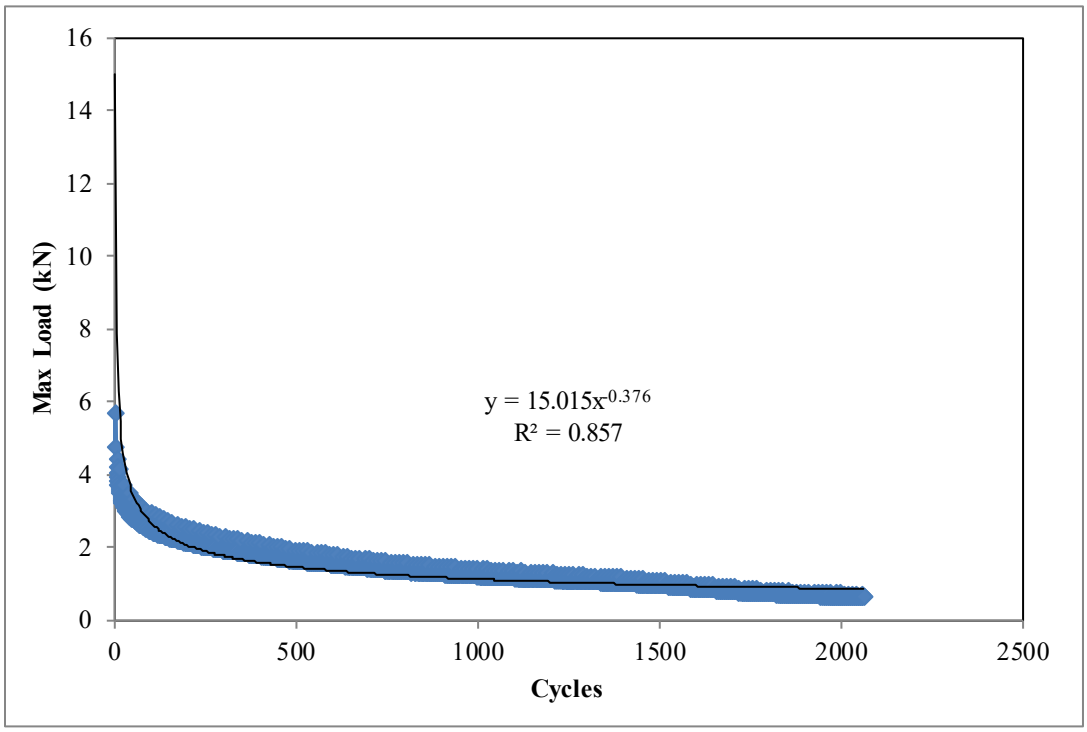

Figure G.2: Sample S2 Load vs Cycle Plot

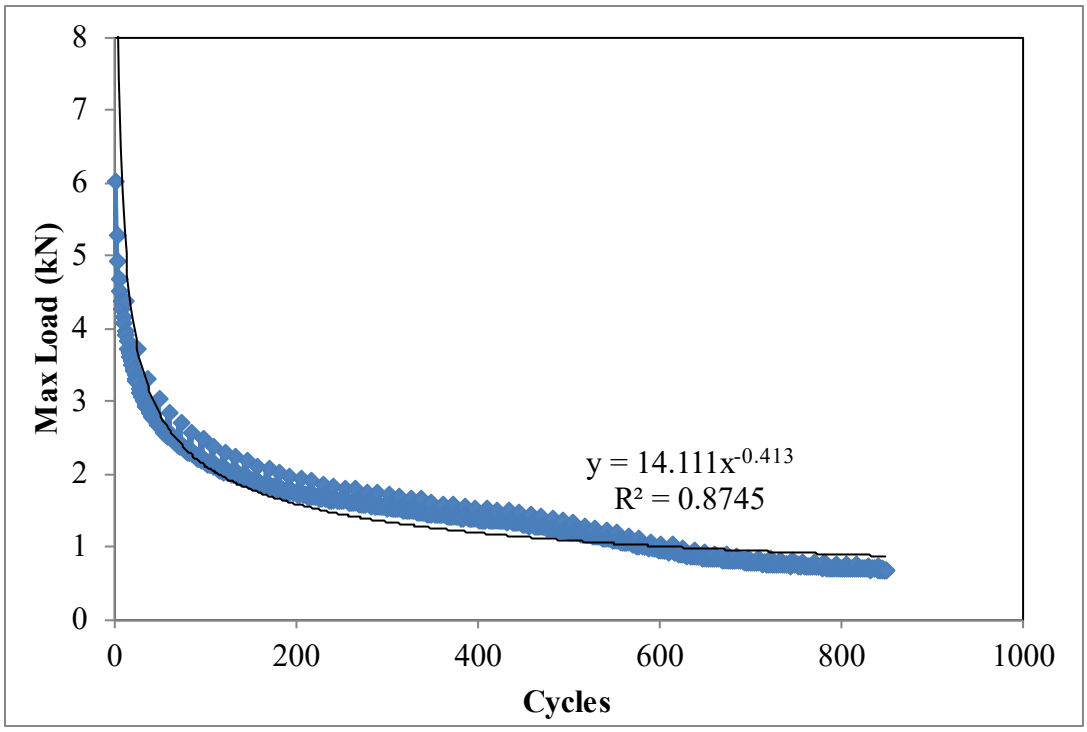

Figure G.3: Sample S3 Load vs Cycle Plot

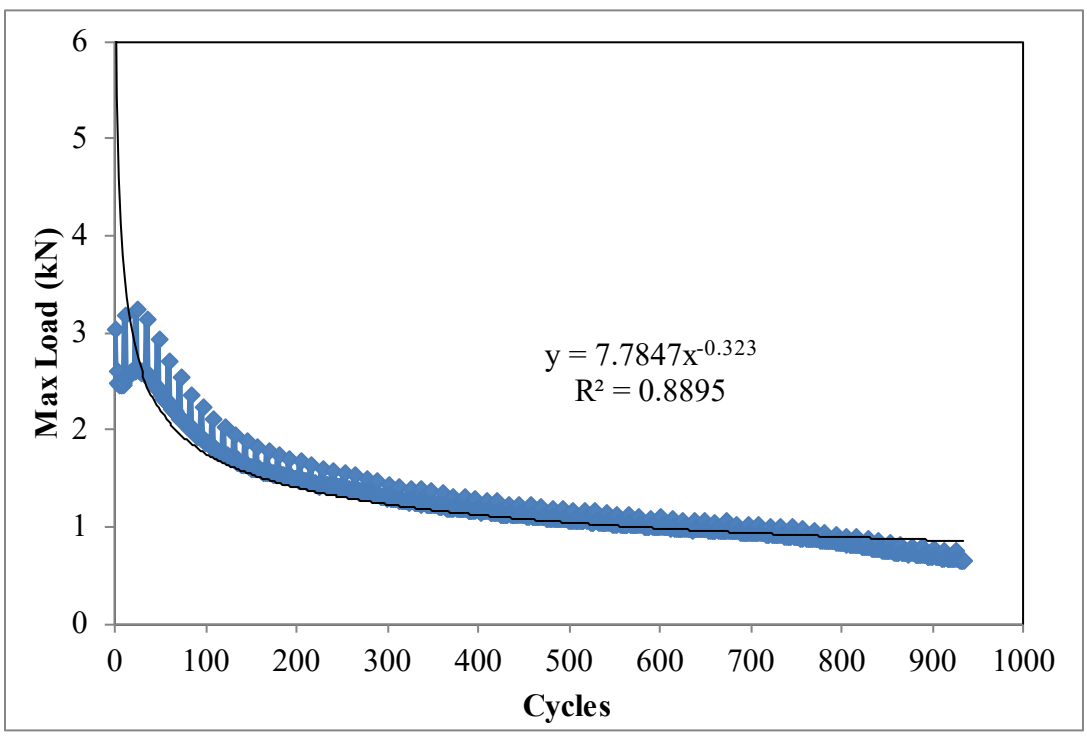

Figure G.4: Sample S7 Load vs Cycle Plot

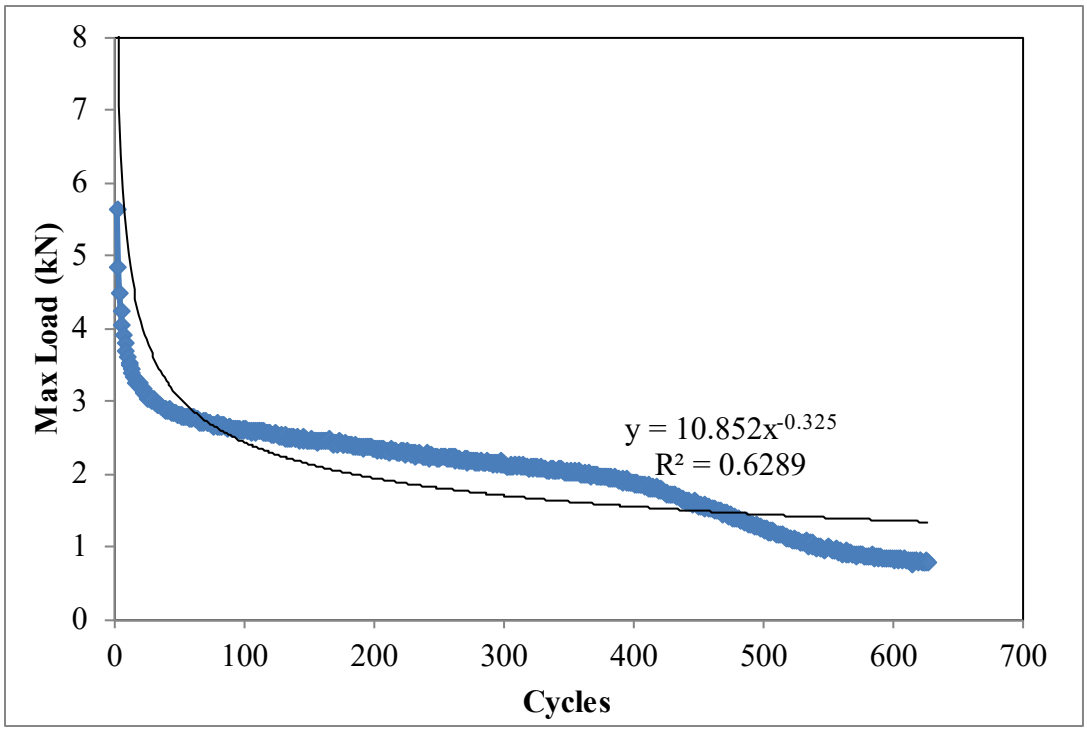

Figure G.5: Sample S9 Load vs Cycle Plot

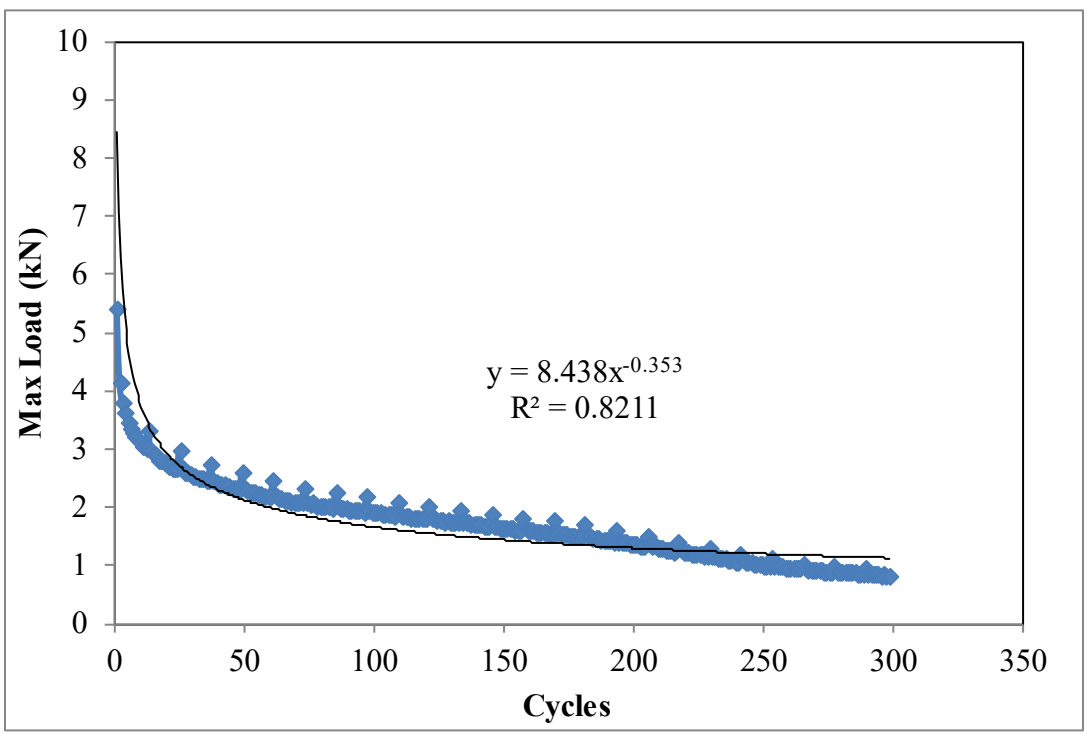

Figure G.6: Sample S10 Load vs Cycle Plot

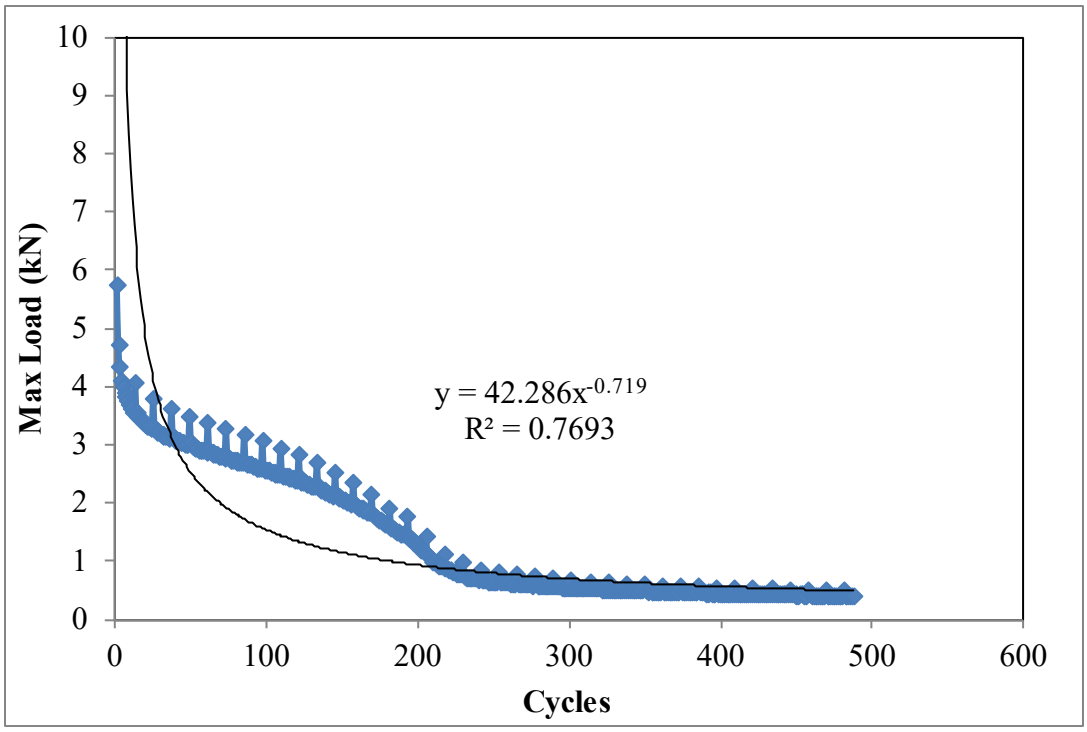

Figure G.7: Sample S11 Load vs Cycle Plot

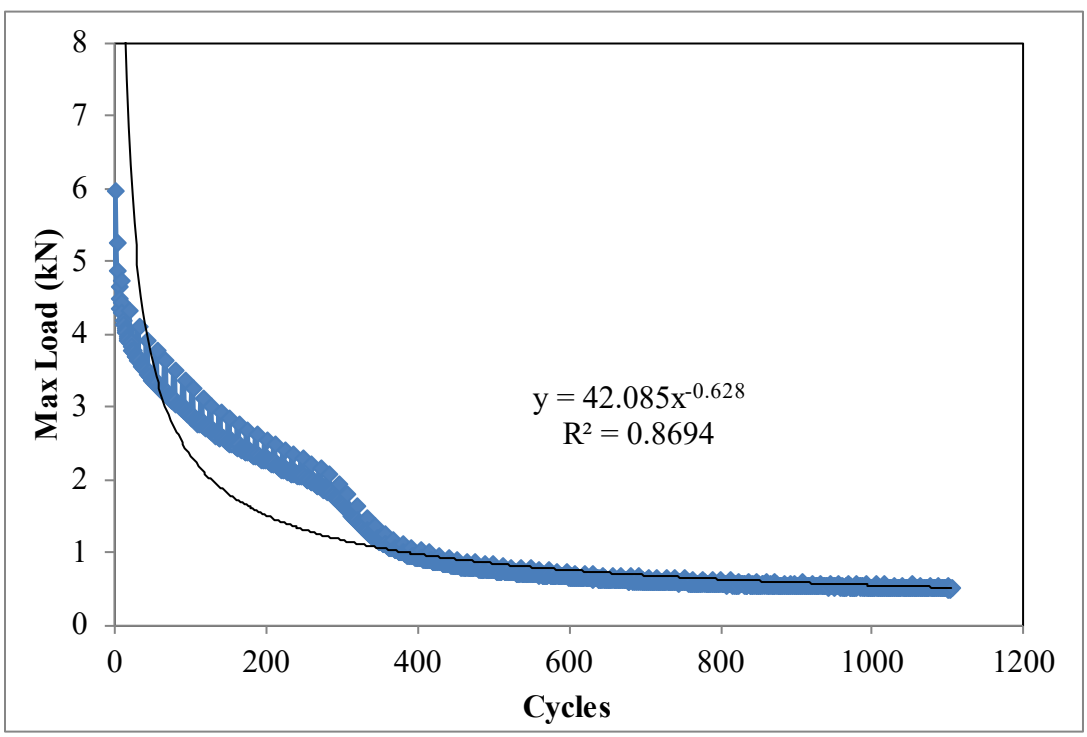

Figure G.8: Sample S14 Load vs Cycle Plot

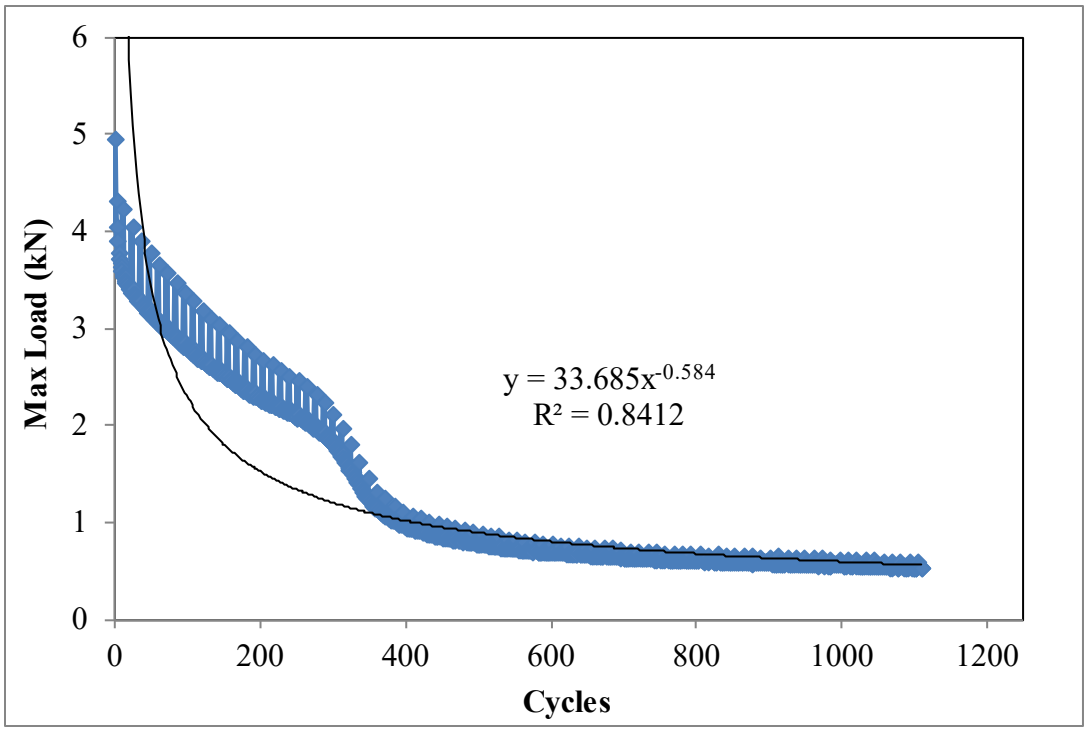

Figure G.9: Sample N8 Load vs Cycle Plot

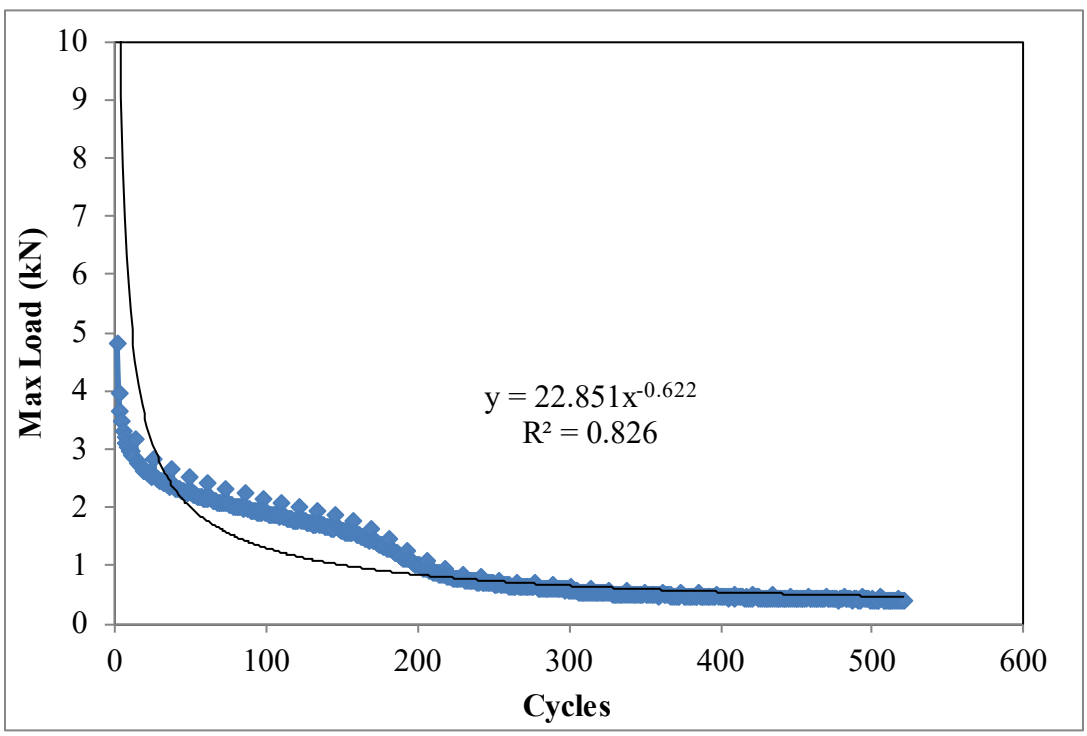

Figure G.10: Sample N9 Load vs Cycle Plot

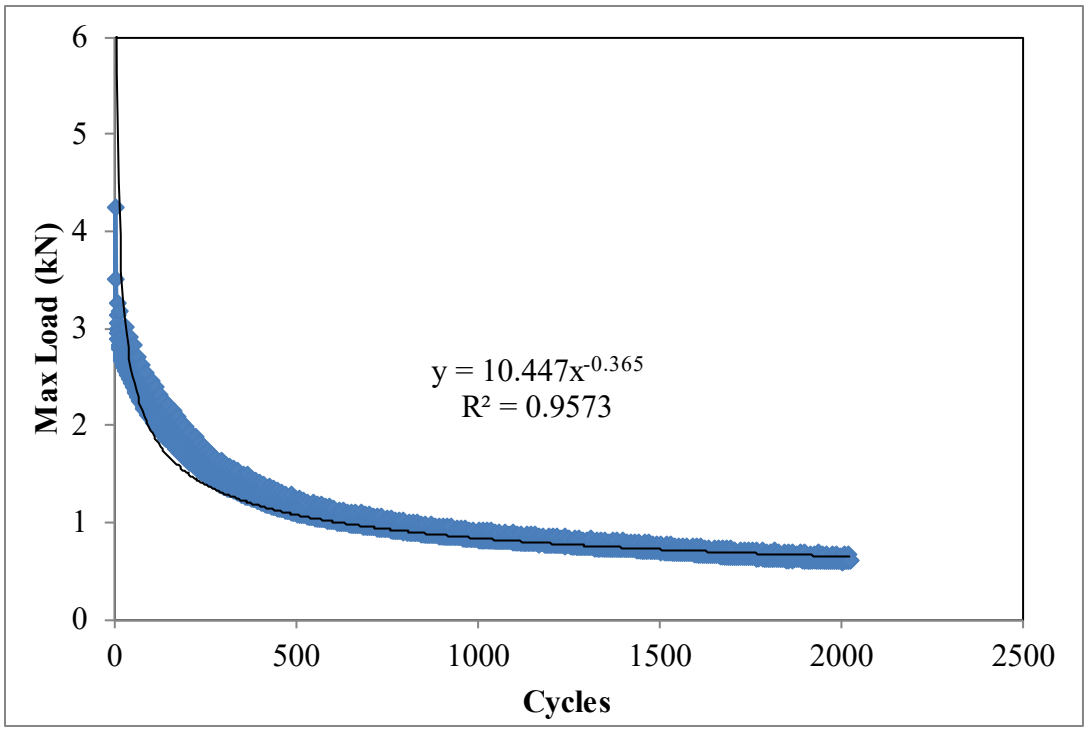

Figure G.11: Sample N10 Load vs Cycle Plot

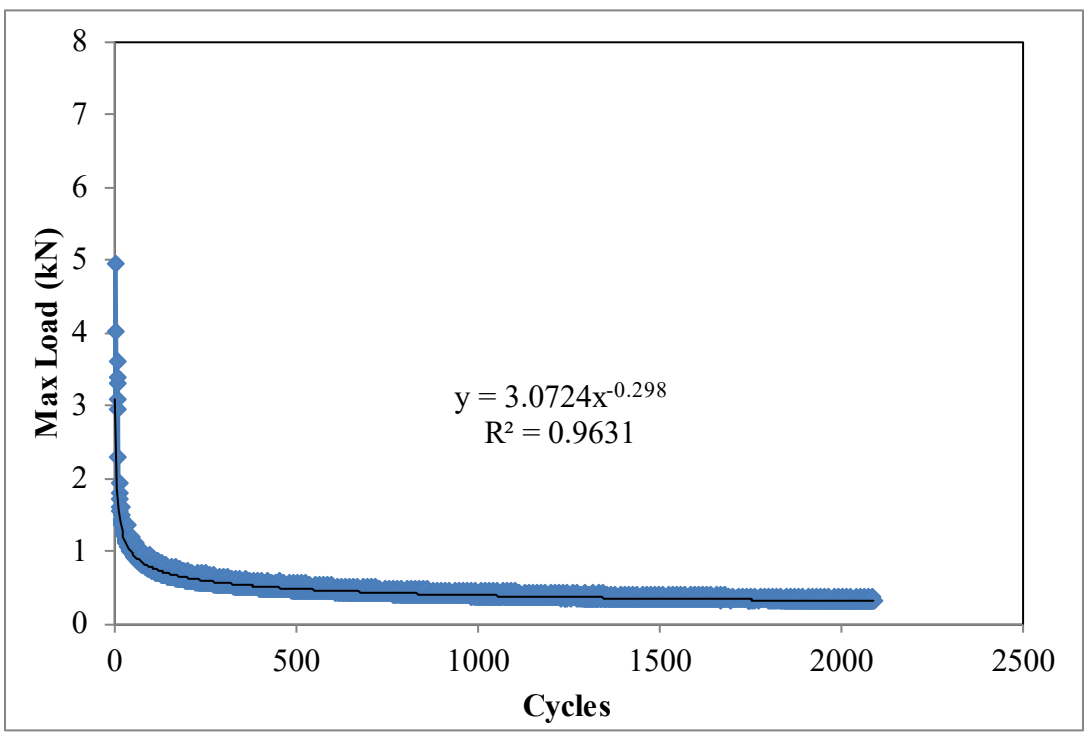

Figure G.12: Sample N12 Load vs Cycle Plot

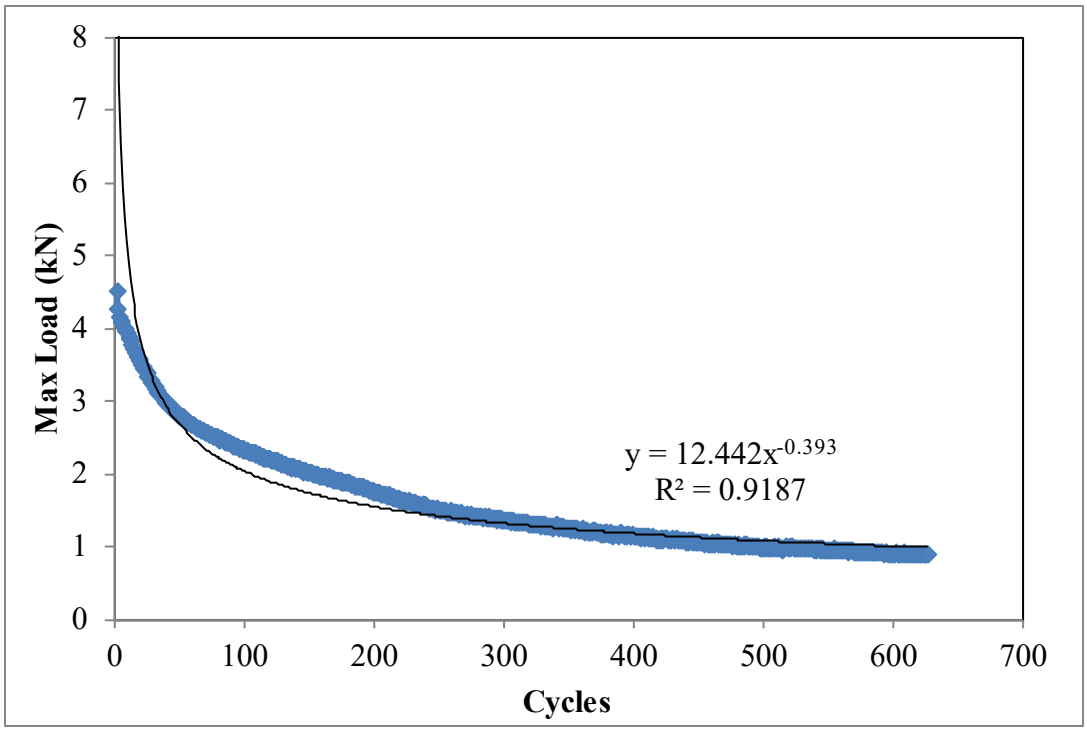

Figure G.13: Sample N14 Load vs Cycle Plot

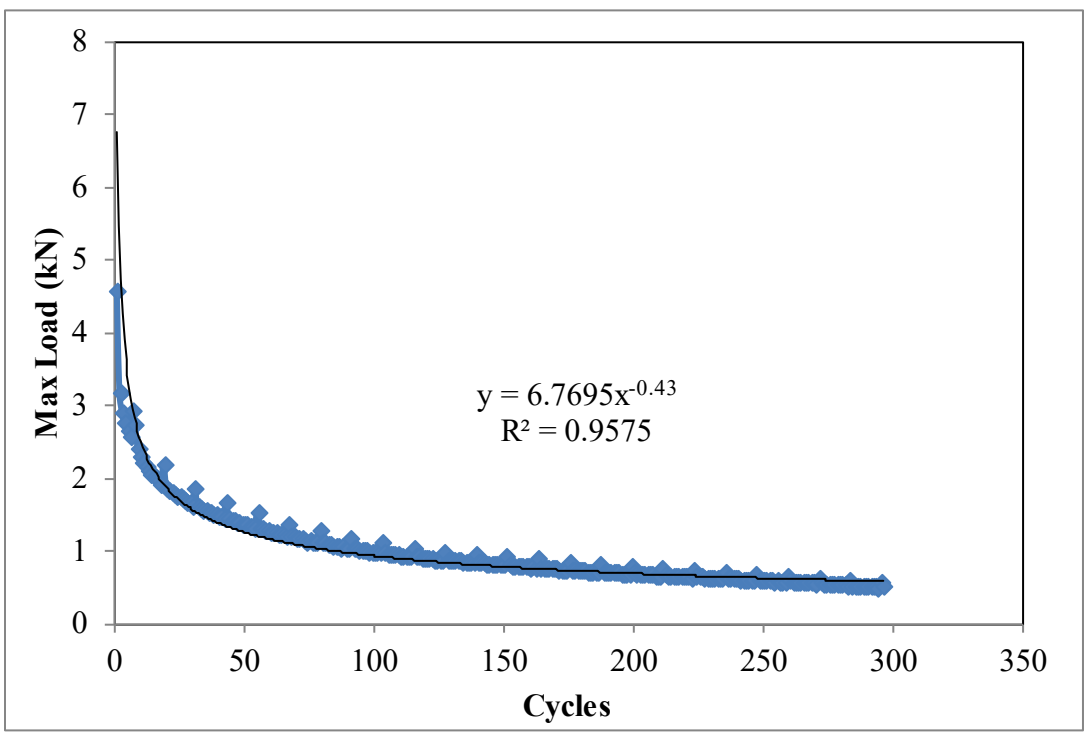

Figure G.14: Sample N17 Load vs Cycle Plot

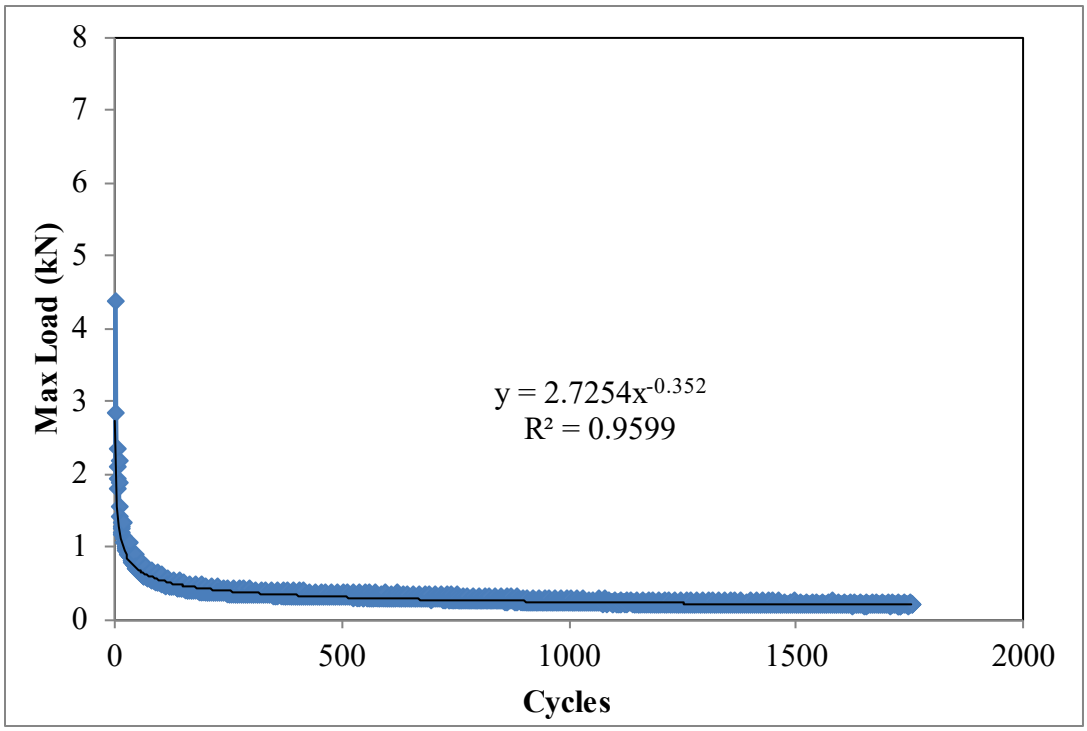

Figure G.15: Sample N18 Load vs Cycle Plot

APPENDIX – H: CUSTOMIZED OT SPECIMEN STRAIN GAGE VALUES

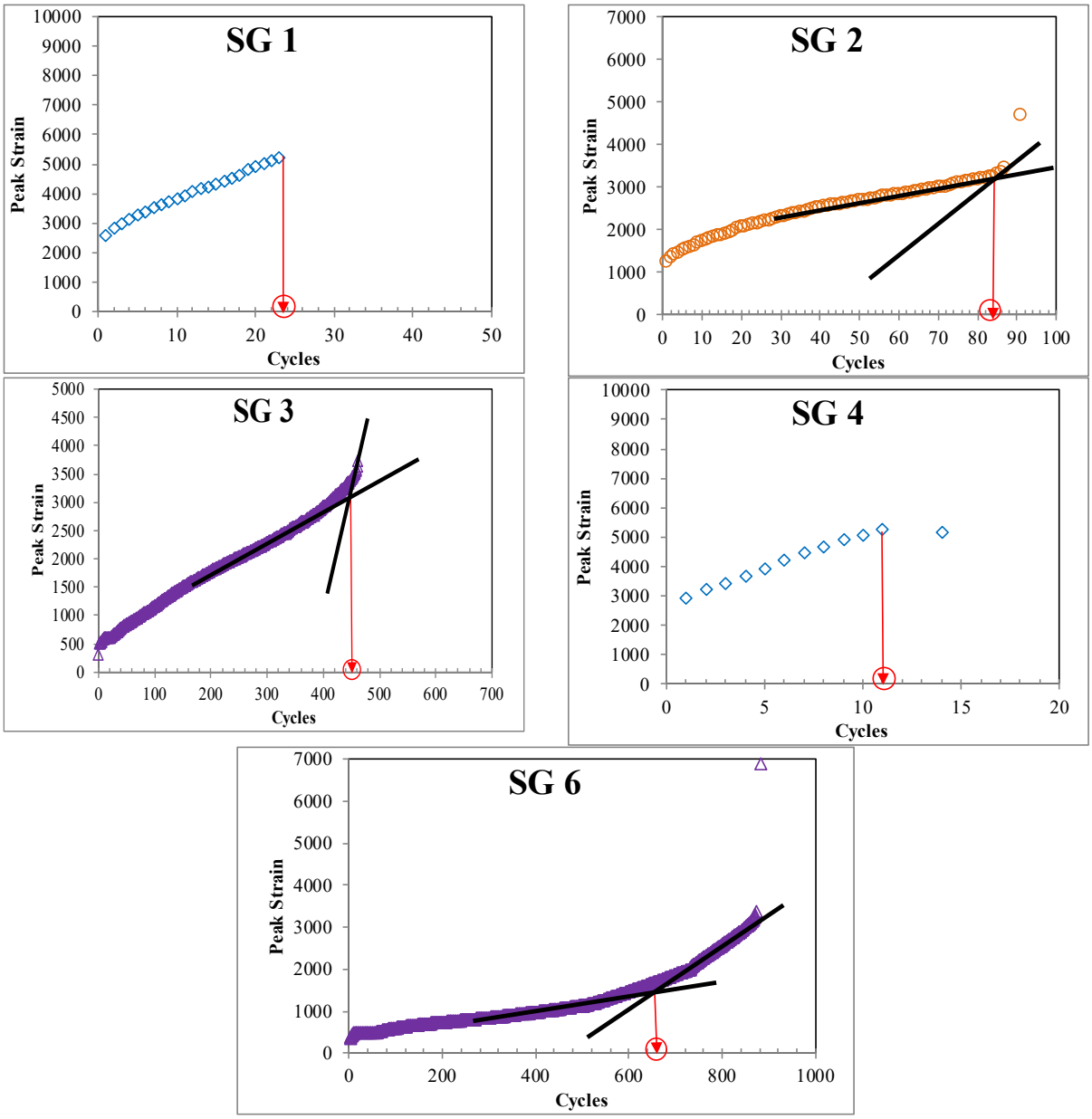

Figure H.1: Sample S1 Strain Gage Responses

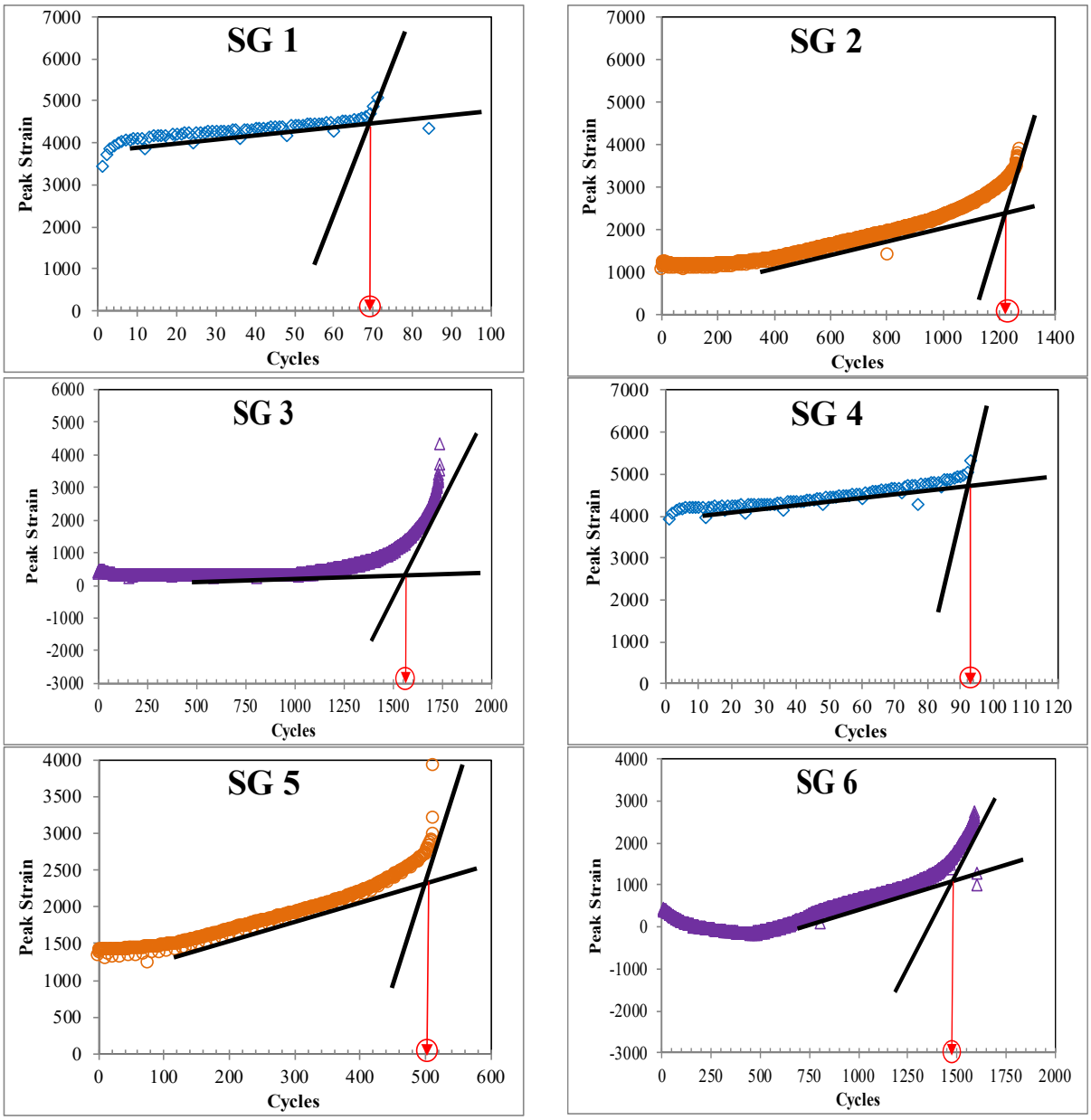

Figure H.2: Sample S2 Strain Gage Responses

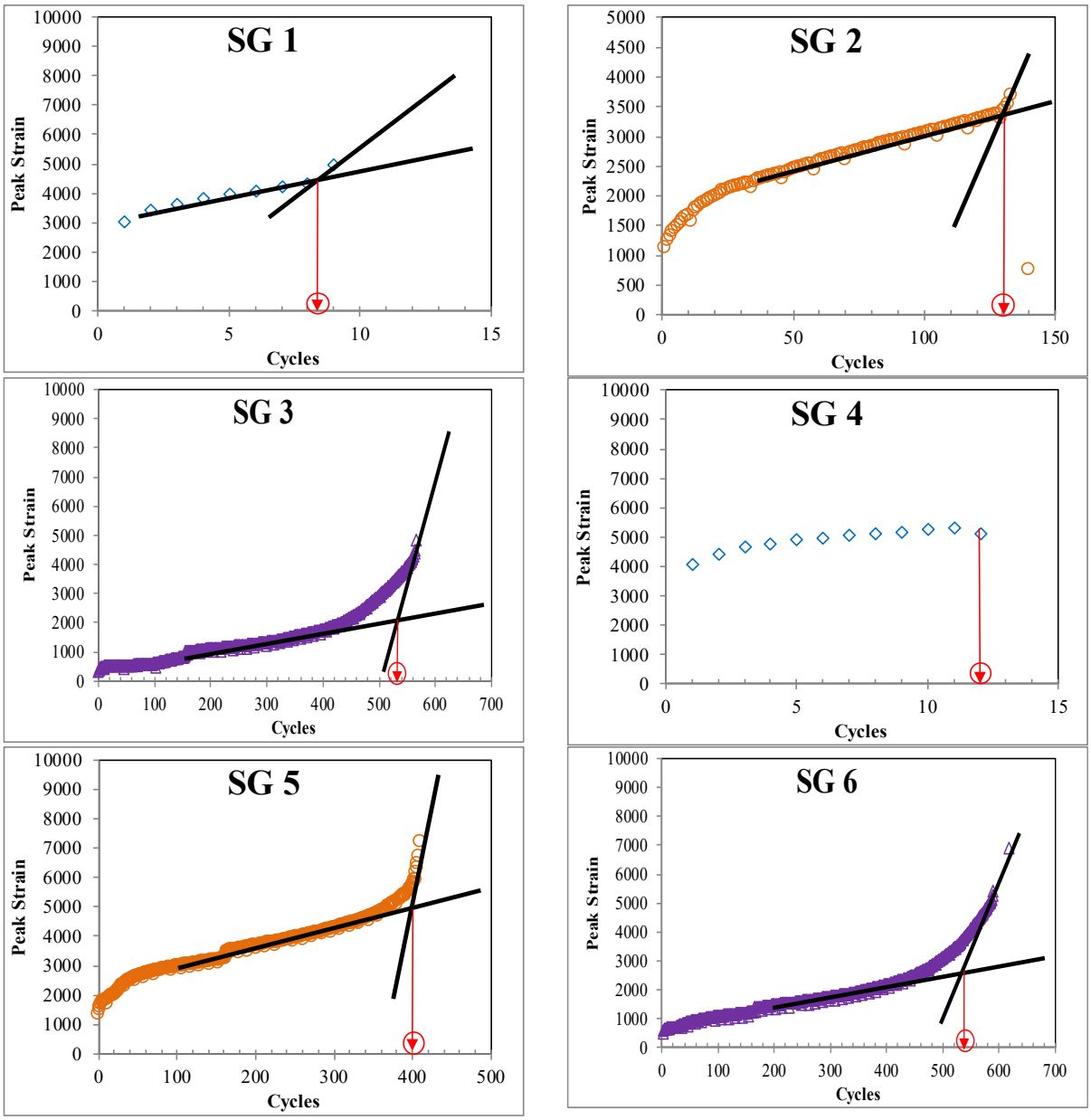

Figure H.3: Sample S3 Strain Gage Responses

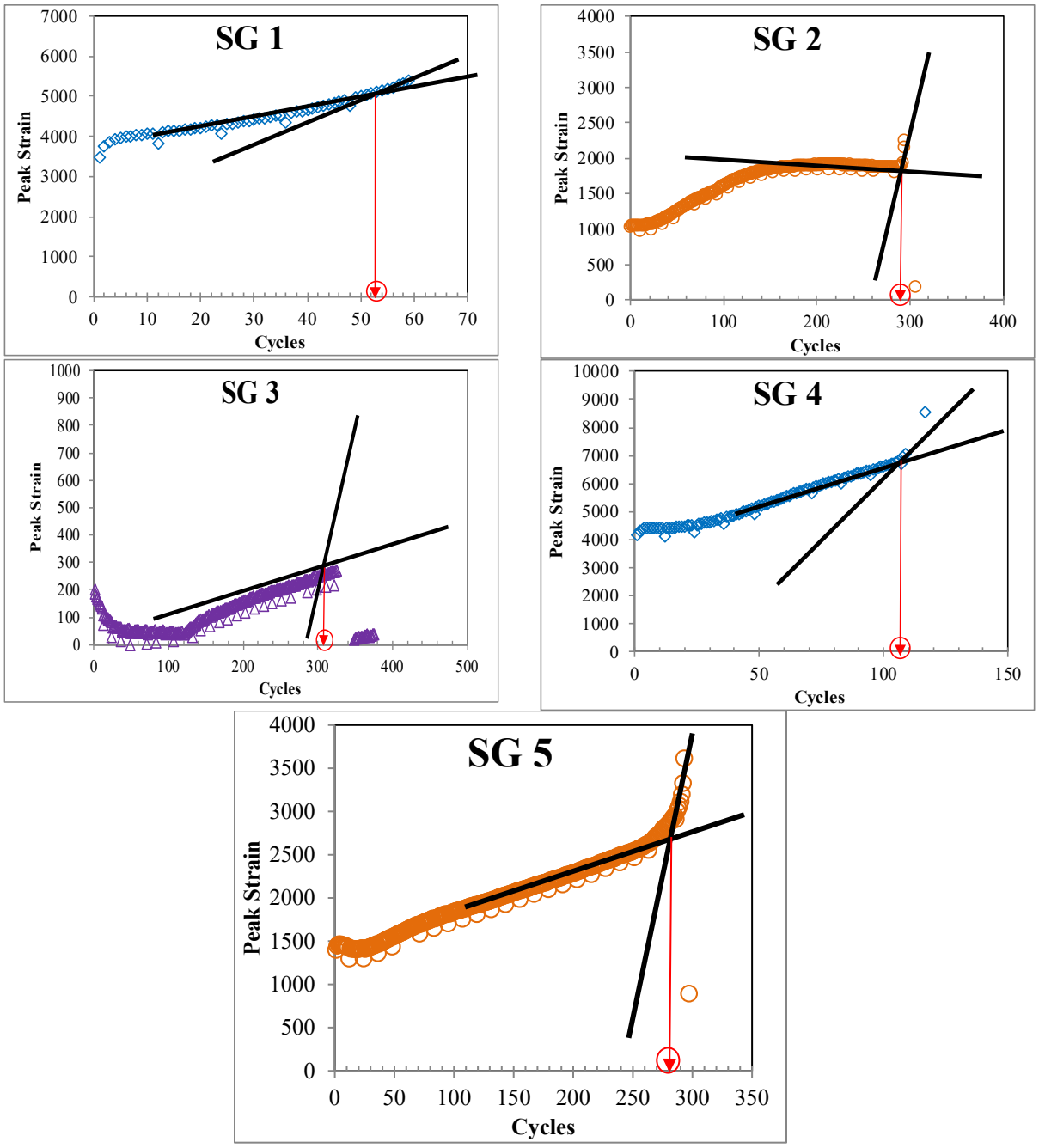

Figure H.4: Sample S7 Strain Gage Responses

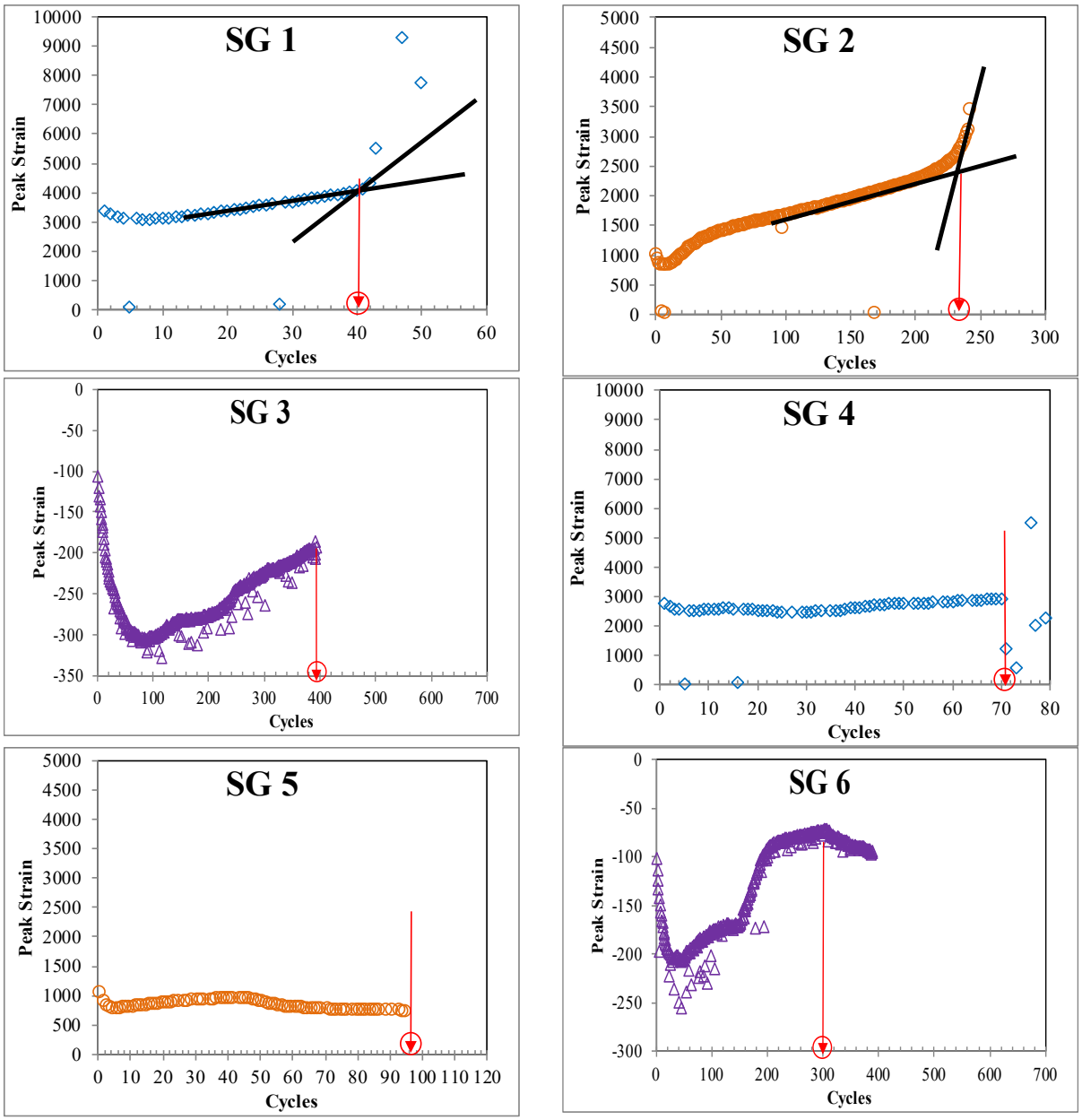

Figure H.5: Sample S9 Strain Gage Responses

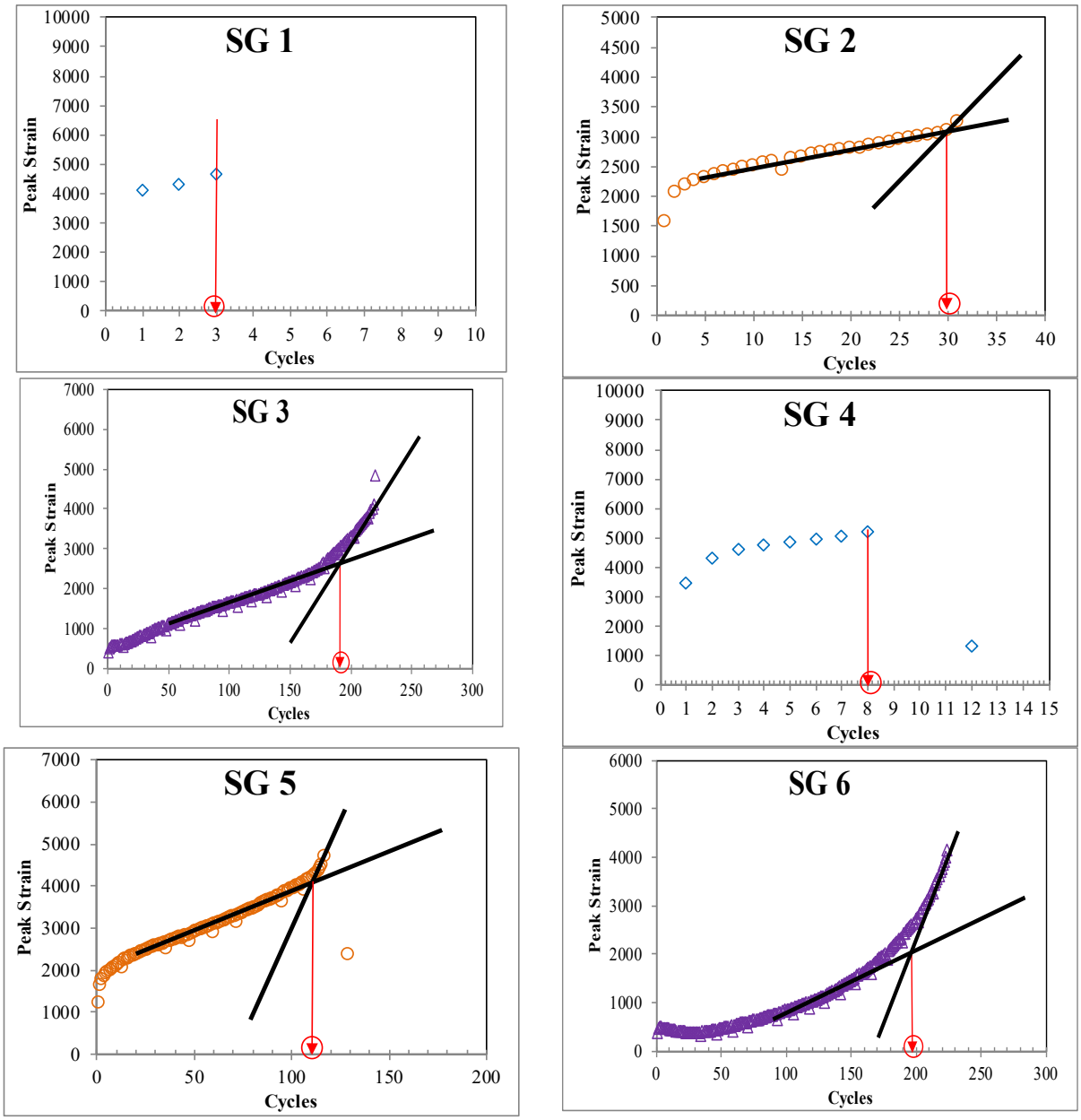

Figure H.6: Sample S10 Strain Gage Responses

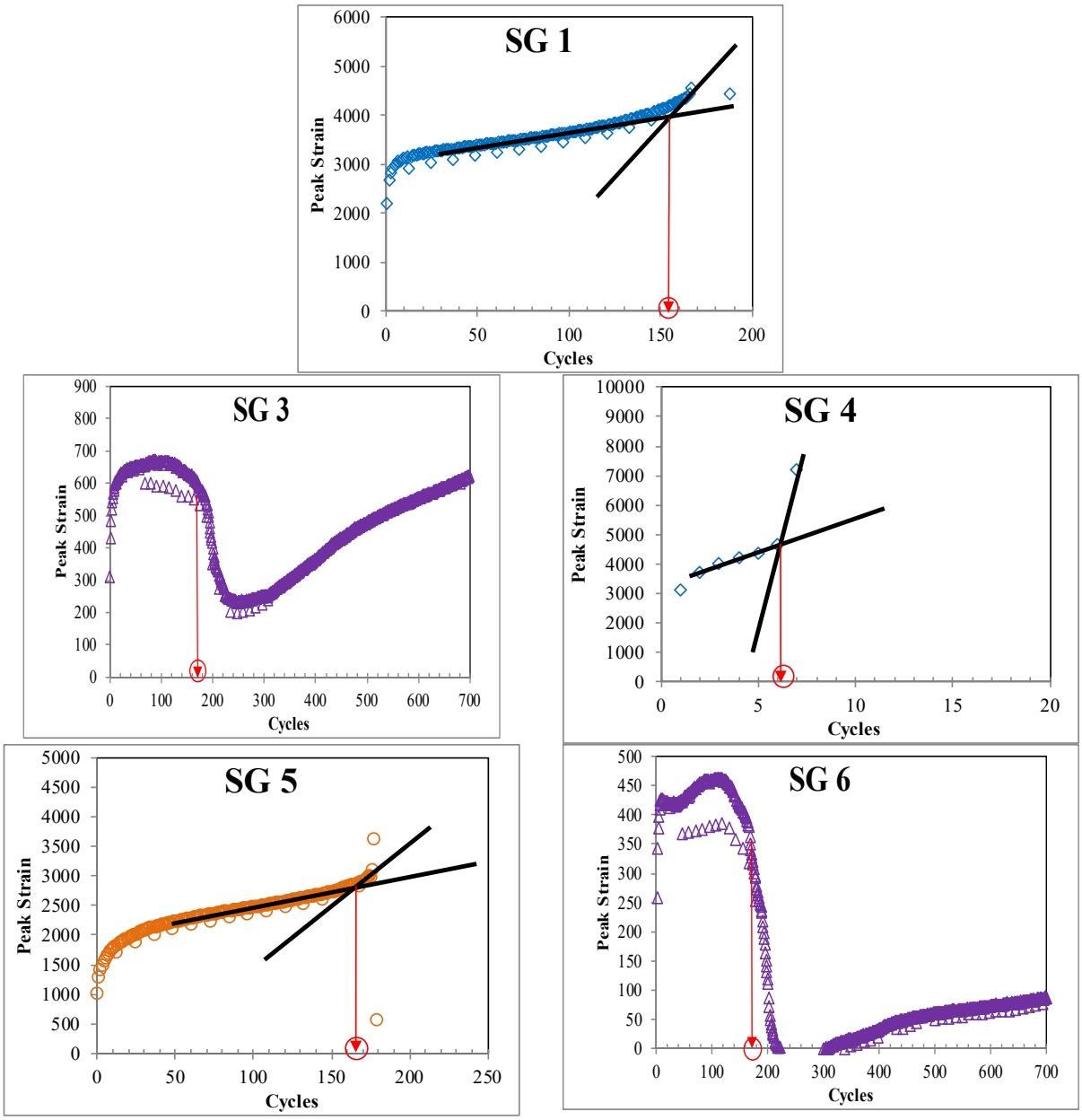

Figure H.7: Sample S11 Strain Gage Responses

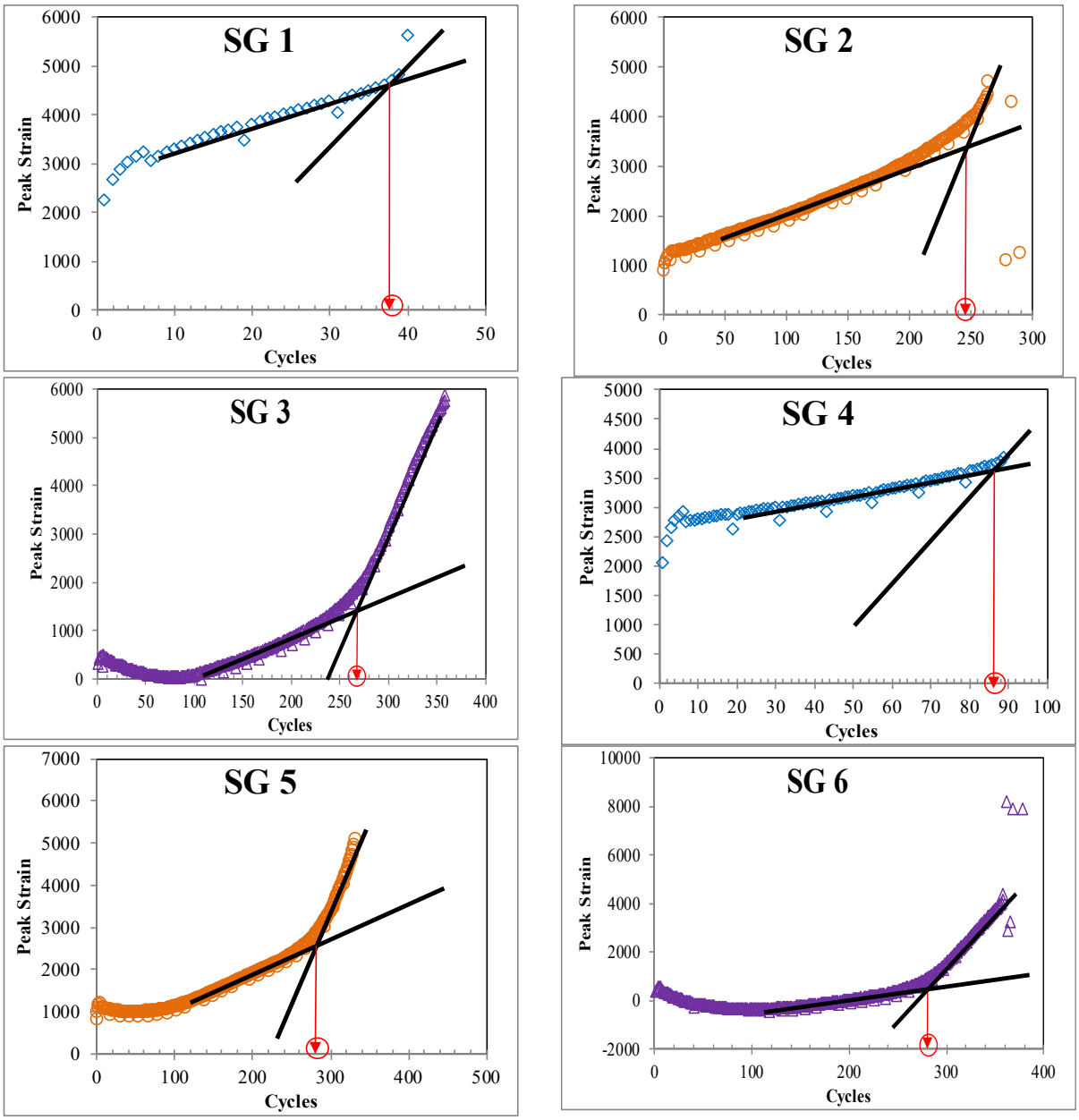

Figure H.8: Sample S14 Strain Gage Responses

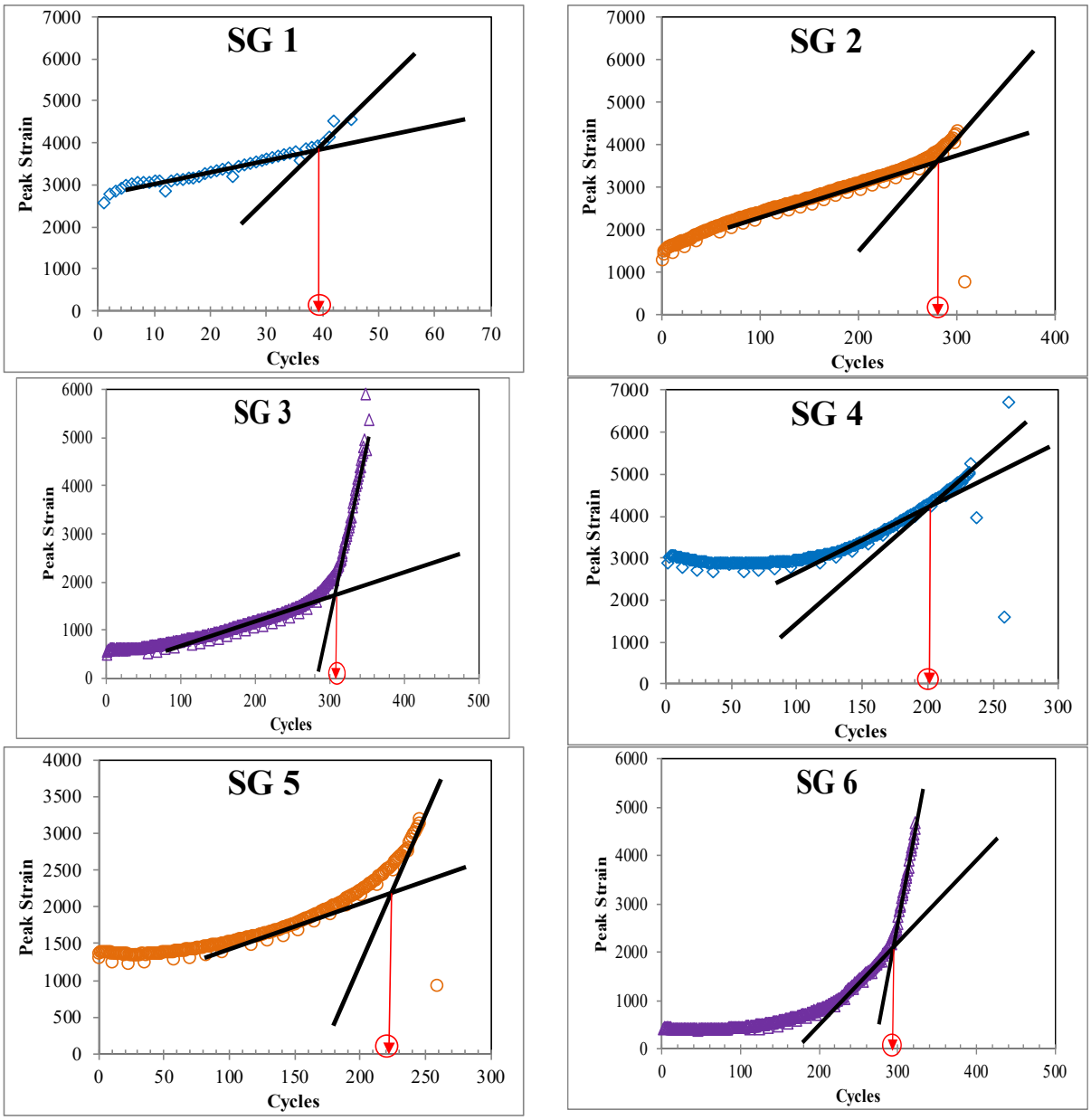

Figure H.9: Sample N8 Strain Gage Responses

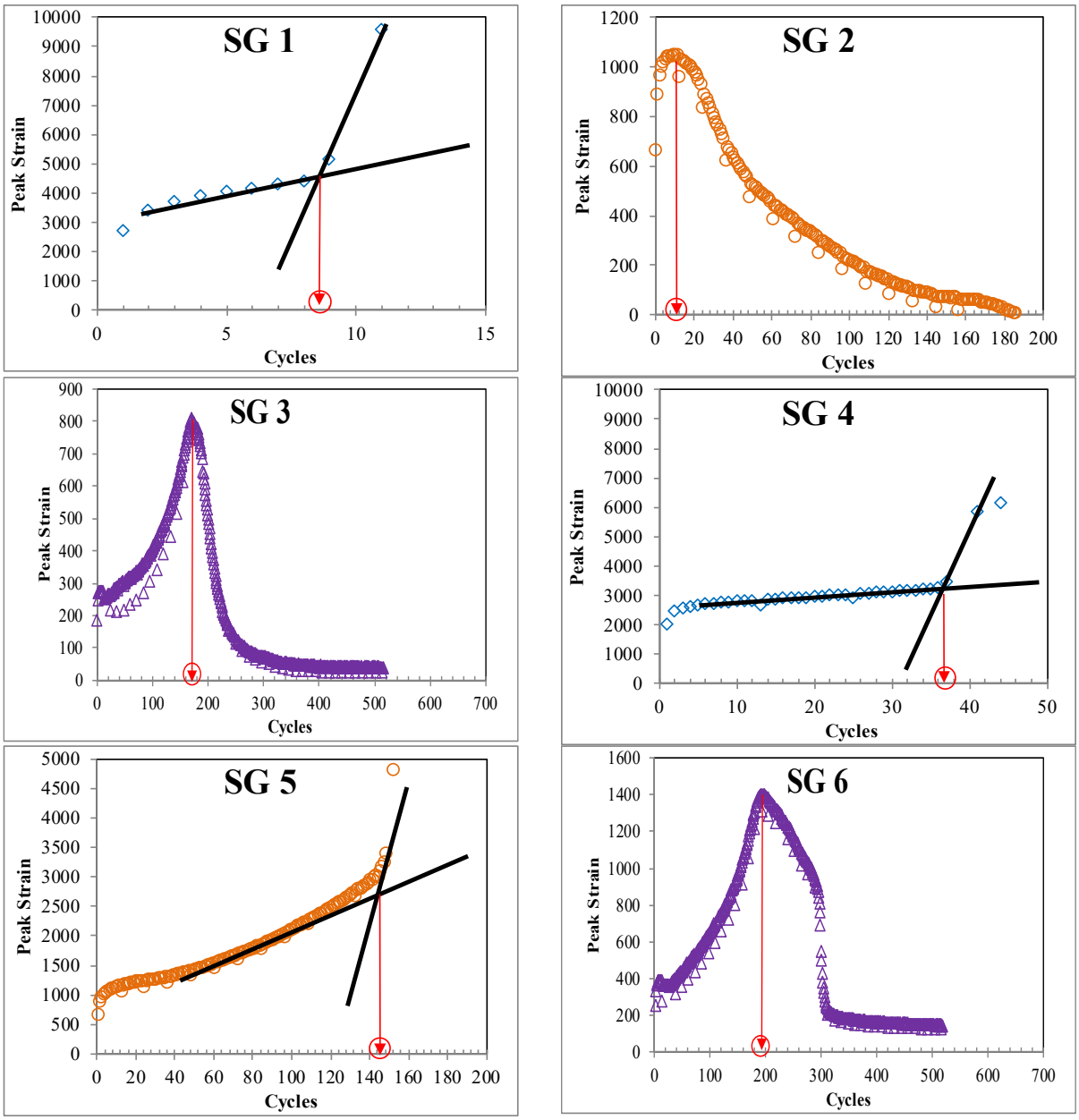

Figure H.10: Sample N9 Strain Gage Responses

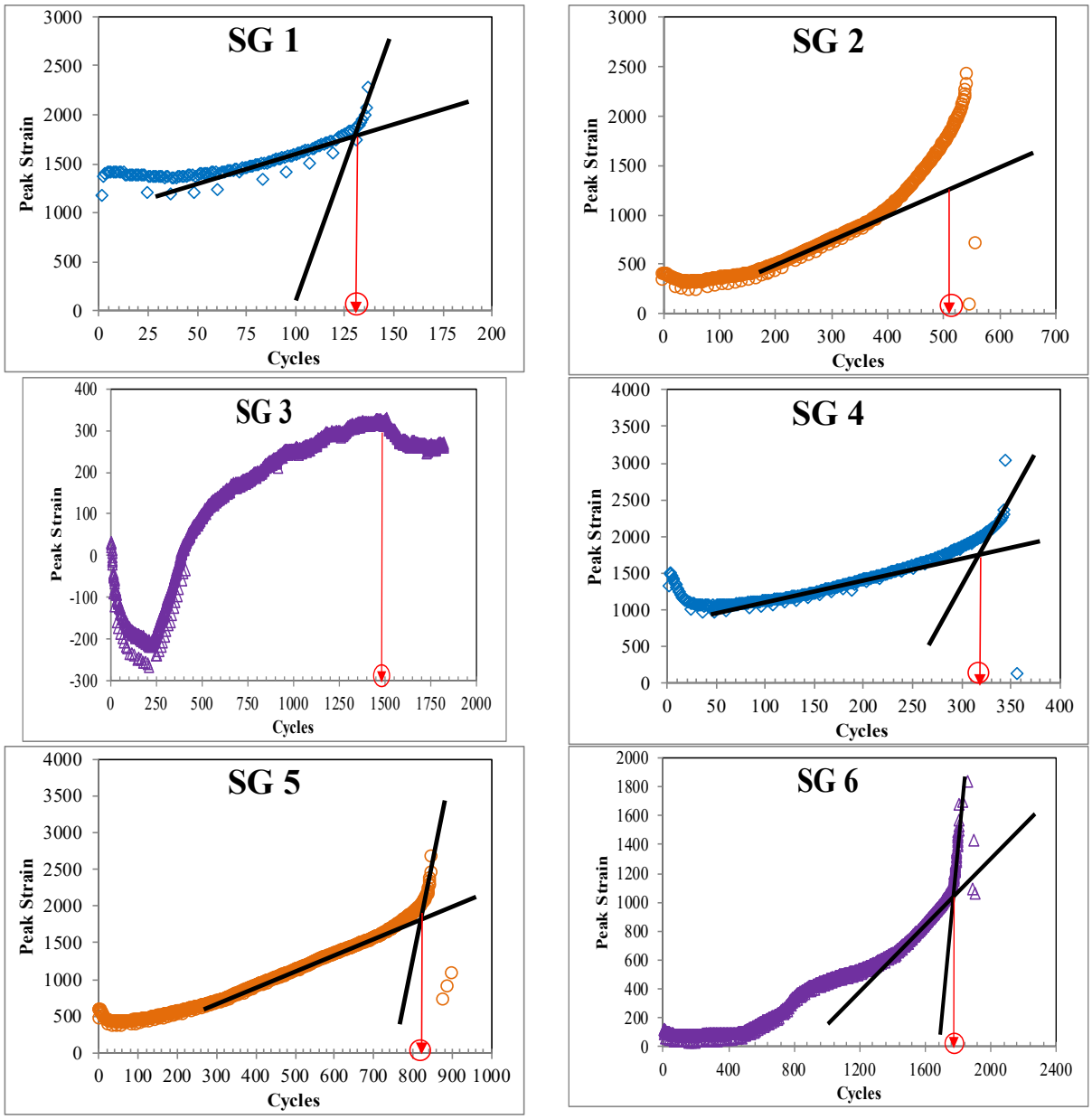

Figure H.11: Sample N10 Strain Gage Responses

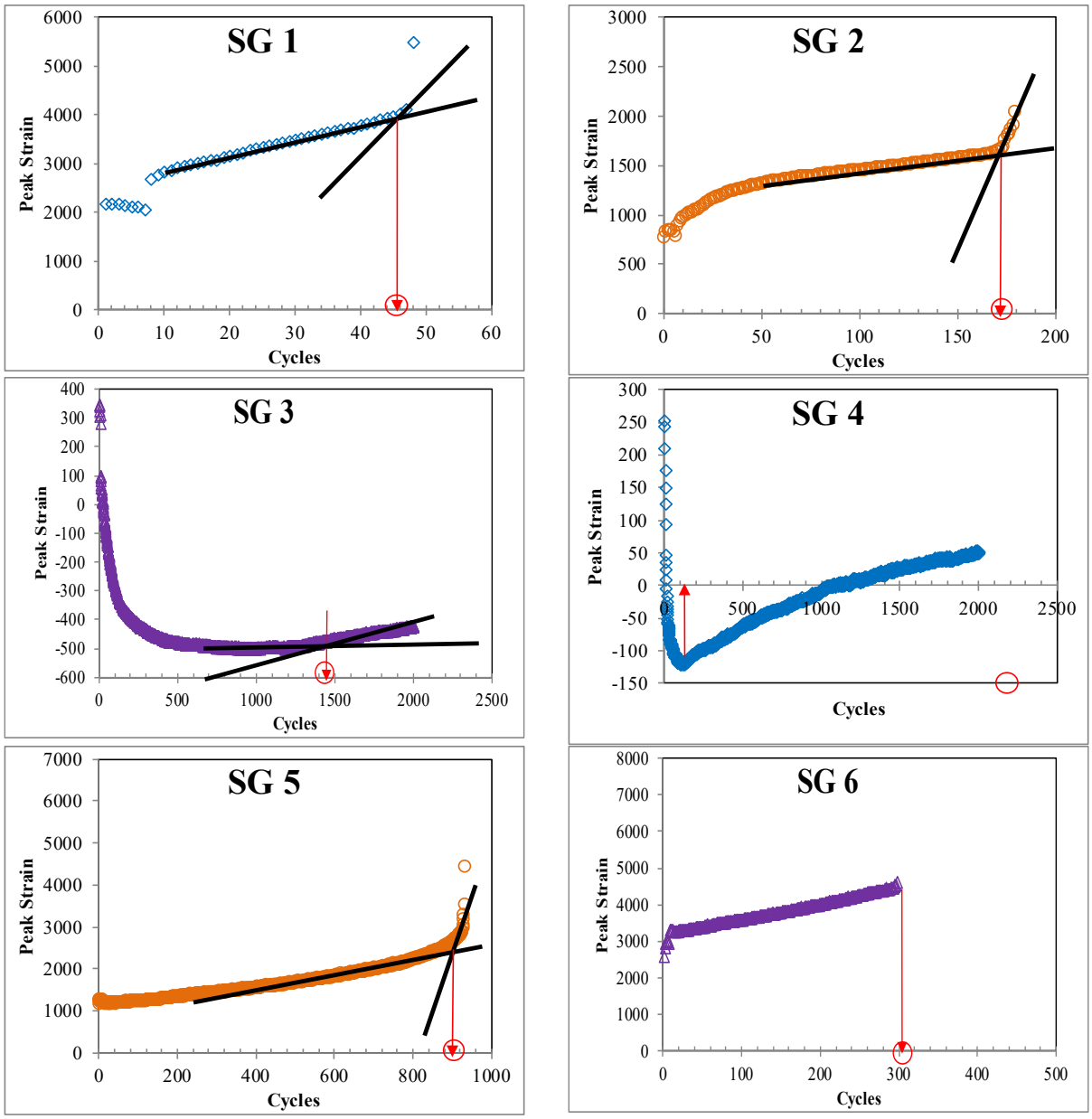

Figure H.12: Sample N12 Strain Gage Responses

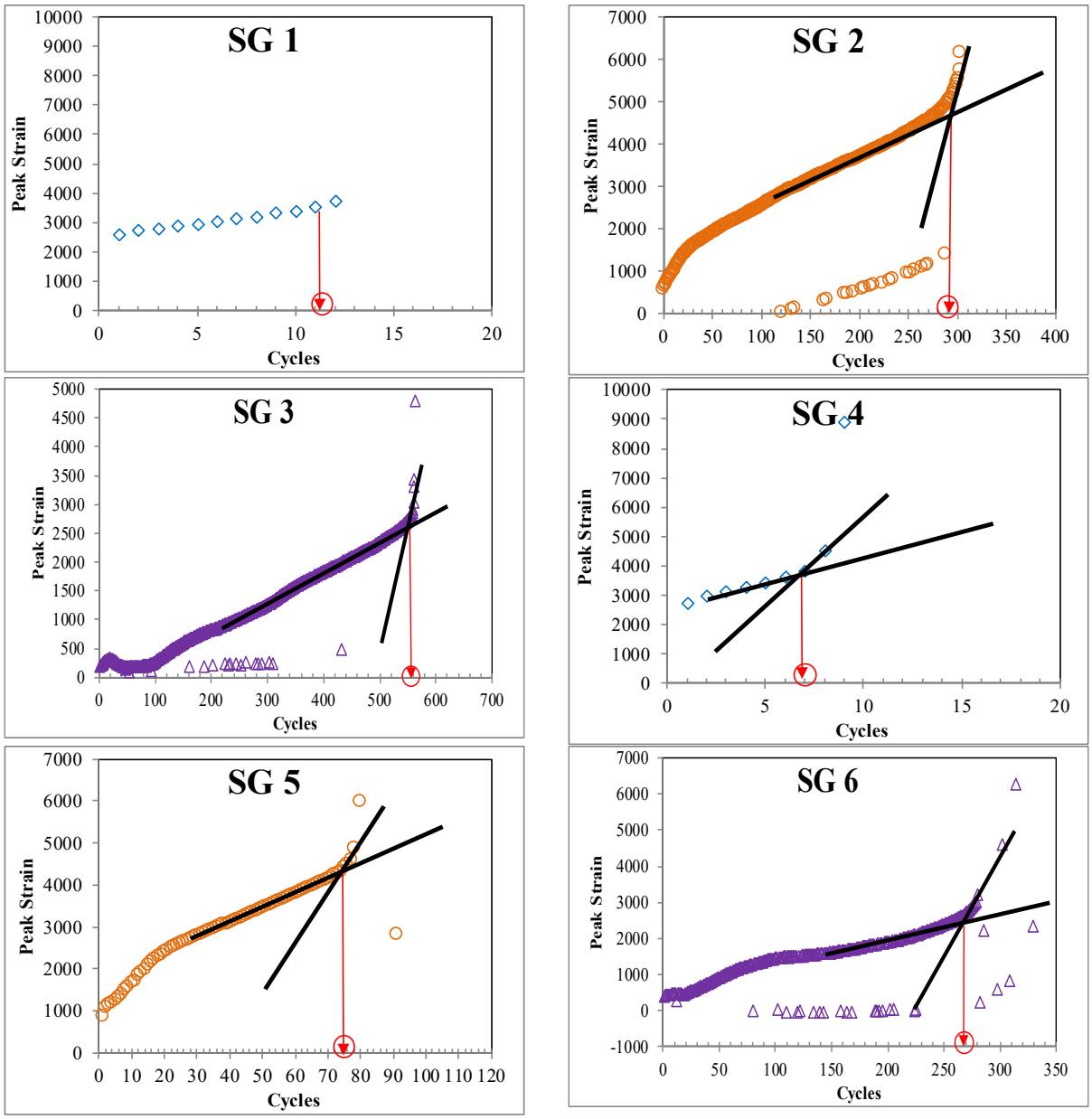

Figure H.13: Sample N14 Strain Gage Responses

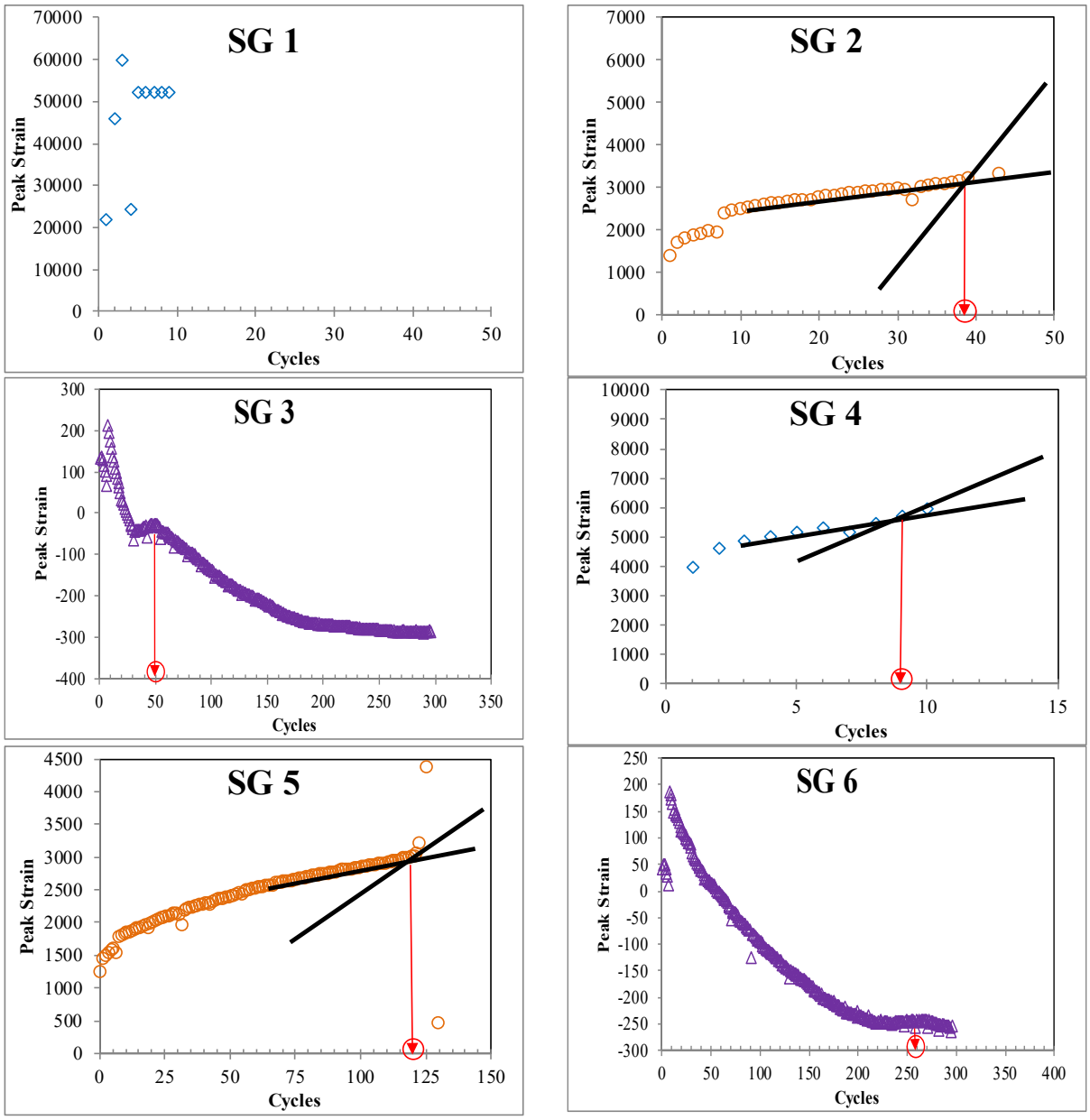

Figure H.14: Sample N17 Strain Gage Responses

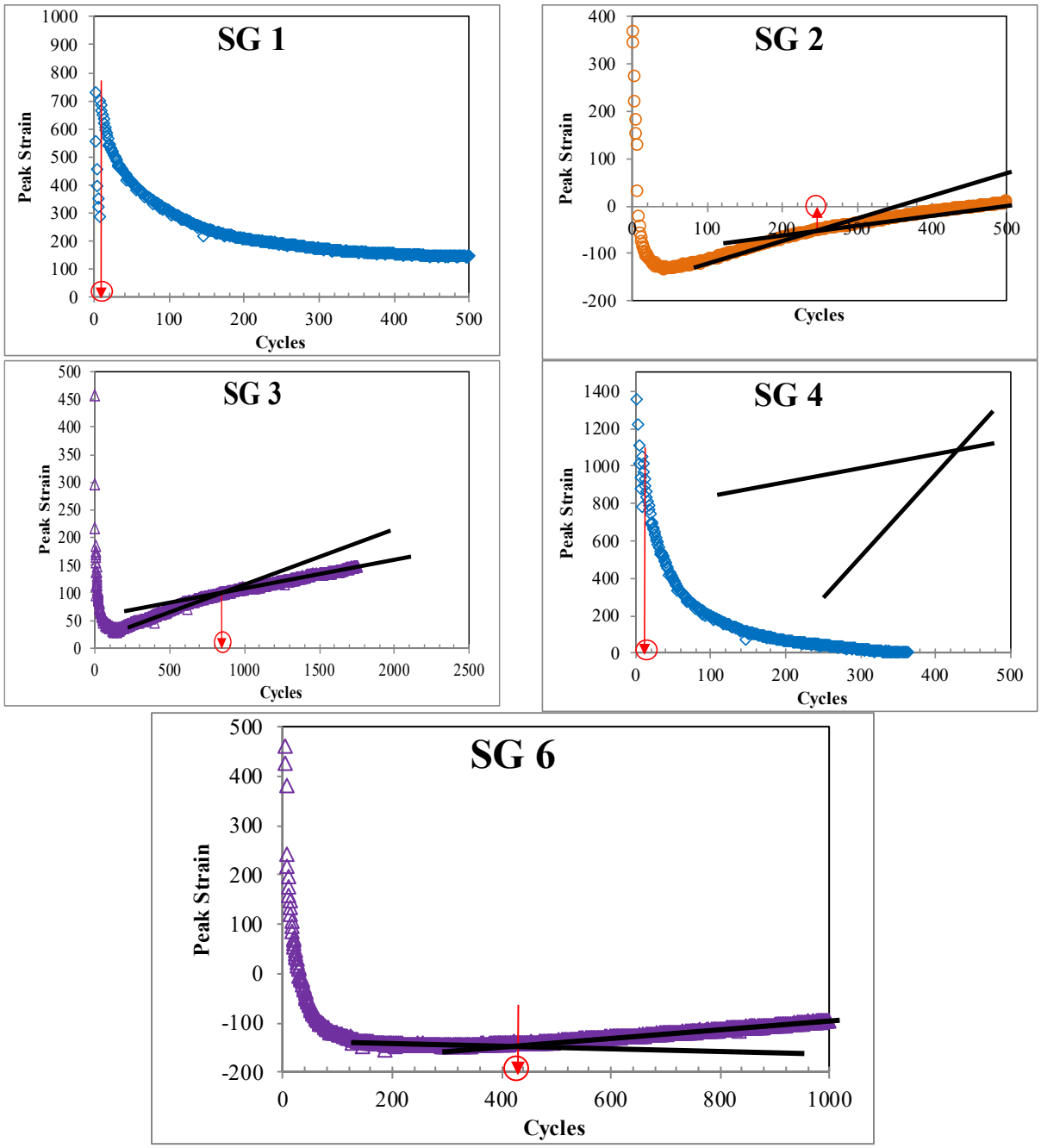

Figure H.15: Sample N18 Strain Gage Responses

APPENDIX – I: CUSTOMIZED OT SPECIMEN SAMPLE PICTURES

(a) Front Side

(b) Back Side

(c) Top Side

Figure I.1: Sample S1 Pictures

(a) Front Side

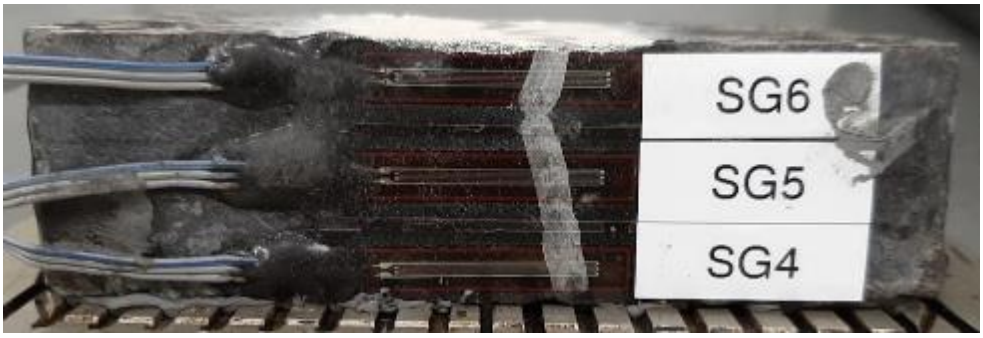

(b) Back Side

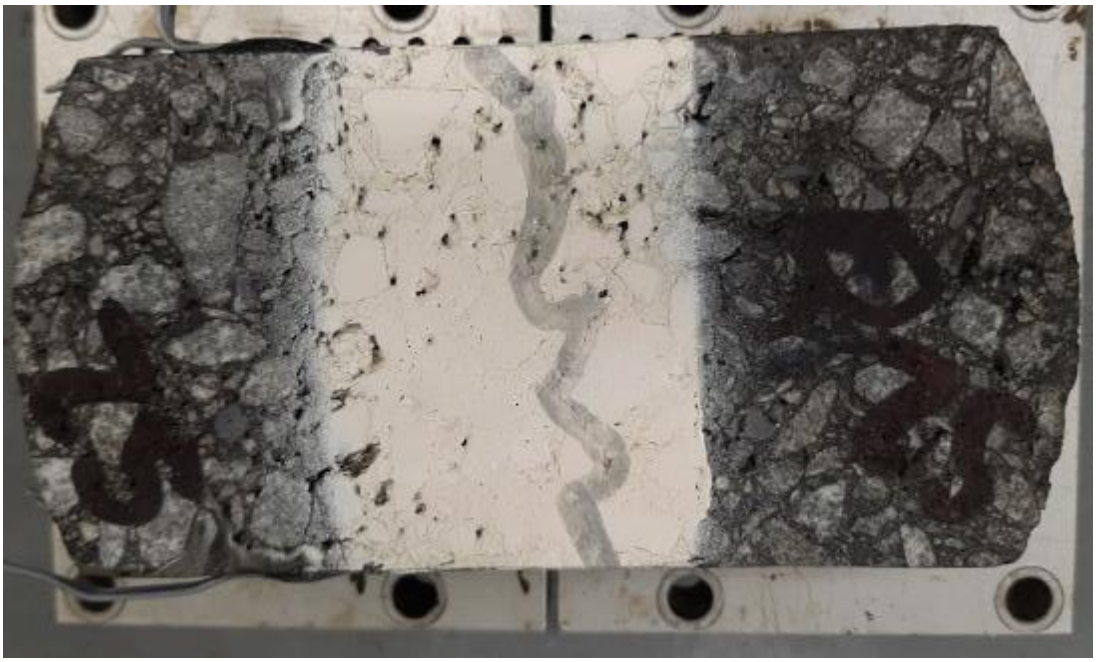

(c) Top Side

Figure I.2: Sample S2 Pictures

(a) Front Side

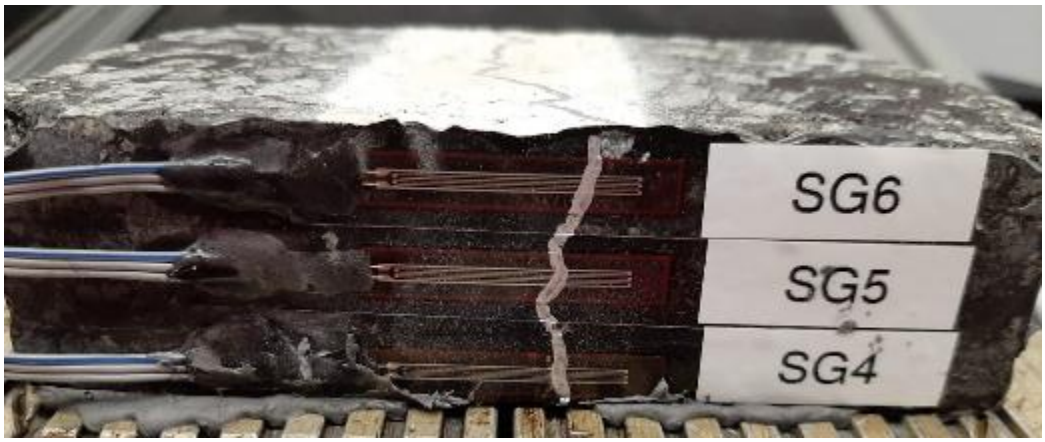

(b) Back Side

(c) Top Side

Figure I.3: Sample S3 Pictures

(a) Front Side

(b) Back Side

(c) Top Side

Figure I.4: Sample S7 Pictures

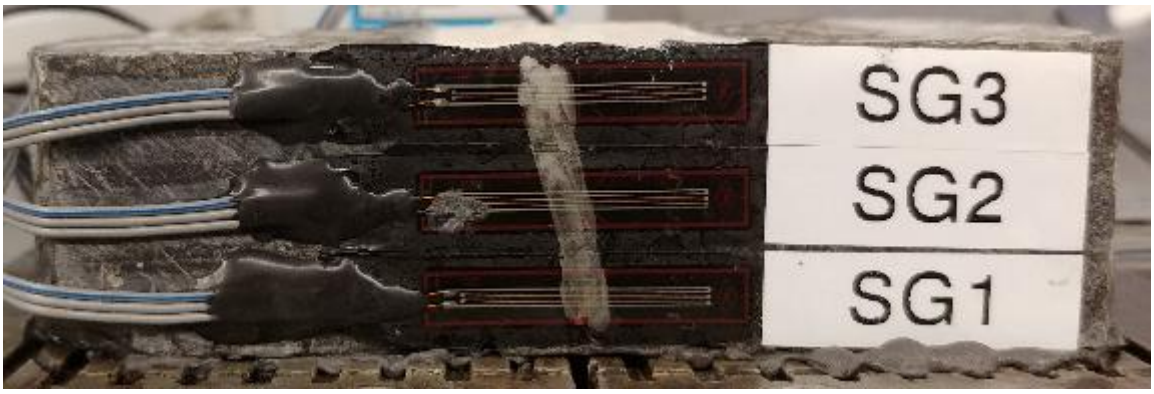

(a) Front Side

(b) Back Side

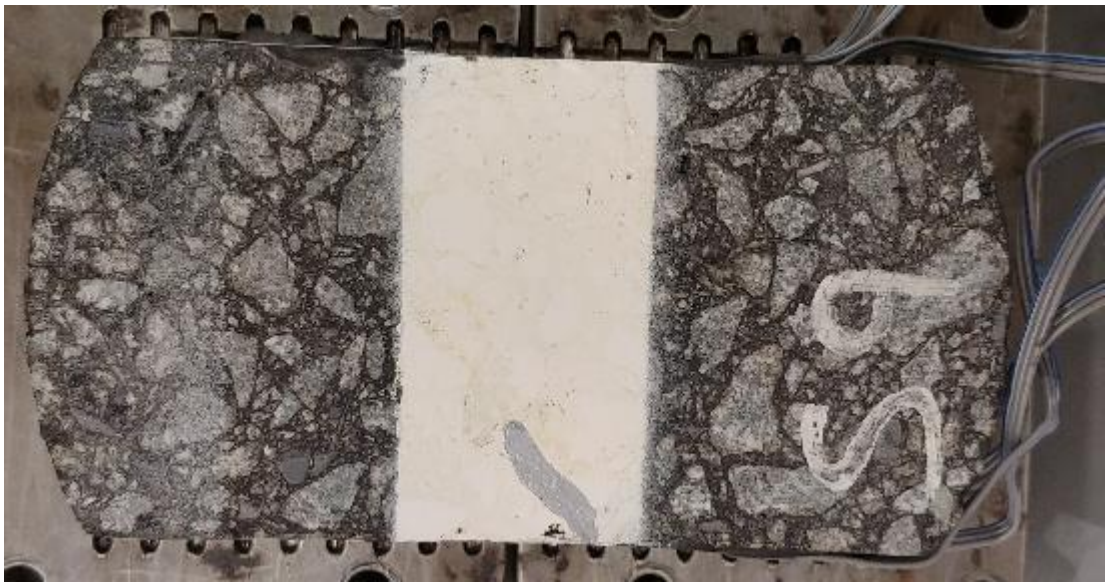

(c) Top Side

Figure I.5: Sample S9 Pictures

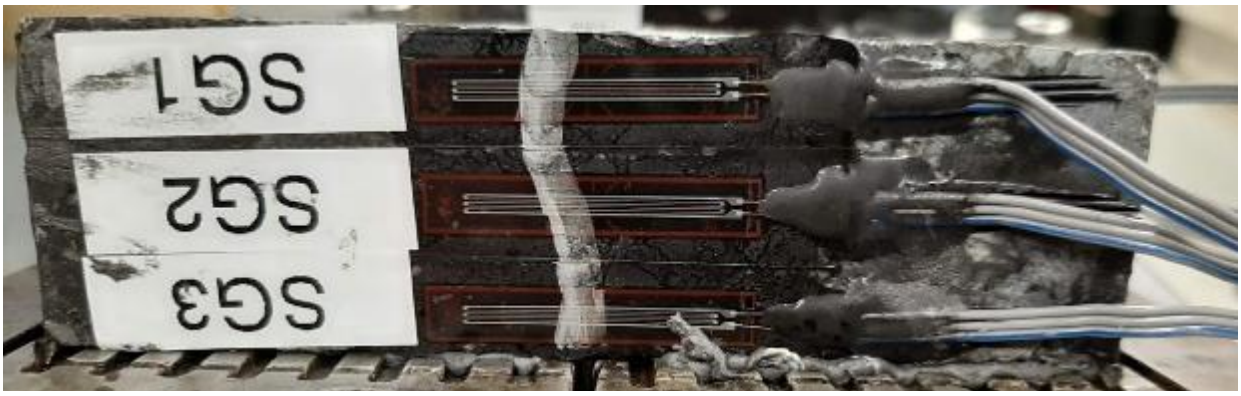

(d) Front Side

(e) Back Side

(f) Top Side

Figure I.6: Sample S10 Pictures

(a) Front Side

(b) Back Side

(c) Top Side

Figure I.7: Sample S11 Pictures

(a) Front Side

(b) Back Side

(c) Top Side

Figure I.8: Sample S14 Pictures

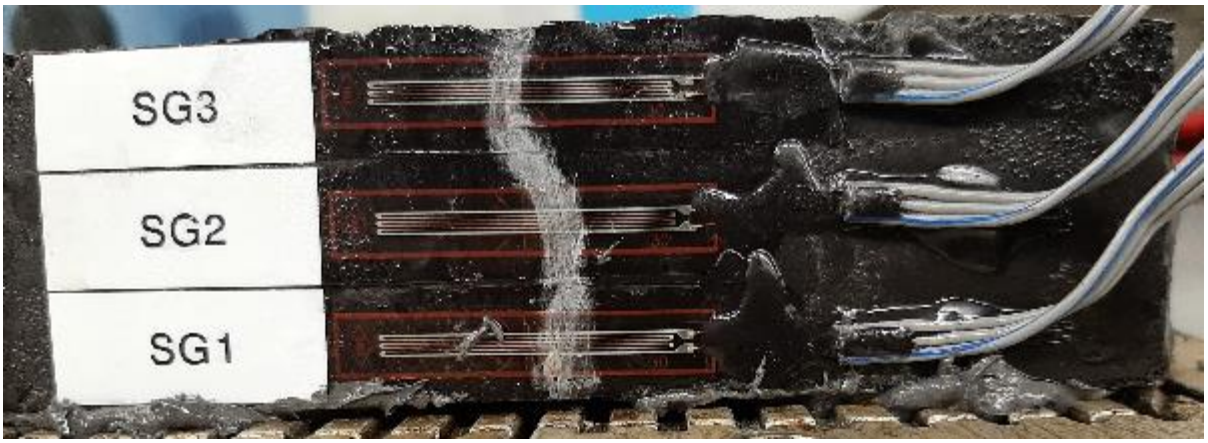

(a) Front Side

(b) Back Side

(c) Top Side

Figure I.9: Sample N8 Pictures

(a) Front Side

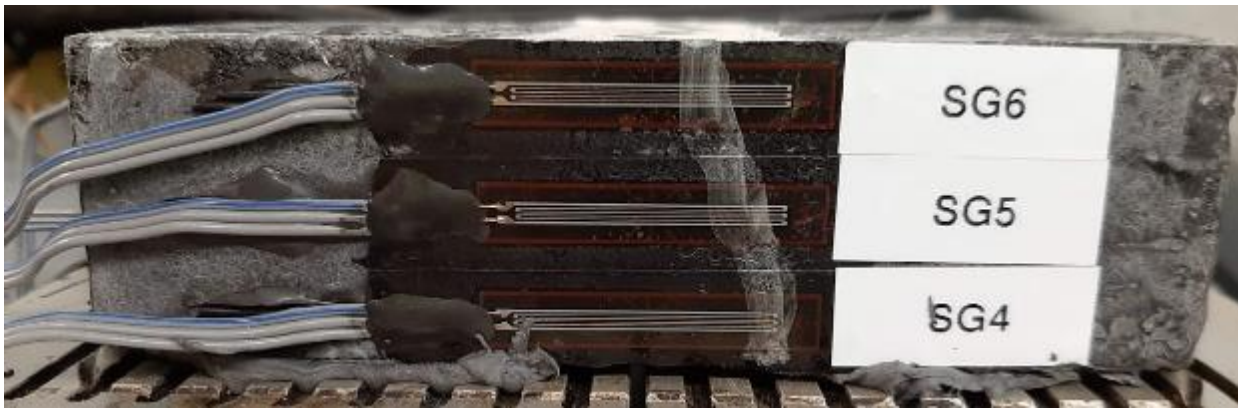

(b) Back Side

(c) Top Side

Figure I.10: Sample N9 Pictures

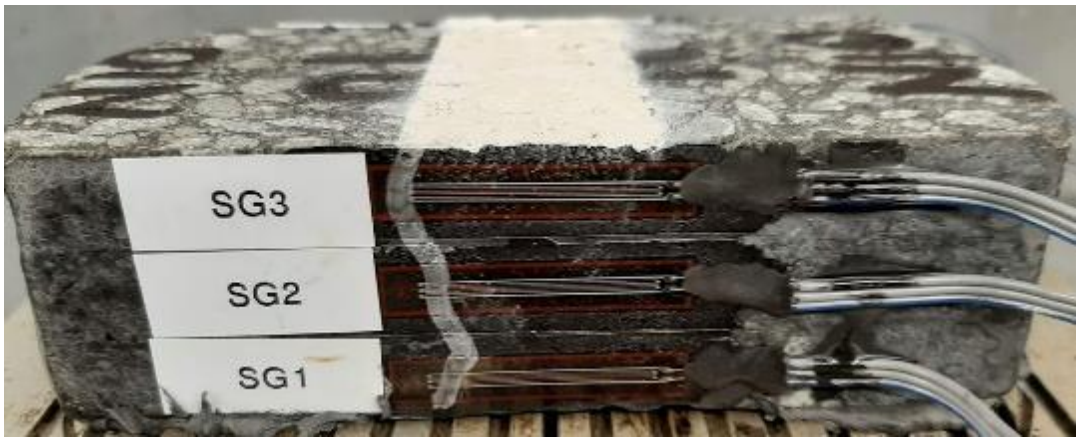

(a) Front Side

(b) Back Side

(c) Top Side

Figure I.11: Sample N10 Pictures

(a) Front Side

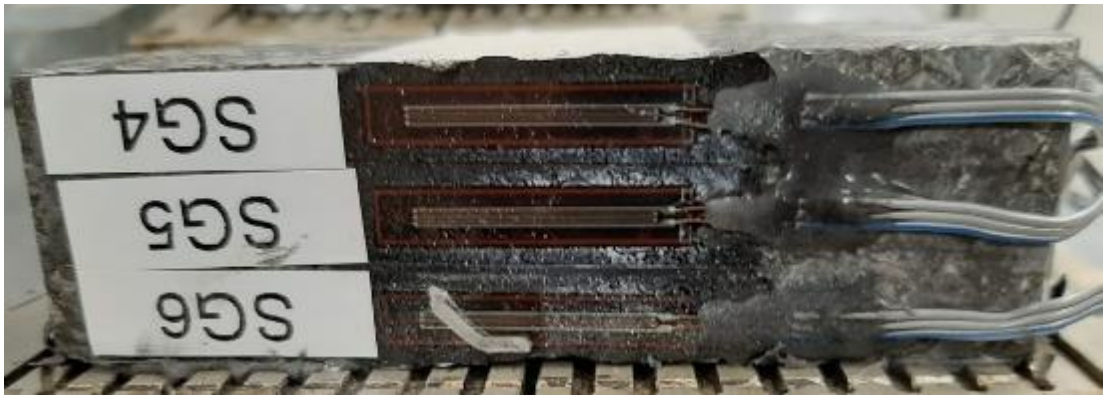

(b) Back Side

(c) Top Side

Figure I.12: Sample N12 Pictures

(a) Front Side

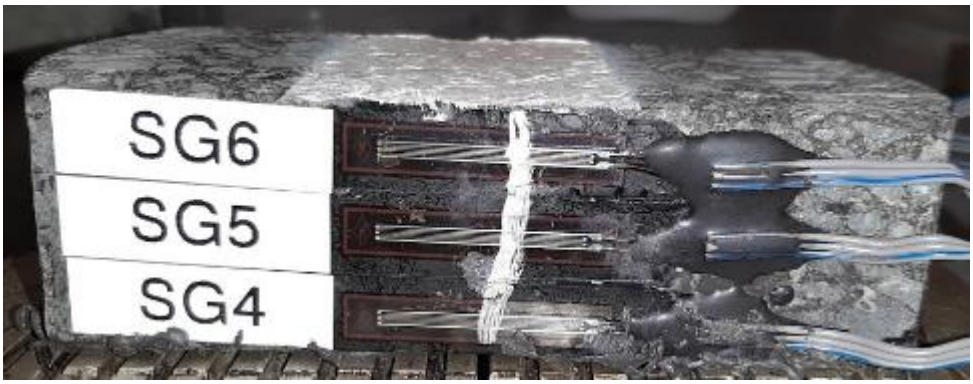

(b) Back Side

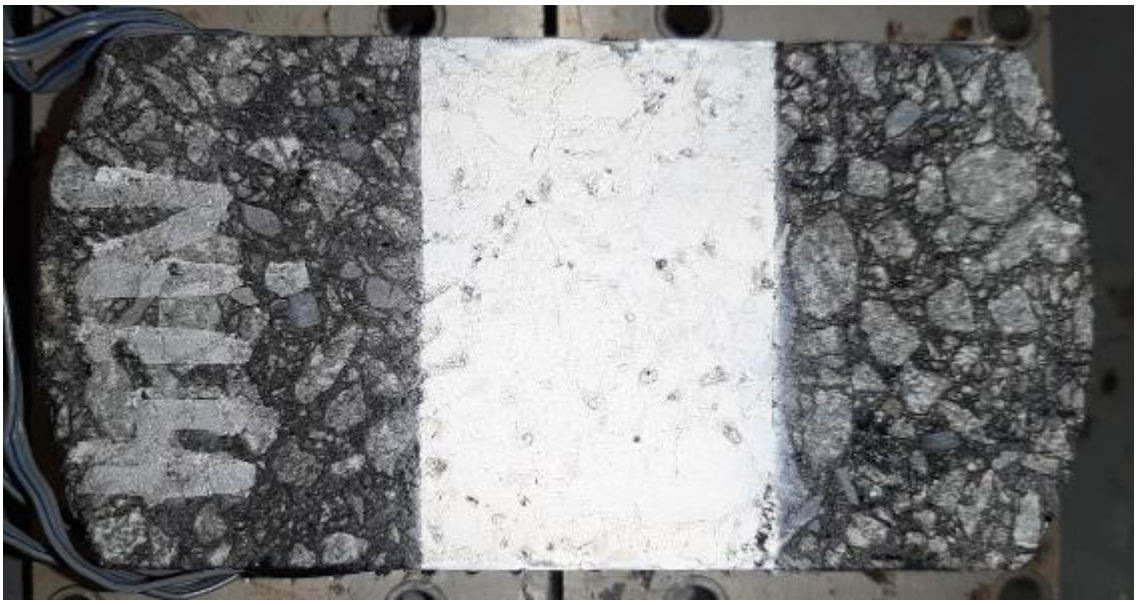

(c) Top Side

Figure I.13: Sample N14 Pictures

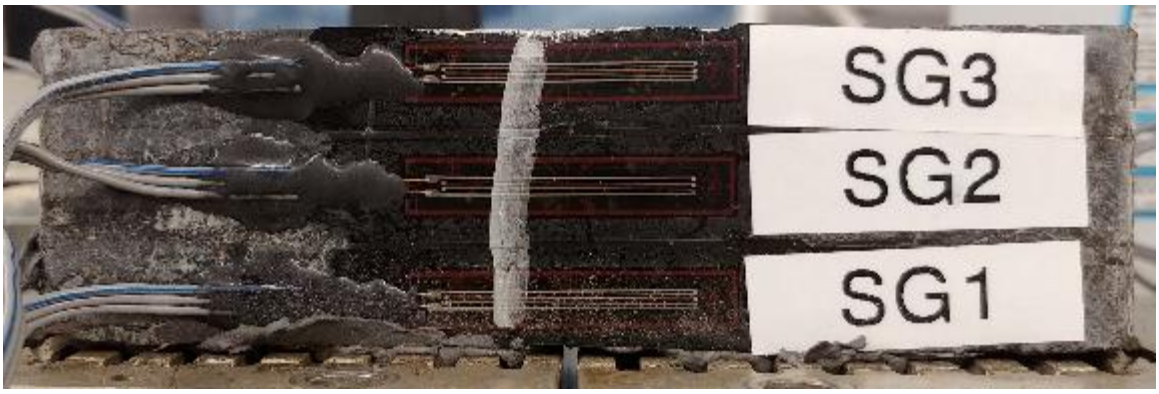

(a) Front Side

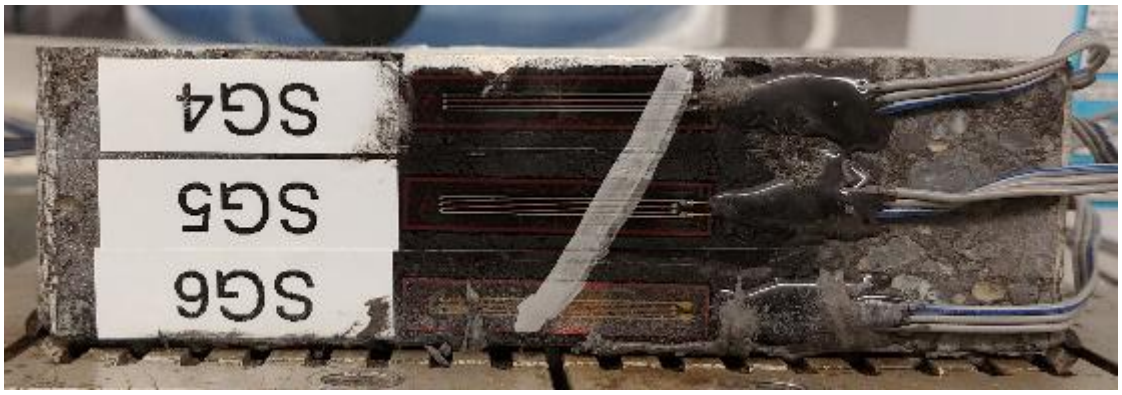

(b) Back Side

(c) Top Side

Figure I.14: Sample N17 Pictures

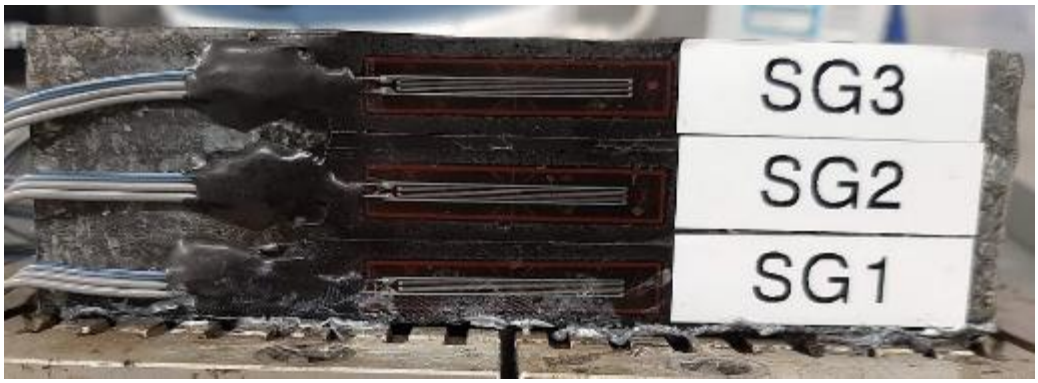

(a) Front Side

(b) Back Side

(c) Top Side

Figure I.15: Sample N18 Pictures

APPENDIX – J: STRAIN GAGE READINGS AT FAILURE

Sample ID	Strain (μE)		
	Bottom Gage	Middle Gage	Top Gage
S3	4722	4539	3482
S7	5921	2361	NA
N8	4110	3121	2257
S10	4911	3823	2769
S11	4412	3009	468
N9	4284	1283	1105
S14	4214	3209	698
N17	5194	3083	NA
N18	NA	NA	NA
S2	5001	2905	1492
N10	1936	1876	714
N12	4015	2121	NA

NA: Failure point cannot be determined from gage response due to erratic readings.